AN ANALYTICAL MODEL FOR THE SEISMIC ANALYSIS OF REINFORCED CONCRETE FRAME STRUCTURES

by

C D Mercer

A thesis submitted in fulfilment of the requirements for the degree of Doctor of Philosophy

Department of Civil Engineering
University of Cape Town
South Africa

November 1987

To

Allison and my parents

ABSTRACT

The thesis is concerned with developing an analytical model to describe the cyclic behaviour of reinforced concrete members. The mechanisms which are important in the behaviour of members dominated by flexural deformations are identified. They include bar-slippage due to deterioration of the bond between the steel and concrete, the crack opening and closing criterion, and the cyclic response of steel and concrete. All these mechanisms are incorporated in an analytical model based on a layered beam approach. The model is developed for a member in double curvature bending and consists of two inelastic zones on either side of a central elastic zone. The bar-slippage which occurs in the beam-column joint is included at the ends of the beam model. A linear bending moment distribution is assumed along the beam. The moment-curvature relationship is calculated in the inelastic zones; the curvature is then integrated along the inelastic zone to determine the displacements. Damage measures with an objective of predicting the onset of failure are also proposed. The implementation of the model into a frame analysis computer program is discussed. Special attention is devoted to the solution strategies and numerical algorithms employed in the computer program. The model is shown to perform satisfactorily when compared to experimental results. A simplified analytical model which approximates the concrete with only two layers is also presented. The simplified model is shown to predict the response as competently as a model with far more concrete layers; however, the computational time for the simplified model is significantly less.

DECLARATION

I, Colin Douglas Mercer, declare that this thesis is essentially my own work and has not been submitted for a degree at another university.

C D Mercer

November 1987

ACKNOWLEDGEMENTS

I wish to express my appreciation to the following :

Professor J B Martin, my supervisor, for his guidance and encouragement during my postgraduate studies.

The Atomic Energy Commission and the Foundation for Research and Development for their financial support.

Luis Resende, Dave Hawla, Gino Duffett, Howard Pearce and other colleagues for the many helpful comments and discussions.

Jack Vos and Helena Voyé for assistance with the database and solvers used in the program development.

Shirley Breed for typing the manuscript.

and finally,
my wife Allison, parents, family and friends for all the support and encouragement.

TABLE OF CONTENTS

NOMENCLATURE

Special Symbols

$\dot{\ }$	differentiation with respect to time
d	derivative
∂	partial derivative
Δ	increment in
Σ	summation
$\mathcal{A}$	finite element assemblage operator
$\sim$	vector
[ ]	matrix
$[\ ]^T$	matrix transpose
$[\ ]^{-1}$	matrix inverse

Lower case

a_1, a_2	constants for steel constitutive model, equation (2.4)
a_i	constants for concrete damage model
b_i	constants for bond stress-slip constitutive model
b^*	width of beam
d	damage variable for bond
$\underset{\sim}{d}$	vector of nodal displacements
d^*	depth of beam
d^j	height of j^{th} concrete layer above base of beam
d^B	height of bottom steel layer above base of beam
d^T	height of top steel layer above base of beam
f^j	force in j^{th} concrete layer
h	distance betwen top and bottom steel layers
m	number of integration intervals for left inelastic zone

n	number of integration intervals for right inelastic zone
p	constant involving circumference and area of bar
q	bond stress
q_F	frictional bond stress
q^B	total axial force in bottom half of beam
q^T	total axial force in top half of beam
$\underset{\sim}{r}^e$	local element internal force vector for bar-slippage model
t	time
$\underset{\sim}{u}$	global displacement vector
$\bar{\underset{\sim}{u}}$	vector of independent variables
v	vertical displacement
x	coordinate along beam
x_a	length of left inelastic zone
x_b	length of right inelastic zone

Upper case

A	area of a steel bar
A_o	area of a bar in bar-slippage model
A_d	damaged concrete area
A_s^T	area of top steel layer
A_s^B	area of bottom steel layer
A_c^j	area of j^{th} concrete layer
B_i	derivatives of shape functions
E	elastic stiffness, Young's modulus
E_t	elastic stiffness for concrete in tension
E_c	elastic stiffness for concrete in compression
E_q	elastic stiffness for bond stress-slip relation
$[E]$	matrix defined in equation (3.35)
F_A^{int}	internal axial force at end A of beam

F_B^{int} internal axial force at end B of beam

F^{int} internal horizontal force at a section

$\underset{\sim}{F}$ global load vector for bar-slippage model

F^{int} internal local force vector, defined in equation (3.82)

F^{ext} external local force vector defined in equation (3.82)

F^* initial axial force at a section

F_s^T force in top steel layer

F_s^B force in bottom steel layer

[G] matrix containing integration constants

$[G^*]$ matrix defined in equation (3.34)

[H] unit matrix defined in equation (3.32)

$[H^*]$ matrix defined in equation (3.34)

[J] Jacobian matrix

I_a second moment of area for section on left of contraflexure point

I_b second moment of area for section on right of contraflexure point

$[k_e]$ element stiffness matrix

$[K_T]$ global tangent stiffness matrix

L total length of beam

L_r anchorage length of bar

M bending moment

M^{int} internal moment at a section

M^* prescribed bending moment at a section

N_A axial member end force at A

N_B axial member end force at B

N_e number of elements in bar-slippage FE model

N_c number of concrete layers

N_p number of nodes per element for bar-slippage FE model

N_i shape functions for node i

P_A normal member end force at A

P_B normal member end force at B

P axial load

$Q(\omega)$ function describing constitutive relation for bond-slip

R curvature parameter for steel constitutive model

R_o constant in steel constitutive model

$\underset{\sim}{R}^{ext}$ global load vector

$\underset{\sim}{R}^{int}$ global internal force vector

$\underset{\sim e}{R}^{int}$ element internal force vector

$\underset{\sim}{R}(\underset{\sim}{d})$ vector of internal forces for bar-slippage model

$S(\epsilon)$ function describing constitutive relation for steel

Greek

α crack width

β crack closure constant

ϵ uniaxial strain

ϵ^* normalized strain for steel constitutive model

ϵ^B strain at bottom steel layer

ϵ^T strain at top steel layer

ϵ^j strain at j^{th} concrete layer

ϵ_m concrete strain corresponding to maximum stress

ϵ_p plastic strain

ϵ_r unloading strain value for steel model

ξ normalized strain difference in steel model

Ω function involving terms for curvatures

λ concrete damage variable

λ_t concrete damage variable in tension

λ_c concrete damage variable in compression

Λ_a anchorage damage measure

Λ_D overall damage measure

Λ_c concrete damage measure

σ uniaxial stress

σ^* normalized stress for steel constitutive relation

σ_r unloading stress value for steel model

σ_{eff} effective stress

ϕ curvature

ϕ^* prescribed curvature

Π function describing integrals for Simpson's Rule

ρ'' percentage volume of hoop steel

$\underset{\sim}{\Psi}$ vector of residuals or out of balance forces

Ψ_o circumference of steel bar

θ rotation

θ^s fixed end rotation

θ' rotation at ends of elastic zone

ω bar slip

ω^* specified bar slip used in calculation of normalized energy

$\bar{\omega}$ prescribed slip

Script

ℓ length of anchored bar

ℓ_e length of elastic zone

$\mathcal{D}$ tangent operator

$\mathcal{E}$ dissipated energy

$\mathcal{E}_o$ normalized dissipated energy

Subscript

a limit of elastic zone at left hand side

b limit of elastic zone at right hand side

A	left hand end of beam model
B	right hand end of beam model
i,j	integration stations for inelastic zones
max	maximum value

Superscript

B	bottom steel layer
T	top steel layer
f	displacement due to flexure
max	maximum value
η	power used in concrete damage model

CHAPTER 1

INTRODUCTION

It is not always feasible to design a typical reinforced concrete frame structure so that it behaves elastically when subjected to a large seismic loading. During the past two decades inelastic design methods have increasingly been practised, see [2] for example. Presently, earthquake design philosophy allows for the development of inelastic regions within the structure in order to control the dissipation of energy and prevent collapse of the structure. In particular, the 'strong column-weak girder' approach allows these inelastic regions to occur in the girders, usually at their ends and not in the columns. The risk of total collapse by a sidesway mechanism is then reduced. Another advantage of this approach is that the dissipation of energy is distributed throughout the structure and not concentrated in one particular part of the structure such as the lower storey.

Predicting the nonlinear response of such structures therefore becomes of primary concern to the design engineer. With the significant advances made in computer technology in recent years, the trend has been towards increasingly more complex analytical modelling techniques such as finite element methods, see for example [1]. Whether such sophistication is always justified remains a point of debate. Biggs [6] and Fajfar [8] address this issue and query the use of the more advanced analytical models in terms of the uncertainties involved. For the design engineer, analytical models are not only required to predict the response of the structure, but also to estimate the amount of damage that has occurred, or more specifically, to

estimate how close the component or structure is to failure. In addition, input to the analytical model needs to be as straightforward as possible. One of the drawbacks of existing simple analytical models lies with the empirical formulae used to determine the cyclic response of a component on a global level. In general, little of the physical processes causing damage and inelastic behaviour are explicitly included in these empirical formulae. Consequently, their validity in terms of response and damage prediction is questionable when applied in conditions which differ from the experimental tests.

It is essentially this issue that the thesis addresses. The main objective is the development of an analytical model where the relevant mechanics are included in the model as an integral part of the damage process. The model is primarily developed for the cyclic behaviour of reinforced concrete members dominated by flexure. Damage measures designed to predict flexural failure in a beam are proposed. Further aspects considered in the development of the model include the formulation of robust solution strategies and numerical algorithms. These are essential for computational efficiency if such an analytical model is to be of practical use. The purpose of the thesis is to illustrate the feasibility of such an analytical model. For this reason only simple structural components are considered in verifying the model. Further development is envisaged before more complex components such as structural frames are considered.

Chapter 2 of the thesis discusses the mechanisms of damage which dominate the cyclic response of reinforced concrete structures. Also included in this chapter are the constitutive models used for concrete, steel and the bond stress-slip relationship in the anchorage of the reinforcing bars. Only the uniaxial behaviour of these materials is considered.

The formulation of the proposed analytical beam model is presented in Chapter 3. The numerical algorithms used to determine the cyclic moment-curvature response and the bar stress-slippage response for an anchored bar are also discussed. The aspects concerned with the computational implementation of the beam model and the solution strategies which are important for efficient nonlinear analysis, are covered in Chapter 4.

The beam model is evaluated in Chapter 5. First, a parametric study is presented in which the consistency of the model is confirmed. This is followed by a comparison of the model with experimental results. A simplified beam model is presented in Chapter 6, where the concrete is approximated by a top and a bottom layer only. The conclusions and recommendations for further research are presented in Chapter 7.

CHAPTER 2

MECHANISMS OF DAMAGE IN REINFORCED CONCRETE AND RELATED MATERIAL CONSTITUTIVE MODELS

During the past two decades considerable research has been conducted to develop a better understanding of the complex mechanisms and their interaction in reinforced concrete structures subjected to seismic loads, see for example [19 - 38]. Experimental tests have covered all possible aspects of concern - from seismic tests on full scale structures to studies of the anchorage characteristics of reinforcing bars. However, the understanding of the relevant mechanisms and their interaction is by no means complete.

In this chapter, a discussion on the mechanisms and factors which dominate the cyclic response of members in reinforced concrete moment resisting frames is presented. The cyclic response of steel, concrete and the bond stress-slip characteristics for the anchorage of a reinforcing bar are included in this chapter, along with the corresponding constitutive material models.

2.1 Damage and Failure of Reinforced Concrete Structures

Some of the earliest tests on the cyclic response of reinforced concrete components were those conducted by Burns and Seiss [24]. In these tests simply supported beams loaded at mid-span were investigated. The results highlighted the importance of compression steel and stirrups in increasing

the rotational ductility of members. Researchers have since concentrated on specific components of a typical moment resisting frame structure. The bending moment distribution in such a structure resulting from lateral loading allows three components or assemblages to be identified; the cantilever beam, an exterior beam-column connection and an interior beam-column connection. These three components are shown in Figures 2.1 - 2.3 respectively. The extent to which the cantilever beam in Figure 2.1 can be considered as a separate component when compared to the exterior beam-column connection in Figure 2.2, depends on the relative flexural capacities of the beam and the column.

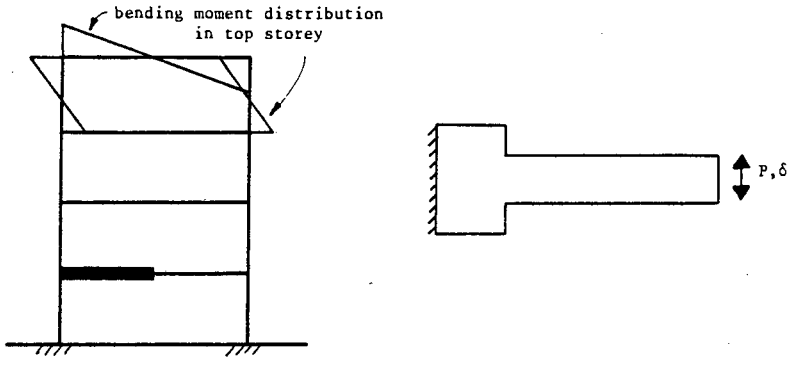

Figure 2.1 : Cantilever component

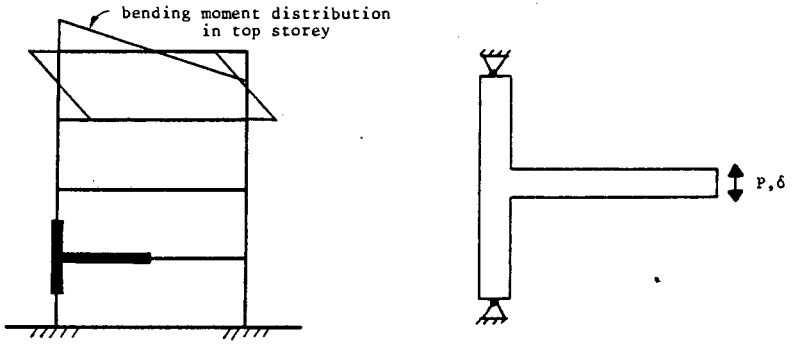

Figure 2.2 : Exterior beam-column assemblage

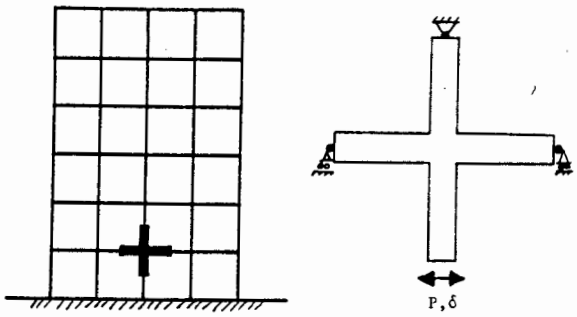

Figure 2.3 : Interior beam-column assemblage

Bertero and Popov [20] classify the behaviour of reinforced concrete regions according to the controlling stress states; (i) regions controlled by bending or flexure, (ii) regions controlled by high shear and (iii) regions controlled by high axial and shear forces. In this section, the emphasis is on the first two classes of regions.

Experimental cyclic tests on cantilever beams [25,32,33] give some insight into the more fundamental aspects of the mechanisms controlling the behaviour of reinforced concrete components. In the immediate discussion it is assumed that slippage of the reinforcing bars does not occur; this important aspect will be discussed later in this section.

A typical reinforced concrete cantilever beam with a cyclic loading sequence is shown in Figure 2.4(a). The load-displacement response for one load cycle is given in Figure 2.4(b). As the load is initially applied, the response is essentially elastic as indicated by the curve AB. At point B of the response, cracks in the concrete propagate from the top of the beam, predominantly near the fixed end. Figure 2.4(d) illustrates the beam at this stage of the loading. As the load is increased, further cracks develop

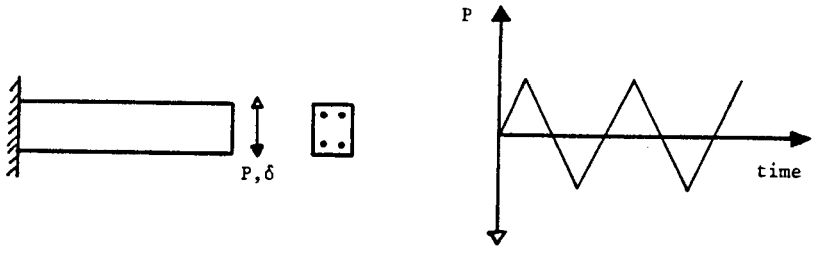

Figure 2.4(a) : Cantilever beam and loading sequence

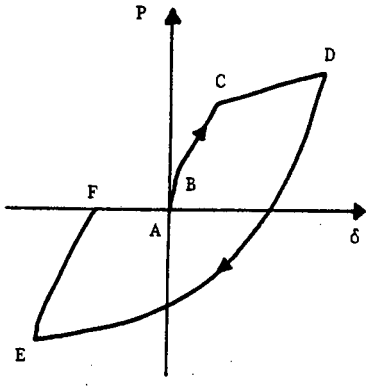

Figure 2.4(b) : Load-displacement response for 1st cycle

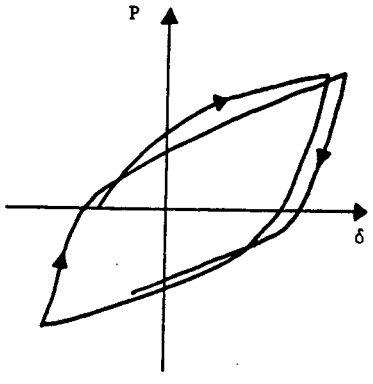

Figure 2.4(c) : Load-displacement response for further cycles

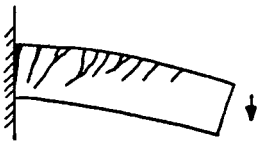

Figure 2.4(d)

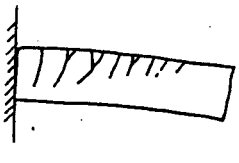

Figure 2.4(e)

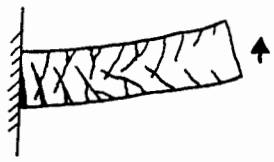

Figure 2.4(f)

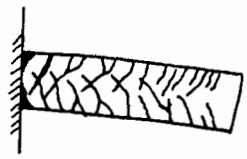

Figure 2.4(g)

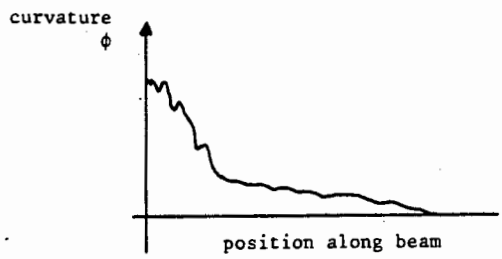

Figure 2.4(h) : Curvature distribution

in the concrete along the beam. The amount of cracking and the inclination of the cracks depends on the shear stress state and the amount of transverse reinforcement. The cracking continues until the top steel reinforcement yields - point C in Figure 2.4(b). This yielding causes a significant change in the load deflection response, mainly as a result of large curvatures near the fixed end. The resulting load-deflection response is indicated by curve CD in Figure 2.4(b). If the loading is large enough, spalling of the concrete can occur in the bottom of the beam at the fixed end. At point D in Figure 2.4(b), the load is reversed. The beam's response is initially elastic and fairly stiff; however, as the cracks close

the response becomes more nonlinear. Figure 2.4(e) illustrates the beam when the load is zero, the permanent deformation which has occurred is clearly evident. As the load is increased in the opposite direction, the existing cracks close completely and new cracks develop as the concrete in the lower part of the beam reaches its tensile strength. These cracks propagate from the bottom face of the beam and, as in the first half of the cycle, are more dominant towards the fixed end. The load-deflection response, curve DE in Figure 2.4(b), is the result of closure of old cracks, the development of new cracks, as well as the Bauschinger effect of the reinforcing steel. This aspect is discussed in more detail in section 2.2. The beam at this stage of loading is illustrated in Figure 2.4(f). Reducing the load to zero completes the first load cycle. The load-deflection response is indicated by curve EF in Figure 2.4(b). Provided the integrity of the beam is maintained, further load cycles produce load-deflection response curves similar to the one shown in Figure 2.4(c). As the cyclic loading sequence is continued, unconfined concrete in both the top and bottom faces of the beam may start to spall at the fixed end. With large enough loads, the confined concrete begins to lose its integrity and can also spall. The spalling results in the load-deflection curve being dominated by the response of the steel at the fixed end. Figure 2.4(g) illustrates the beam after a number of load cycles. The curvature distribution along the beam when the loading is at a maximum, is shown in Figure 2.4(h). A region of high curvature exists near the fixed end of the beam where the inelastic deformation is concentrated. In the remainder of the beam where the deformations are essentially elastic, the curvature distribution is approximately linear.

In the discussions thus far, only flexural deformations have been considered. Slippage of the longitudinal reinforcing bars at the fixed end

can contribute significantly to the deformations of the beam. Briefly, slippage is the result of a deterioration in the bonding mechanisms of the reinforcing bars due to cyclic loading, in addition to the yielding of reinforcing bars. A detailed account of the mechanisms involved in this process is given in section 2.4.

Slippage increases the crack widths at the fixed end, introducing an additional rotational component to the beam. These are generally referred to as fixed end rotations, and result in an increase in the maximum tip displacement of the cantilever. Results given by Ma *et al* [33] illustrate the load deflection response for a typical cantilever beam. These results

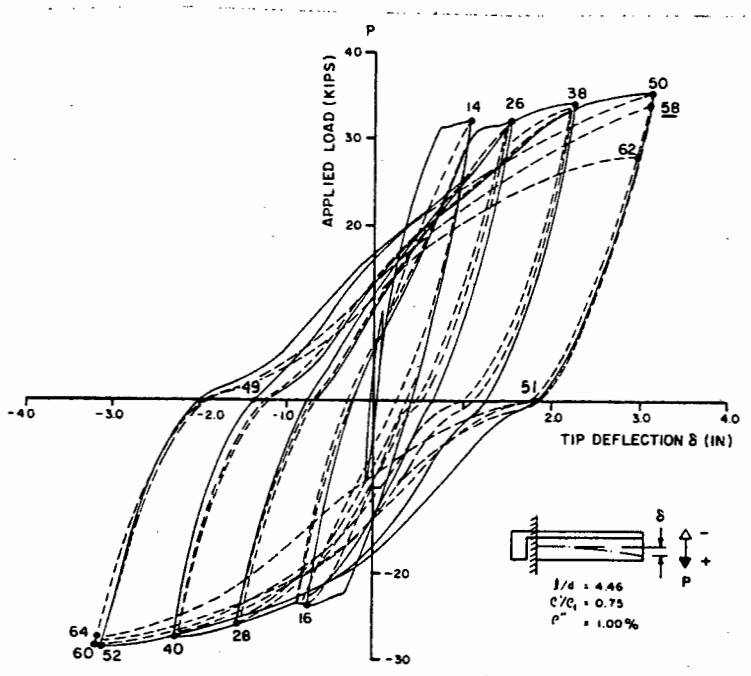

Figure 2.5(a) : Typical load-displacement response, from [33]

are given in Figure 2.5(a) with the corresponding moment - fixed end rotation response shown in Figure 2.5(b). In this experiment, the fixed end rotation accounted for approximately 50% of the tip displacement.

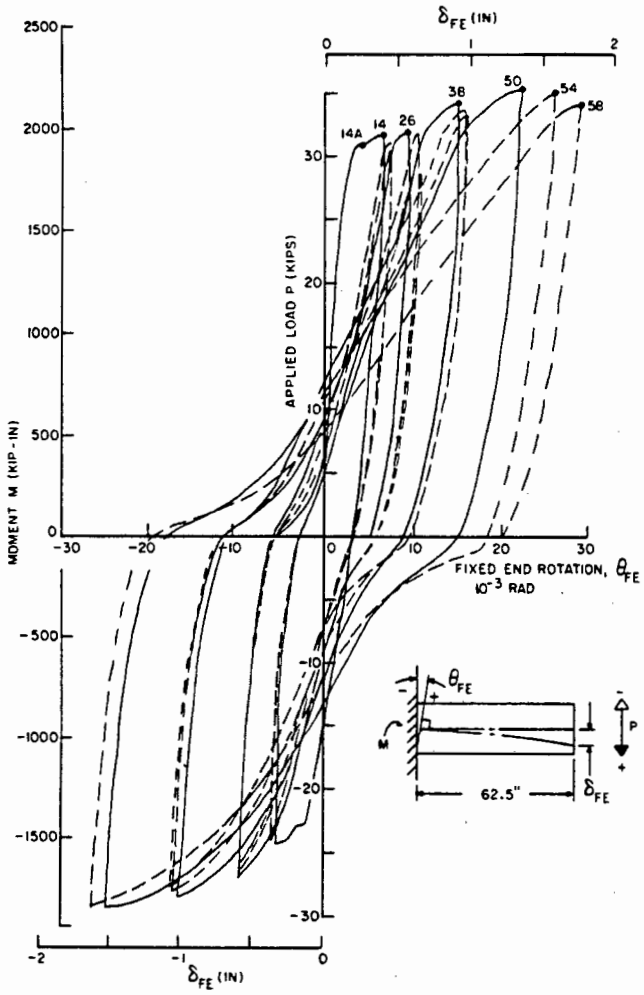

Figure 2.5(b) : Moment-fixed end rotation response, from [33]

The discussion by Filippou *et al* [18] on the mechanical behaviour of a cracked reinforced concrete section helps to clarify the effect that bar slippage has on the response. Figure 2.6(a) illustrates the development of a crack at a section as the result of deterioration in the bonding mechanisms of the bottom reinforcing bars. For the bending moment shown, the forces that are in equilibrium at the section are the tensile forces in the bottom reinforcing bars and the compressive forces in the concrete and reinforcing bars at the top of the beam. When the bending moment is reversed at the section, the top reinforcing bars are subjected to increasing tensile forces, resulting in deterioration of the bonding mechanism. This results in development of the crack through the complete

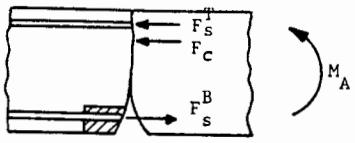

Figure 2.6(a)

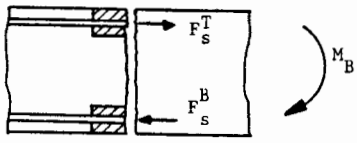

Figure 2.6(b)

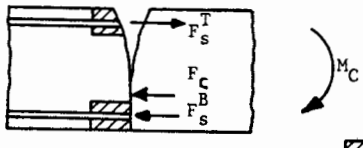

Figure 2.6(c)

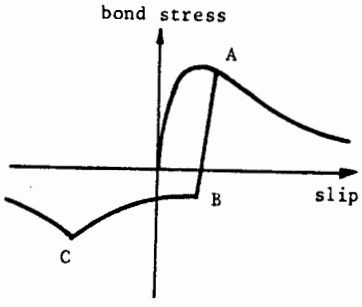

Figure 2.6(d)

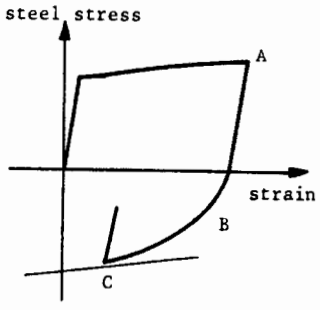

Figure 2.6(e)

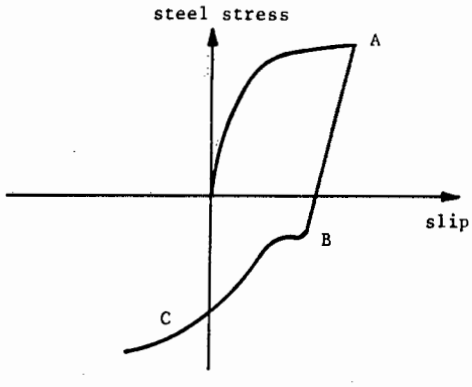

Figure 2.6(f)

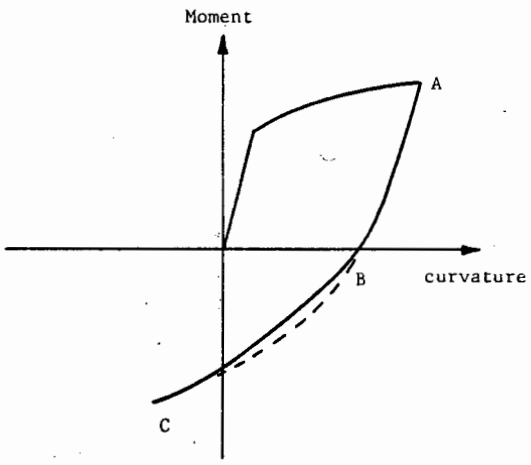

Figure 2.6(g)

Figure 2.6 : Crack closure at a reinforced concrete section, 2.6(a) - (e) from Filippou *et al* [18]

section as illustrated in Figure 2.6(b). At the same time, the compressive stresses in the bottom reinforcing bars increase. Typically, the top reinforcement area is about twice the bottom reinforcement area and to maintain equilibrium at the section, the stresses in the bottom bars increase more rapidly than the stresses in the top bars. As the compressive stresses in the bottom reinforcing bars increase, slippage occurs when the bond stress reaches the frictional resistance of the bonding mechanism. This onset of slippage is indicated by point B in Figures 2.6(d) and 2.6(e). The crack at the bottom of the beam then closes and compressive stresses build up in the concrete at the bottom of the section. This contribution to the total compressive force becomes significant, whilst the proportion of steel contribution reduces. The section at this stage is illustrated in Figure 2.6(c), and indicated by point C in Figures 2.6(d) - 2.6(g). Filippou *et al* [18] support this explanation by noting that as a consequence

of bar slippage during crack closure, tensile plastic strains in the steel from previous load cycles are never fully recovered and 'tend to centre about an ever increasing plastic tensile strain' - a phenomenon which has been observed in experimental tests [38]. Crack closure results in a slight 'pinching' of the moment-curvature response as illustrated in Figure 2.6(g).

Once significant bond deterioration has occurred at a cracked section, relative slippage takes place between the reinforcing bar and the concrete. The stress transfer between the concrete and the steel occurs away from the cracked section, where bonding is adequate. The compressive stresses are transmitted across the cracked section by 'arching action' as illustrated in Figure 2.7.

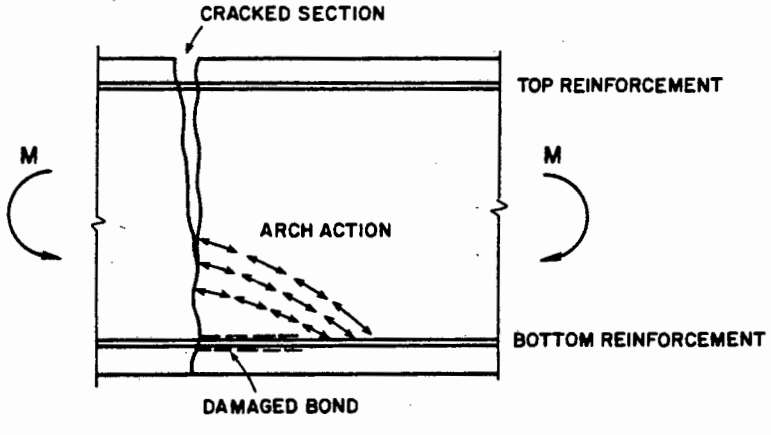

Figure 2.7 : Compressive stresses in concrete during crack closure, from [18]

An important factor which effects the behaviour of a cracked section is shear deformation. Shear forces are transmitted across a cracked section by a combination of dowel action (shear stresses in the steel bars) and aggregate interlock (shear transfer in the cracked concrete). When the shear forces are large enough, shear slippage can occur at a cracked

section. Not only does this contribute to the deflections of the beam, but it causes the integrity of the concrete to deteriorate rapidly. Such deformation causes abrasion as well as spalling of the unconfined concrete. As a result, high shear forces produce significant pinching of the load displacement response as illustrated in Figure 2.8. Dowel action can cause further deterioration of the concrete near the cracked section, at the same time degrading the bonding mechanism.

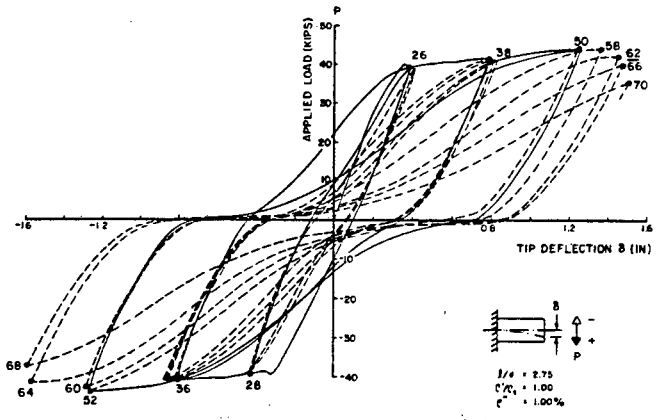

Figure 2.8 : Load-displacement response showing pinching due to shear, from [33]

Failure of beams dominated by flexure, generally occurs with the bottom reinforcing bars buckling or fracturing. This is caused by a combination of factors such as spalling of the unconfined concrete, localized cracking and crushing of the confined concrete. The loss of concrete cover as well as yielding of the steel and dowel action due to shear slippage, tend to reduce the buckling load of the bars.

Experimental results have shown that reduced stirrup spacing generally produces greater confinement of the concrete and delays the buckling of the reinforcement [26,28,32,33]. Apart from significant cracking near the fixed end, generally referred to as the 'hinging zone', small cracks develop along

the remainder of the beam. These cracks usually remain stable, and the response in this part of the beam is essentially elastic. Most of the inelastic deformations occur in the hinging zone.

Tests of external beam-column assemblages [26,27,28,31] have highlighted the importance of maintaining the integrity of the beam-column joint. The mechanisms of damage described for the cantilever are further complicated by deformations in the columns and the joint. In beam-column connections, the flexural strength ratio M_R , defined as the ratio of the sum of the flexural capacities of the columns to that of the beam, controls the position of the hinging zone. When the flexural strength ratio is less than 1.0 , the hinging zone tends to form in the columns or joint. This is not desired in the weak beam-strong column design of frames, and typically this value is greater than 1.0 . When the flexural strength ratio is of the order 1.5-2.0, the hinging zone forms in the beam. For flexural strength ratios slightly greater than 1.0 , the hinging zone can form in the joint. When this occurs the anchorage characteristics of the reinforcing bars are adversely affected. As the concrete confined in the joint cracks, slippage of both the beam and column reinforcement increases. High shear stresses in the joint have a similar effect on the performance of the joint. In tests where the hinging zone was located in the beam and with adequate transverse reinforcement in the column and joint, little inelastic deformation was evident in the columns [27].

The response of interior beam-column assemblages illustrates two further aspects which contribute to the understanding of mechanics of damage in reinforced concrete structures. Lateral loading of such an assemblage causes cracked sections to develop in the beams on either side of the

column. The longitudinal reinforcing bars of the beams are anchored in the column and are usually continuous through the column. Under lateral loading conditions the bars are in compression on one side of the column and in tension on the other side. With a severe cyclic loading sequence the bonding mechanism is soon destroyed and the bars are able to move freely within the joint. Figure 2.9 illustrates such an event. Extensive experimental tests have been performed at Berkeley, California, on interior beam-column subassemblages, see for example [20], and in particular on the bond characteristics of reinforcing bars under such loading conditions, see for example [35,36,56,58].

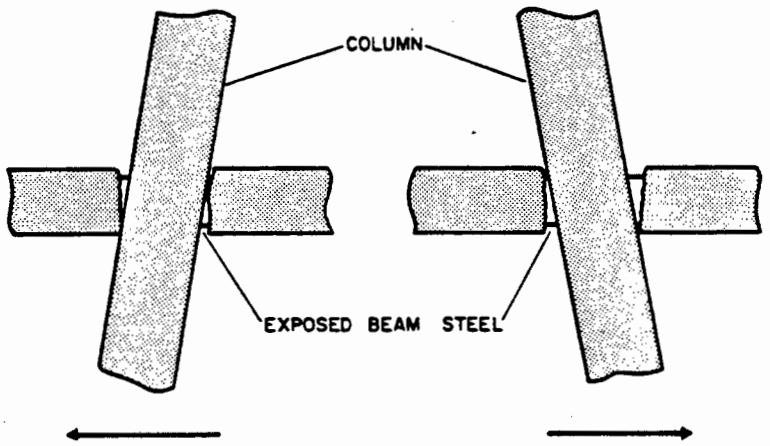

Figure 2.9 : Crack development during cyclic response of beam-column assemblage, from [61]

An aspect which becomes important in structures as the deformations increase is the additional moments resulting from axial forces in the column and large lateral displacements, generally referred to as the P - δ effect. The significance of this effect has been highlighted by Bertero and Popov [20], where they compare the load-deflection (H - δ) results for a subassemblage and the equivalent shear force (H_{eq}) which includes the P - δ effect. The equivalent shear force is obtained from the relationship $H_{eq} = H + P\delta/h_{col}$. This comparison is shown in Figure 2.10.

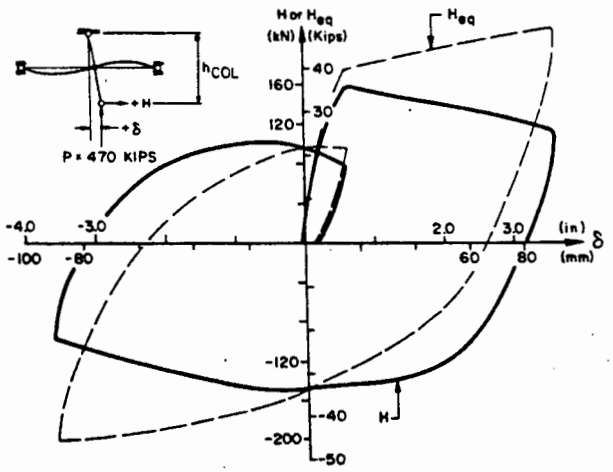

Figure 2.10 : Load-displacement response for beam-column assemblage, from [20]

2.2 Steel Constitutive Model

The cyclic stress-strain response of a typical reinforcing bar at a beam-column joint is illustrated in Figure 2.11. Two important factors evident in this response are, (i) the Bauschinger effect, and (ii) the hysteretic response which is centred around an ever increasing plastic strain in tension. The latter phenomenon is due to the combined effect of crack closure and bar slippage. This aspect has been dicussed in section 2.1. The Bauschinger effect is the gradual yielding that occurs in the steel when loading is reversed. This effect is important since the reinforcing steel tends to dominate the response at cracked sections.

A considerable number of researchers have investigated stress-strain models in an attempt to find one which reproduces the experimental results sufficiently well, and at the same time is computationally efficient. These models range from the simple bilinear elastic-plastic relationship to fairly sophisticated models. Campi *et al* [36], Stanton *et al* [39] and Filippou *et*

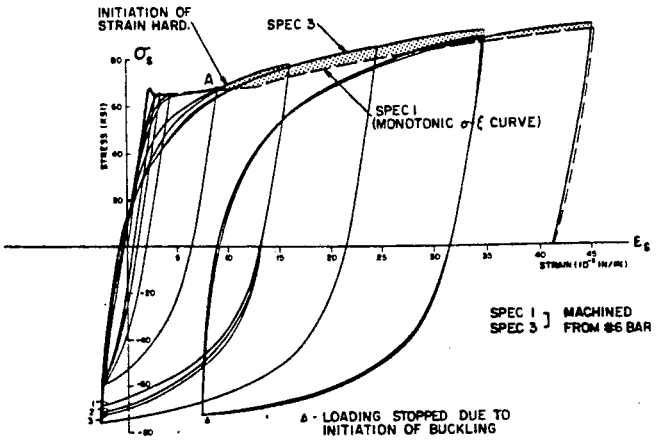

Figure 2.11 : Steel stress-strain response, from [33]

al [18] have shown that the model proposed by Giuffre and Pinto [40] is compatible with the above requirements. This model is used in the present research.

The model was used by Menegotto and Pinto [41] and is sometimes referred to as the Menegotto-Pinto model. It consists of a basic stress-strain curve which is defined in a normalised stress space and mapped onto the actual stress-strain curve. The stress-strain relationship is illustrated in Figure 2.12 and is defined by the following equations :

$$\sigma^* = b\,\epsilon^* + \frac{(1 - b)\,\epsilon^*}{(1 + \epsilon^{*R})^{1/R}} \qquad (2.1)$$

where σ^* is the normalized stress defined as

$$\sigma^* = \frac{\sigma - \sigma_r}{\sigma_o - \sigma_r} \quad , \qquad (2.2)$$

and ϵ^* is the normalized strain defined as

$$\epsilon^* = \frac{\epsilon - \epsilon_r}{\epsilon_o - \epsilon_r} \quad , \tag{2.3}$$

where

σ,ϵ are the actual stress and strain values

σ_o,ϵ_o are the stress and strain values at the point of intersection of the two asymptotes defining the unloading-reloading curve, E_0 and E_1 respectively, e.g. point B in Figure 2.12(a)

σ_r,ϵ_r are the stress and strain values of the point on the asymptote E_1 at which the most recent unloading occurred for the branch under consideration, e.g. point A in Figure 2.12(a) for branch 1

R is a parameter which defines the curvature of the transition from the asymptote E_0 to the asymptote E_1 .

An expression defining R as a function of a strain difference is given in [41]. This expression has the form

$$R(\xi) = R_o \frac{a_1 \xi}{a_2 + \xi} \tag{2.4}$$

where ξ is the normalized strain difference between the point (σ_o,ϵ_o) and the point on the same asymptote at which the largest strain occurred previously, see Figure 2.12(c).

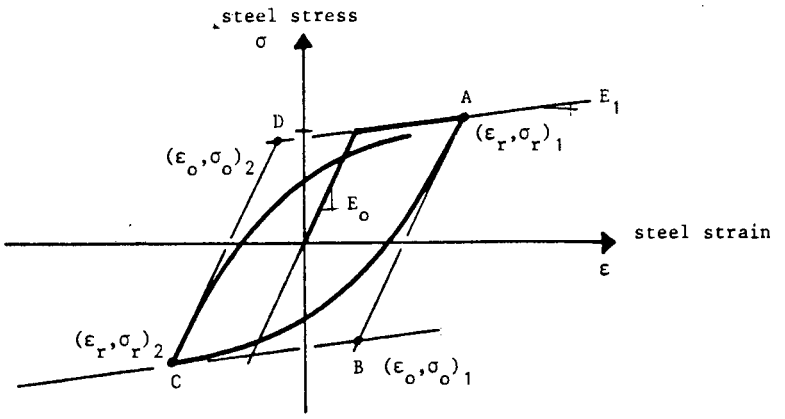

Figure 2.12(a)

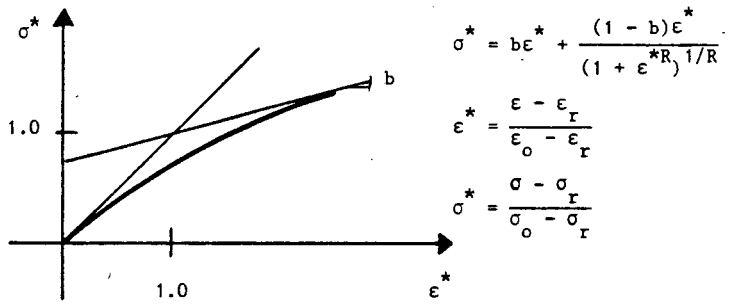

Figure 2.12(b)

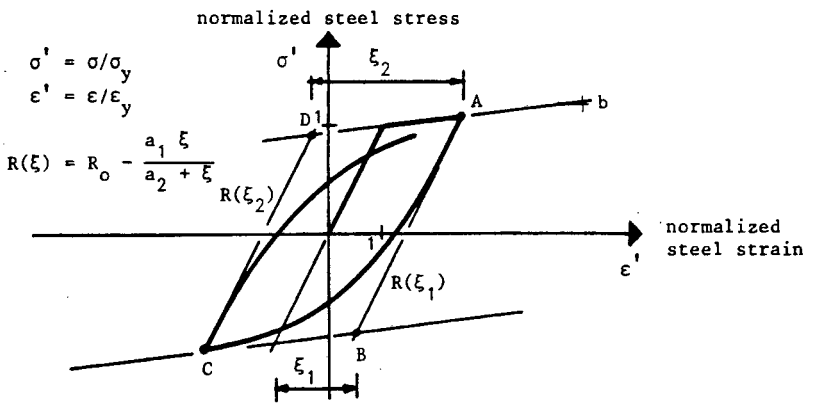

Figure 2.12(c)

Figure 2.12 : Menegotto-Pinto steel model

The stress-strain space is normalized in this definition with respect to the corresponding yield values. R_o, a_1 and a_2 are constants with the following values suggested by Menegotto and Pinto [41] :

$$R_o = 20.0$$

$$a_1 = 18.5$$

$$a_2 = 0.15 \ .$$

The relationship between ϵ^* and σ^* , equation (2.1), is illustrated in Figure 2.12(b).

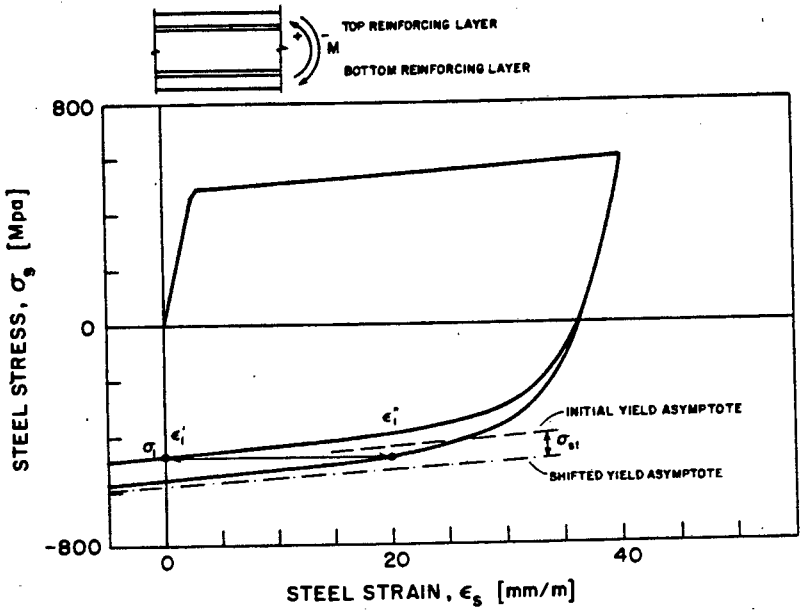

Figure 2.13 : Isotropic hardening effect in steel bars, from [18]

Filippou *et al* [18] and Stanton *et al* [39] have proposed an additional refinement of the model to allow for isotropic hardening. At a particular stress level for a yielding reinforcing bar, σ_1 , the difference in the strains obtained for models excluding and including the isotropic hardening effect is illustrated in Figure 2.13. This difference is significant and can effect the crack closure characteristics as well as the curvature at a cracked section. The simple modification suggested by Filippou [18] has been implemented in the constitutive model for the present studies.

A typical stress-strain relation obtained using this constitutive model is illustrated in Figure 2.14.

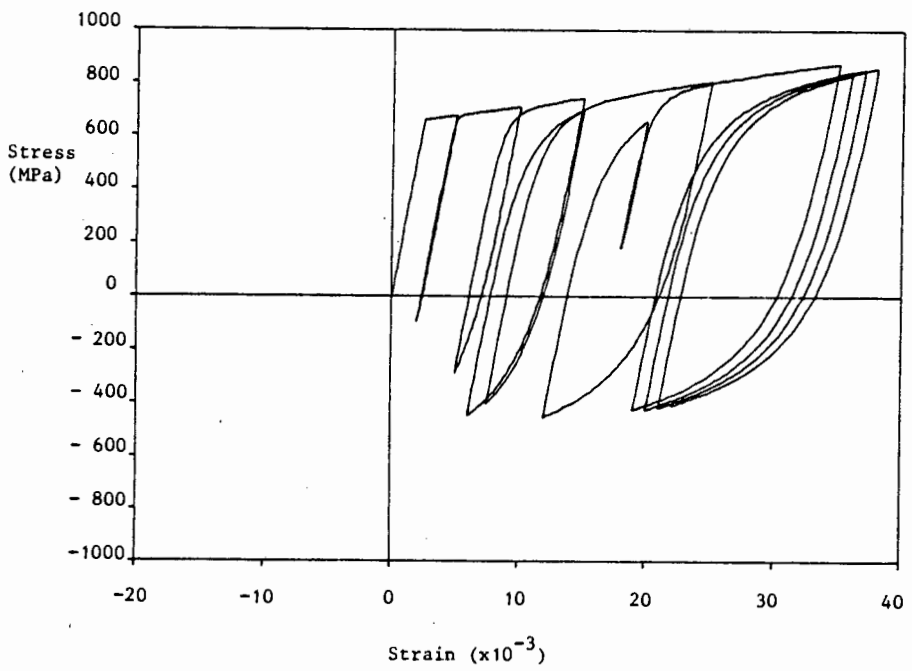

Figure 2.14 : Typical stress-strain response using Menegotto-Pinto model

2.3 Concrete Constitutive Model

The behaviour of concrete is by no means straightforward and has been extensively researched. Recent experimental studies by van Mier [3] highlight the difficulties involved in understanding the fracture nucleation and propagation mechanisms in concrete for various stress loading conditions. Briefly, at the microstructure level, concrete is characterised by a distributed microcrack field. As the loading is increased, the microcracks coalesce to form fracture or crack bands - a phenomenon called localization. The mechanics involved in this process are complex and beyond the scope of this study; they are thoroughly covered by Bazant [43] in his recent state-of-the-art discussion on the subject.

The response of concrete in beams is characterised according to its prevailing stress state - unconfined concrete will behave predominantly as a brittle material, while confined concrete will exhibit both brittle and ductile characteristics.

It is clear from the discussions in section 2.1 that a versatile constitutive model for concrete is essential. The model is required to give a good representation at all levels of strain, including the effects of cyclic loading. This study is only concerned with the uniaxial behaviour of concrete - in reality a multiaxial stress state exists. Sophisticated modelling techniques such as the finite element method are required to capture the multiaxial stress state.

Constitutive models used in similar studies of cyclically loaded reinforced concrete have tended to consist of a series of curves such as the model proposed by Park *et al* [72] and illustrated in Figure 2.15. An alternative

model based on damage mechanics concepts is used in this study. Such a model is attractive due to the simplicity with which it describes the basic damage process.

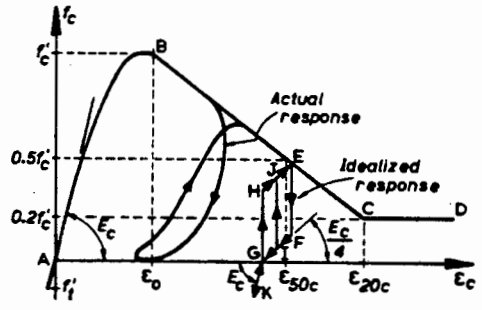

Figure 2.15 : Concrete stress-strain model, from [72]

Damage mechanics describes the behaviour of a degrading material in terms of the evolution of a continuous defect field. This concept has been used in concrete to describe the irreversible mechanical changes in the micro-structure associated with microcracking. Since the original proposal by Kachanov [44] to use a damage variable to describe aspects of creep in metals, a number of effective constitutive models for brittle materials such as concrete and rock have been developed, see for example [45-53].

In the following discussion, a simple one-dimensional damage model is formulated for a specimen loaded in uniaxial tension. For concrete loaded in uniaxial tension, the microcracks propagate in a plane which has the loading direction as its normal.

A scalar damage parameter λ is chosen in such a way that it not only has a simple analytical form, but it is also in agreement with the mechanisms involved in the damage process. Physically, λ represents the microdefect

surface density. Analytically, this can be expressed for a specimen loaded in tension as,

$$\lambda = \frac{A_d}{A_o} \tag{2.5}$$

where A_o is the total cross sectional area of the specimen and A_d is the damaged area.

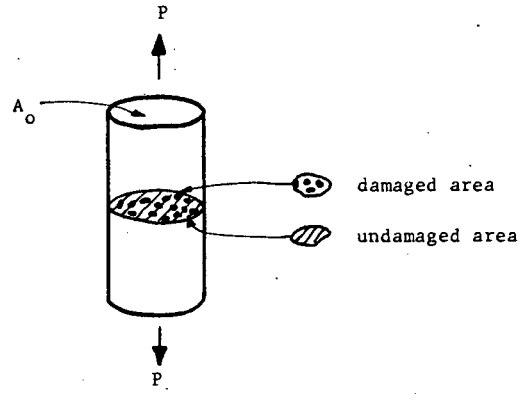

Figure 2.16 : Concrete damage

These quantities are illustrated in Figure 2.16. From this equation it is apparent that λ varies from a value of 0 in the undamaged state, to a value of 1 when the specimen is totally fractured. The load P is now carried by the undamaged area of the specimen, $(A_o - A_d)$. The stress is defined as

$$\sigma = \frac{P}{A_o} \quad , \tag{2.6}$$

and the effective stress as

$$\sigma_{eff} = \frac{P}{(A_o - A_d)} = \frac{P}{A_o(1 - \lambda)} \quad . \tag{2.7}$$

Linear elastic behaviour is assumed to govern the effective stress-strain relation;

$$\sigma_{eff} = E\,\epsilon \tag{2.8}$$

where E is the elastic stiffness for the material and ϵ is the strain.

From equations (2.5)-(2.8) the following stress-strain relation can be obtained,

$$\sigma = E(1 - \lambda)\,\epsilon \quad . \tag{2.9}$$

In terms of the numerical implementation of such a model, it is expedient to express equation (2.9) in an incremental or rate form. For <u>concrete in tension</u> (denoted by the subscript t), the rate form is given as

$$\dot{\sigma} = E_t(1 - \lambda_t)\,\dot{\epsilon} - E_t\,\dot{\lambda}_t\,\epsilon \tag{2.10}$$

where $\dot{\lambda}_t > 0$ for $\lambda_t = \lambda_t^{max}$, $\dot{\epsilon} > 0$

$\dot{\lambda}_t = 0$ otherwise,

and $\dot{\epsilon}$ is the strain rate.

When $\dot{\lambda}_t > 0$, loading or further damage occurs and results in a progressive loss of stiffness. Elastic unloading or reloading occurs when $\dot{\lambda}_t = 0$. The unloading takes place along the secant, with the stiffness given by $E_t(1 - \lambda_t)$. The rate at which damage occurs $\dot{\lambda}_t$, or damage evolution, must be defined in order to complete the constitutive model. The damage

evolution is given as a function of the form

$$\dot{\lambda}_t = \dot{\lambda}_t(\epsilon, \dot{\epsilon}, a_i)_t \quad . \tag{2.11}$$

where $(a_i)_t$ are constants which can be described as material parameters for concrete in tension.

The total amount of damage λ_t is obtained by integrating the rate of damage in time, expressed as

$$\lambda_t = \int_{\text{time}} \dot{\lambda}_t \, dt \quad , \quad 0 \leq \lambda_t \leq 1 \quad . \tag{2.12}$$

A damage model is also used to describe the uniaxial compressive behaviour of concrete. However, the microcracks in this case propagate in the same direction as the direction of loading. For this reason the damage evolution for concrete in compression is different to that in tension. An independent damage parameter λ_c is defined for concrete in compression, with the rate form of equation (2.9) given as

$$\dot{\sigma} = E_c(1 - \lambda_c)\,\dot{\epsilon} - E_c\,\dot{\lambda}_c\,\epsilon \tag{2.13}$$

where $\dot{\lambda}_c > 0$ for $\lambda_c = \lambda_c^{max}$, $\dot{\epsilon} < 0$

$\dot{\lambda}_c = 0$ otherwise.

The damage evolution is given as a function of the form

$$\dot{\lambda}_c = \dot{\lambda}_c(\epsilon, \dot{\epsilon}, a_i)_c \tag{2.14}$$

where $(a_i)_c$ are constants which can be described as material parameters for concrete in compression.

The total amount of damage λ_c is given by the expression

$$\lambda_c = \int \dot{\lambda}_c \, dt \quad , \quad 0 \leq \lambda_c \leq 1 \quad . \tag{2.15}$$

The choice of the function for damage evolution is an important issue in the definition of the model. In the following discussion, λ refers to both λ_t and λ_c. When a linear function is used to describe the integrated form of equations (2.11) or (2.14), the model reduces to the parabolic stress-strain relation illustrated in Figure 2.17(a). The linear function for damage is given by

$$\lambda = a_1 \epsilon \tag{2.16}$$

and illustrated in Figure 2.17(b).

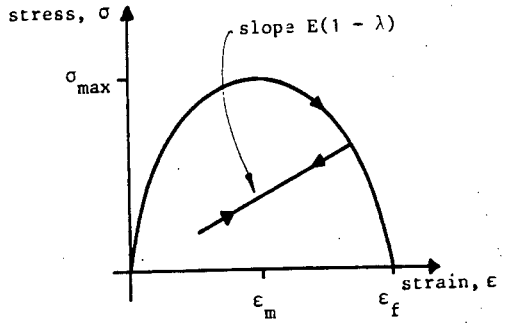

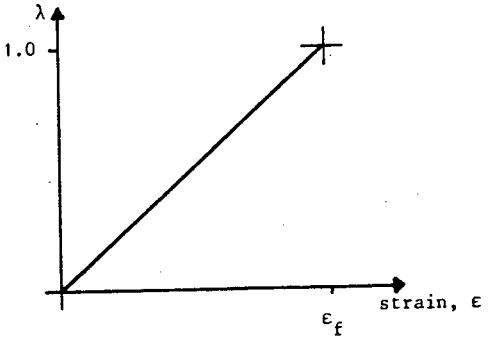

Figure 2.17(a) : Stress-strain relation Figure 2.17(b) : Damage evolution

The constant a_1 can be found by using the maximum stress and corresponding strain, σ_{max} and ϵ_m respectively,. The resulting stress-strain relation reduces to

$$\sigma = E\left[1 - \frac{\epsilon^2}{2\,\epsilon_m}\right] \qquad (2.17)$$

which is identical to Hogenstad's proposed equation for concrete in compression.

Resende [53] has shown that by using a rational function to describe the integrated form of damage evolution, a monotonic stress-strain relationship which corresponds closely with the actual behaviour is obtained. Resende suggests a function of the form

$$\lambda = \frac{a_1\,\epsilon^2}{1 + a_2\,\epsilon + a_1\,\epsilon^2} \quad . \qquad (2.18)$$

The monotonic stress-strain relation reduces to

$$\sigma = E\,\frac{(1 + a_2\,\epsilon)\,\epsilon}{1 + a_2\,\epsilon + a_1\,\epsilon^2} \quad . \qquad (2.19)$$

This is illustrated in Figure 2.18(a), with the damage evolution (equation (2.19)) given in Figure 2.18(b).

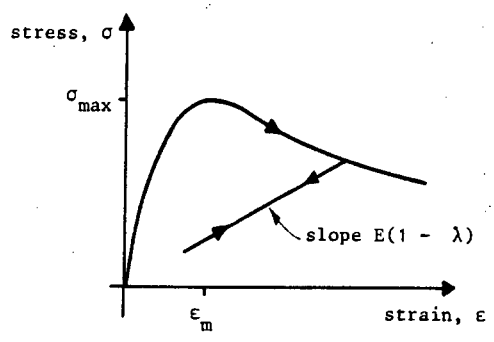

Figure 2.18(a) : Stress-strain relation

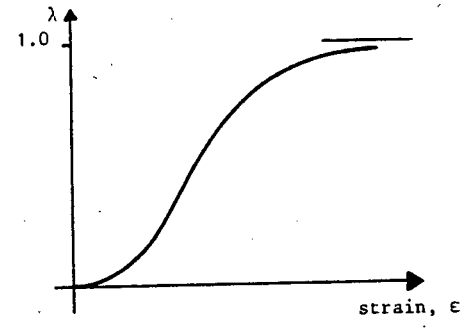

Figure 2.18(b) : Damage evolution

In this study, the initial elastic stiffness E is considered as an unknown. The constants a_1, a_2 and E are obtained by using the following parameters : (i) the maximum stress, σ_{max} , (ii) the corresponding strain, ϵ_m , and (iii) the stress as the strain tends to infinity, σ_∞ . The initial elastic stiffness E is not considered as a material property to calibrate the model for two reasons. Firstly, in practice an initial damage field usually exists in the concrete and it thus becomes difficult to determine a value of E . Secondly, for the applications in the study, reasonable accuracy in the response at larger strains is important.

The difference in the stress-strain response for confined and unconfined concrete is significant. Figure 2.19 illustrates the analytical curves suggested by Kent and Park [19] for different amounts of transverse reinforcement, ρ'' is the ratio of volume of transverse reinforcement to

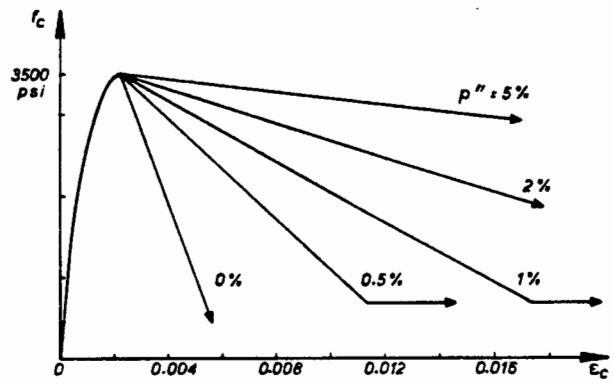

Figure 2.19 : Influence of volume of hoop steel on stress-strain response for concrete, from [19]

volume of confined concrete. The form of damage evolution described in equation (2.16) gives a stress-strain response which is in agreement with the suggested relationship for well confined concrete ($\rho'' > 1\%$). This comparison is illustrated in Figure 2.20. However, the same cannot be said

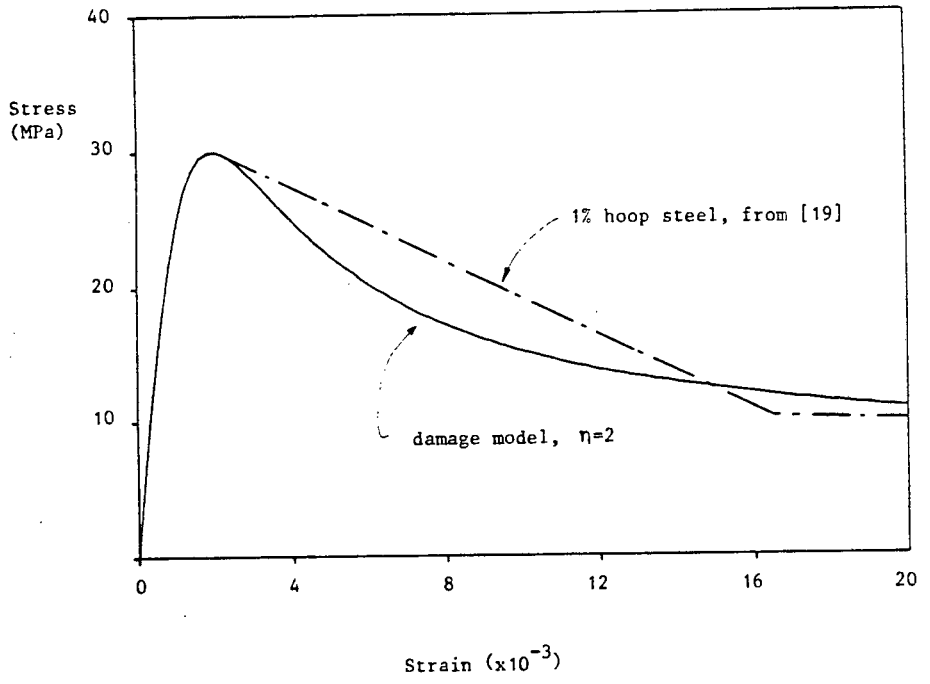

Figure 2.20 : Damage model for confined concrete

for unconfined concrete. A more general form of equation (2.16) is suggested for unconfined concrete,

$$\lambda = \frac{a_1 \epsilon^{\eta}}{1 + a_2 \epsilon^{\eta-1} + a_1 \epsilon^{\eta}} \quad . \tag{2.20}$$

For $\eta = 2$ this equation reduces to equation (2.18).

Figure 2.21(a) illustrates the damage evolution for different values of η , and Figure 2.21(b) the corresponding stress-strain relations. When $\eta = 4$, the stress-strain relation correlates with the suggested curve for unconfined concrete. This comparison is made in Figure 2.22.

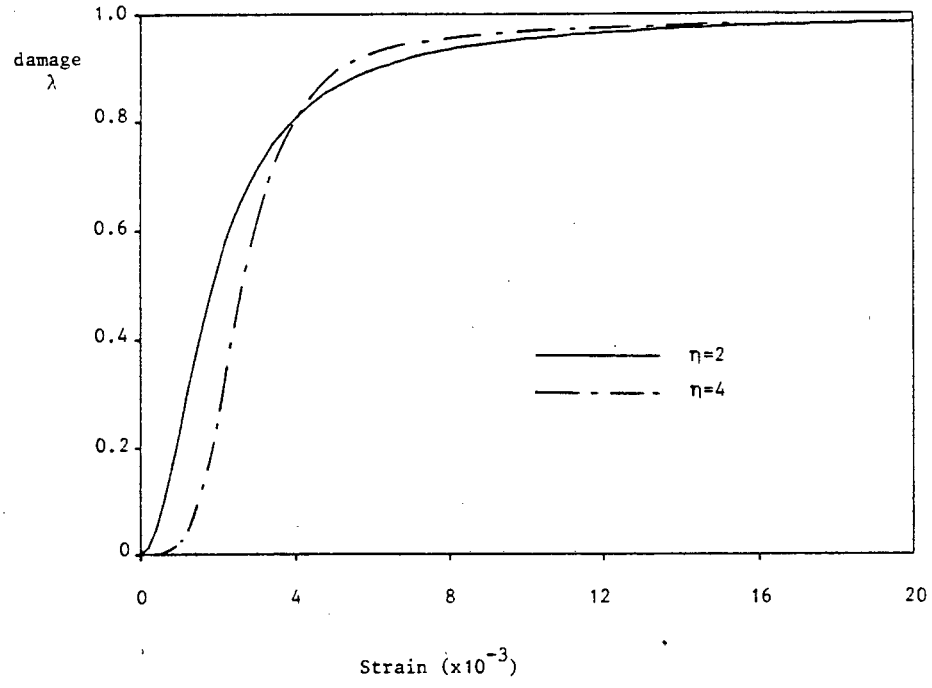

Figure 2.21(a) : Damage evolution

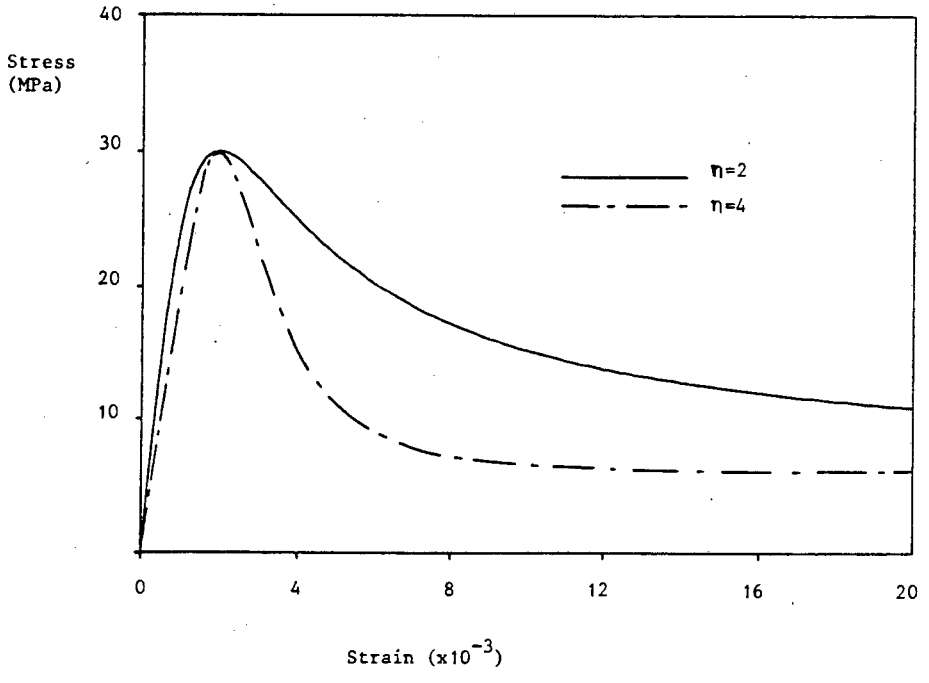

Figure 2.21(b) : Stress-strain response

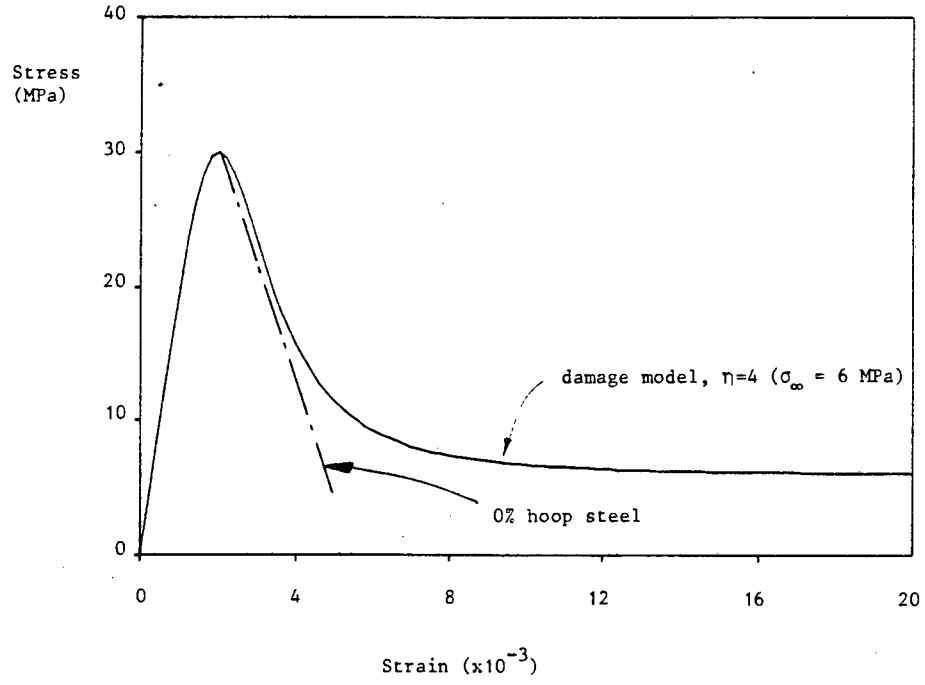

Figure 2.22 : Damage model for unconfined concrete

Unloading and reloading until further damage occurs, is defined by equations (2.10) and (2.13) to take place along a line through the origin and with a slope $E(1 - \lambda)$. This can be considered a good approximation for strains less than ϵ_m . However, at larger strains, confined concrete behaves with some ductility as illustrated in Figure 2.23. An option was included in the damage model to allow unloading to take place along a line joining the point on the monotonic stress-strain curve at which the maximum strain ϵ_r has occurred, and a point on the zero stress axis with a strain of ϵ_p . Figure 2.24 illustrates this unloading relationship. The strain ϵ_p is calculated from the following relation suggested by Karsan and Jirsa [16],

$$\frac{\epsilon_p}{\epsilon_m} = 0.15 \left[\frac{\epsilon_r}{\epsilon_m}\right] + 0.1 \left[\frac{\epsilon_r}{\epsilon_m}\right]^2 \qquad (2.21)$$

where ϵ_m and ϵ_r are as defined previously.

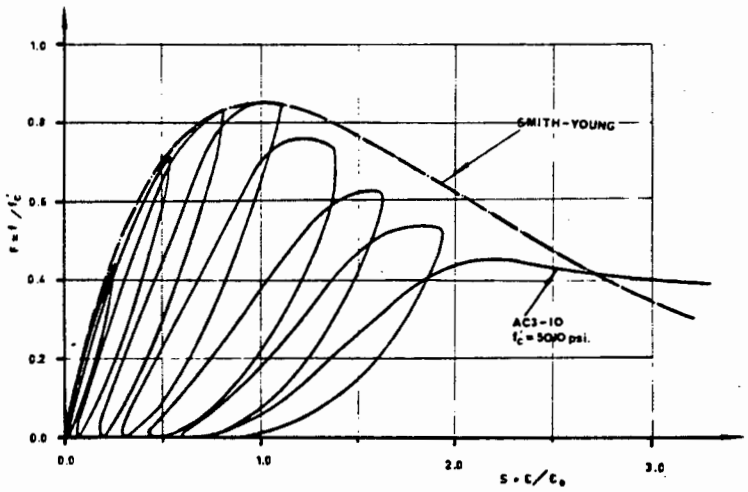

Figure 2.23 : Cyclic stress-strain response for concrete, from [16]

An important issue for a constitutive concrete model is the question of numerical efficiency. Numerical difficulties can be experienced when sudden changes in the slope of the stress-strain curve occur without a change in the sign of the strain rate. Such a change occurs at point B illustrated in Figure 2.24, when going from point A to point C. One solution is to use

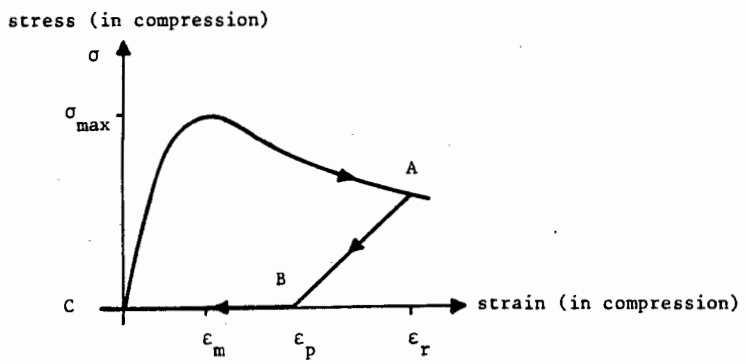

Figure 2.24 : Unloading relationship in compression

very small increments during the analysis; however, this places an unnecessary restriction on the numerical applications. An alternative solution is to use a transition curve as illustrated in Figure 2.25. Such a transition curve, based on similar transitions in the Menegotto-Pinto steel model, was included in the constitutive model. The transition curve has an added advantage in that it models the actual behaviour more accurately.

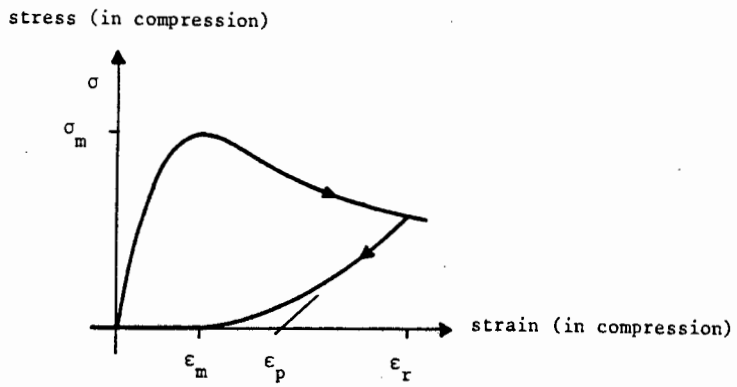

Figure 2.25 : Transition curve for unloading and reloading in compression

2.4 Bond Stress-Slip Constitutive Model for Steel-Concrete Interaction

The effectiveness of reinforced concrete as a composite material lies in the transfer of stresses between the reinforcing steel and the concrete. The stress transfer mechanism is generally described as the bonding between the steel and concrete. The term 'bond stress' is used to describe the somewhat complicated 'shear stress' state which exists in the boundary layer of concrete around the steel bar. It is in this boundary that a large proportion of the stress transfer occurs. The components of stress transfer are best explained by the illustration in Figure 2.26, where the steel, concrete and bond stress distributions are shown for an axially loaded reinforced concrete member.

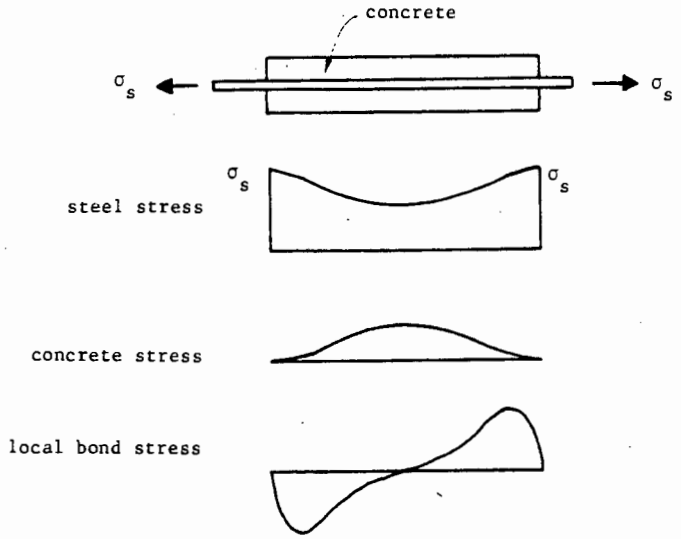

Figure 2.26 : Stress distributions for reinforced concrete member illustrating stress transfer

Numerous experimental studies have been conducted in order to understand the mechanics of the steel-concrete interaction, see for example [35-37, 54-58]. The results of these investigations are best summarised by describing the response of a single bar embedded in the centre of a concrete beam. The bar is loaded at one end, with the slip ω , measured at the same end. The bond stress q, is calculated as

$$q = \frac{P}{\Psi_o \ell} \qquad (2.22)$$

where P is the applied load,

Ψ_o is the circumference of the bar, and

ℓ is the embedded length of the bar.

In the initial stages of loading, bond is provided by the frictional resistance, chemical adhesion and the concrete resisting the movement of the lugs [59,60]. During this stage the concrete between the lugs remains

essentially intact. Microcracks develop in the concrete around the lugs of the steel bar. As the load is increased monotonically, these microcracks coalesce to form internal axisymmetric cracks which propagate from the lugs of the steel bar. These inclined cracks, shown in Figure 2.27(a), were studied in detail by Goto [37]. The nonlinear bond stress-slip relationship corresponding to this loading stage is illustrated in Figure 2.27(a). The continuous stiffness degradation which occurs is clearly evident.

The internal cracks start to close when the load is removed. However, they do not close completely and there is some residual slippage. This slippage is the result of inelastic deformation of the concrete and some friction between the concrete and steel. Figure 2.27(c) shows the unloaded bar with the corresponding bond stress-slip response indicated by the solid line.

When the load is reversed there is initially some bond resistance, mainly due to steel-concrete friction. Once this resistance has been overcome, considerable slip occurs before any further resistance is encountered. This slip is the result of the lugs moving in the gap which was created during the first loading stage. The internal cracks which developed in the first loading stage are now completely closed. As the load is increased in the reverse direction, internal cracking develops in a manner similar to the first loading stage. These cracks develop in the direction normal to the principal tensile stress and the first set of internal cracks as shown in Figure 2.27(c). The bond stress-slip response is indicated by the solid line in Figure 2.27(c). The concrete is now weaker as a result of all the cracking which has occurred. This is evident from the maximum bond stress in the reverse direction which is generally lower than the corresponding stress in the first loading direction.

Results for another cycle of loading are shown in Figure 2.27(d). Again considerable slip occurs in the initial stage, until the lugs make contact with the concrete. By this stage the concrete between adjacent lugs has broken up (see shaded region in Figure 2.27(d)) and provides less resistance than in the previous cycle. Again, there is a resulting loss of strength in the concrete, evident from the corresponding bond stress-slip diagram. This loss of strength is dependent on the amount of slip which occurred in the previous cycle; the greater the slip the more significant the loss of strength.

After a number of cycles of reversed loading, the concrete between adjacent lugs is loosened and considerable crushing of the concrete occurs. This crushed concrete provides little bond resistance and the bar is able to move freely when loaded. A typical experimental result which illustrates the gradual bond deterioration due to cyclic loading is given in Figure 2.28.

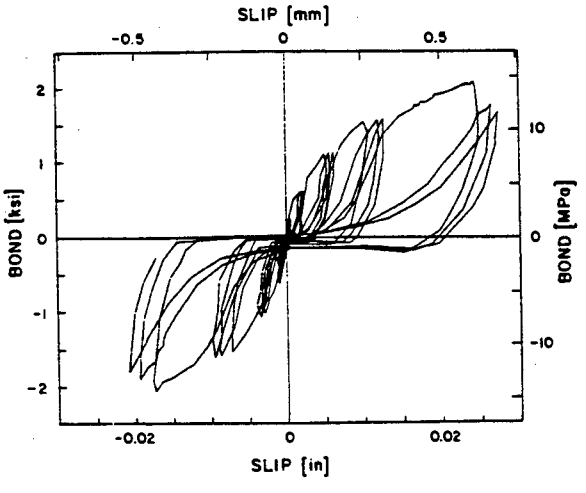

Figure 2.28 : Experimental bond stress-slip results, from [6]

A number of factors have been found to effect the bond strength and degradation. Naturally, the loading history is most important; Ma *et al*

[33] and Eligehausen *et al* [58] give details of how this is manifested. Other factors which can play an important role are; the bar size, the lug spacing and geometry, the concrete properties and the concrete cover. Details of the effects that these factors have on the bond stress-slip response are discussed in the following description of the bond stress-slip constitutive model.

Following the results of an experimental program in which the behaviour of anchored bars subjected to cyclic loading was studied, (see [56] and [58]), a general analytical model was proposed by Eligehausen *et al* [58]. One of the primary concerns of this experimental program was the simulation of the bonding in well confined concrete in accordance with seismic design provisions. The analytical model provided results which agreed well with the experimental results. This model with some modifications has been used successfully in subsequent research, see for example [18,36].

The bond stress-slip relation used in this study contains the essential features of the model proposed by Eligehausen *et al* [58], with some simplifications which make it computationally more attractive. The modified analytical model is now described.

For monotonic loading, the bond stress-slip response in indicated by the curve OABC in Figure 2.29. This curve is sometimes referred to as the 'monotonic loading envelope'. In this thesis, the monotonic response is identical for loading in either the positive or negative directions for well confined concrete and also for unconfined concrete. The monotonic envelope is described as a series of piecewise functions in [58]. Here it is represented in terms of a damage mechanics based model. This choice is appropriate since the bond stress-slip response is essentially controlled by

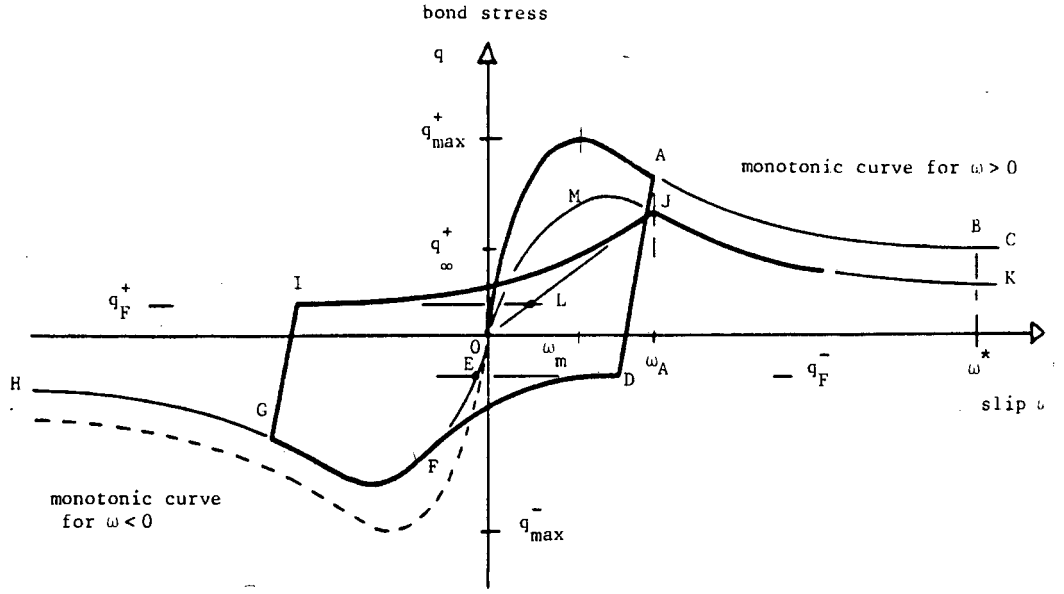

Figure 2.29 : Analytical bond stress-slip relationship

the fracturing of the concrete. The model is fundamentally the same as that described in section 2.3 for concrete. Two damage parameters λ^+ and λ^- are required to fully describe the possible bond stress-slip response, the slip $\omega > 0$ and $\omega < 0$ respectively. For clarity, λ is considered only for the case $\omega \geq 0$, i.e. $\lambda = \lambda^+$ in the following discussion. The extension to the case $\lambda = \lambda^-$ for $\omega < 0$ is straightforward.

The bond stress-bond slip relationship is given as

$$q = E_q(1 - \lambda)\omega \qquad (2.23)$$

where E_q is the initial stiffness and the other variables are as previously defined.

The rate form of equation (2.13) is written as

$$\dot{q} = E_q(1 - \lambda)\,\dot{\omega} - E_q\,\dot{\lambda}\,\omega \qquad (2.24)$$

where $\dot{\lambda} > 0$ for $\lambda = \lambda^{max}$, $\omega > 0$;

$\dot{\lambda} = 0$ otherwise

and $\dot{\omega}$ is the rate of slip.

The rate at which damage occurs $\dot{\lambda}$, is given by an evolution equation of the form

$$\dot{\lambda} = \dot{\lambda}\,(\omega, \dot{\omega}, b_i) \qquad (2.25)$$

where b_i are constants used to define the monotonic bond stress-bond slip relationship.

A rational function identical in form to equation (2.18) is used to describe the damage evolution :

$$\lambda = \frac{b_1\,\omega^2}{1 + b_2\,\omega + b_1\,\omega^2} \qquad (2.26)$$

where b_1 and b_2 are constants.

The constants b_1 and b_2 are determined using the bond stress q_{max} and corresponding slip ω_m , as well as the bond stress q_∞ . These quantities are defined in Figure 2.29.

This form of damage evolution results in a monotonic bond stress-slip relationship which corresponds closely with the actual behaviour as shown in Figure 2.30.

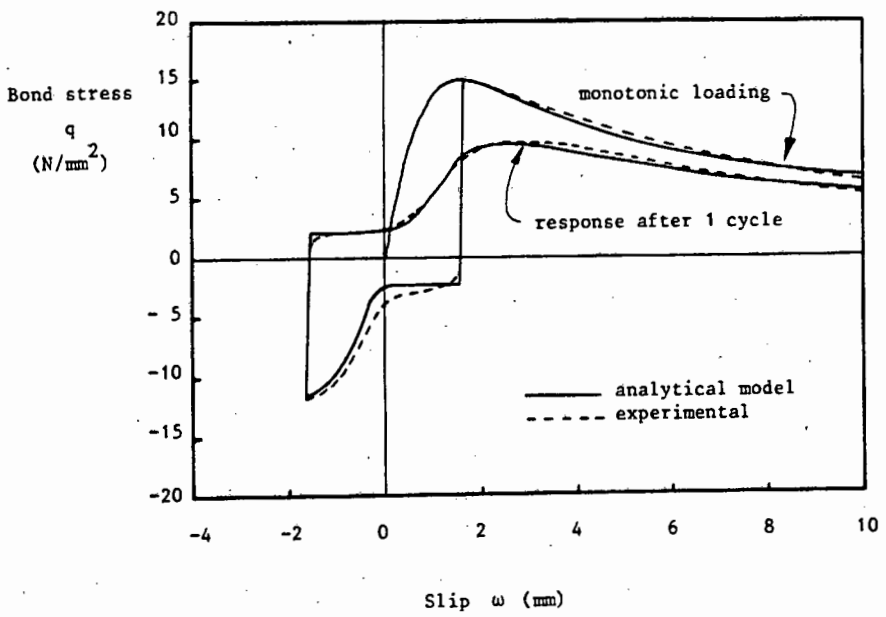

Figure 2.30 : Response of analytical model - 1 cycle

When the loading is reversed, the response follows a stiff linear unloading curve until a bond stress of q_F^- is reached in the reverse direction, line AD in Figure 2.29. q_F^- is the frictional bond resistance for loading in the negative direction. Further slip occurs in the negative sense with the bond stress remaining constant until a curve similar to the monotonic loading curve is reached. This is indicated by the path DEFGH in Figure 2.29. The numerical implementation of changing from path DE to path EFGH not only required small increments in load, but also provided convergence problems under load controlled tests. To overcome these difficulties a transition curve was included so that the response followed the path DF as shown in Figure 2.29. The curve was defined using equations similar to the transition curve in the steel stress-strain relationship.

The curve OEFGH is obtained from the monotonic loading curve by reducing the characteristic stresses q^{-}_{max} and q^{-}_{∞} as a result of the damage which has occurred. Experimental results have shown that the amount of damage can be expressed in terms of a damage parameter d , which is a function of the energy dissipated [36]. The damage parameter d has the form

$$d = \frac{1 - q_{max}(N)}{q_{max}} \tag{2.27}$$

where $q_{max}(N)$ is the reduced maximum bond stress.

The relationship between d and the dissipated energy is given explicitly as

$$d = 1 - e^{-1.2(\varepsilon/\varepsilon_o)^{1.1}} \tag{2.28}$$

where ε is the dissipated energy

and ε_o the normalizing energy, calculated as the energy absorbed under the monotonic loading curve up to a prescribed value, ω^* .

Campi *et al* [36] suggest that only 50% of the energy dissipated by friction be included in the calculation of ε .

For further load cycles, the transition curve is asymptotic to the straight lines IL and OJ depicted in Figure 2.29. The position of J is defined on the reduced monotonic curve OMJK , with slip equal to the maximum slip of previous load cycles of the same sign, i.e. point A in Figure 2.29.

The frictional stresses, q_F^+ and q_F^- are also reduced as a result of the load cycles. Ciampi *et al* [36] gives some complex rules for determining q_F under various loading conditions. Rather than apply these rules we chose to simplify the model by reducing q_F by a factor of 0.8 for each cycle of loading.

Values for defining the monotonic envelope curves are given by Filippou *et al* [18] for straight and hooked bars in confined and unconfined concrete.

A comparison of experimental results with the response predicted by the analytical bond stress-slip constitutive model is given in Figure 2.30, for monotonic loading and for 1 cycle of loading. The experimental results are obtained from Ciampi *et al* [36]. The results for the analytical model were obtained by prescribing the slip. The results show that the choice of a simple evolution law for the monotonic loading is a good one. The results obtained after 1 cycle of loading compare favourably with [36].

The experimental and analytical results after 10 cycles of loading are compared in Figure 2.31. The analytical model shows the correct trends, although the results differ slightly after 10 cycles. The parameters which influence the rate of degradation of the monotonic loading curve are ω^* and the proportion of frictional energy included in the dissipated energy ε. The choice of this proportion, (50% was used here), and the choice of ω^* for calculating the normalizing energy, ε_o, are both parameters which can easily influence the rate of degradation, especially in the first few cycles. In view of the objectives of this thesis, the results obtained by the analytical model are considered to be acceptable.

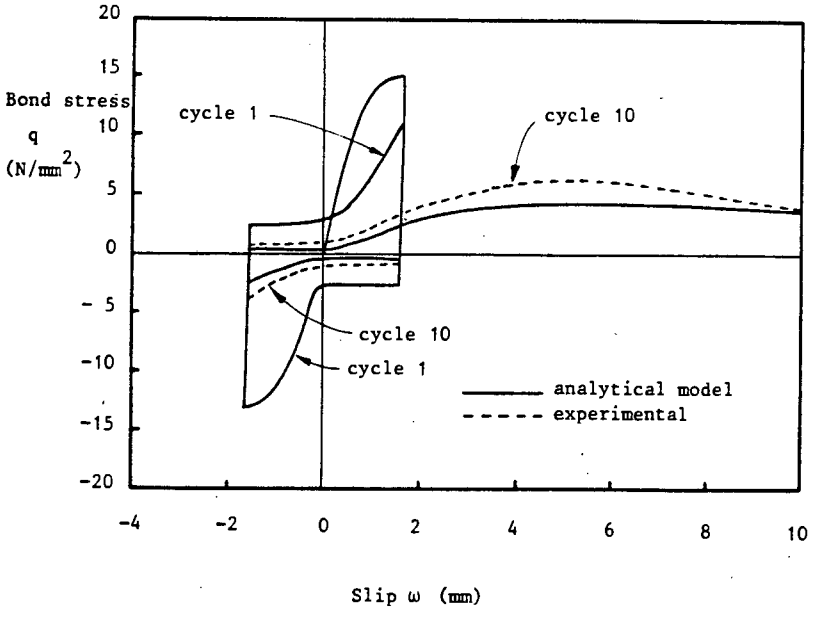

Figure 2.31 : Response of analytical model - 10 cycles

CHAPTER 3

ANALYTICAL MODEL FOR REINFORCED CONCRETE MEMBERS

Simulating the response of reinforced concrete structures which are subjected to large cyclic loads is not a simple procedure when considering the complex mechanisms involved which result in permanent damage. Analytical models of varying degrees of sophistication are available for this task. Two fundamental aspects need to be addressed for any analytical model. They are, first, the assumptions concerning the distribution of stiffness along the member and second, the hysteretic force-deformation relationship at any section of the member. This chapter starts by reviewing how these aspects have been considered in previous studies. Following this discussion, a layered beam element model is proposed. The objective of this model is to simulate the stiffness degradation with as few layers as possible and in a numerically efficient manner. The analytical formulation for the model as well as the numerical procedures used, are included in this chapter.

3.1 Previous Analytical Models

The discussion in Chapter 2 highlights some of the more important factors affecting the stiffness degradation and inelastic response of reinforced concrete members subjected to cyclic loading. This section reviews some of the analytical models which have been developed in an attempt to simulate this response. The objective of this review is to clearly reflect the capabilities and limitations of existing models and is by no means comprehensive. Otani [9], Keshararzian *et al* [15] and Mercer and Martin [17] provide more detailed reviews.

Clough [62] developed one of the first analytical models for reinforced concrete members. The model is called the two component model and consists of two parallel elements, one elastic and the other elastoplastic. These two elements are connected at their ends as illustrated in Figure 3.1. Once the yield moment is reached, a plastic hinge develops at that end of the

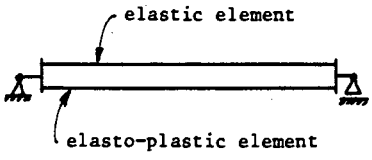

Figure 3.1 : Two component model

elastoplastic element. The disadvantage of this model lies in its restriction to bilinear moment-rotation hysteresis characteristics. Bilinear hysteresis models have an inherent problem in that they overestimate the energy dissipation capacity of reinforced concrete members.

The one component model proposed by Giberson [63] consists of an elastic element with inelastic rotational springs attached at each end as shown in Figure 3.2. The purpose of the springs is to simulate the inelastic deformation occurring near the ends of the reinforced concrete beams. An

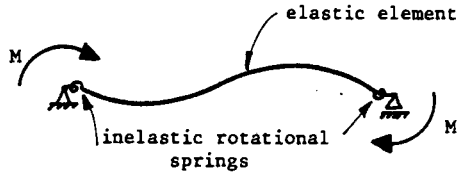

Figure 3.2 : One component model

attractive feature of this model is the ability to use stiffness degrading hysteretic models for the inelastic spring characteristics. The hysteretic models consist of a set of empirical rules to define the force-deformation relationship, in particular the moment-rotation relation for the inelastic springs. Clough [64] modified the bilinear model to include stiffness degrading characteristics as illustrated in Figure 3.3. This model is simple and has been used extensively. More elaborate hysteretic models have been developed, such as the Takeda model [65], illustrated in Figure 3.4.

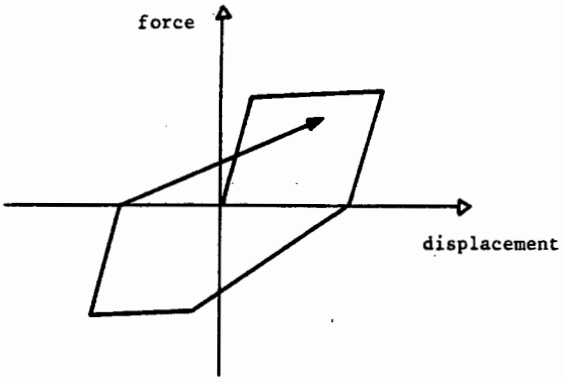

Figure 3.3 : Clough's hysteresis model

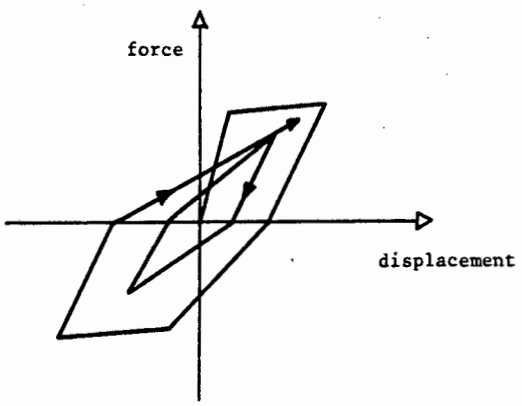

Figure 3.4 : Takeda hysteresis model

The Takeda model has been modified to include pinching action and strength decay, both due to bar-slippage and shear degradation [66]. In addition to a set of rules, the primary curve must be defined for the hysteretic model. The primary curves are generally based on the monotonic moment-curvature response for a particular section of the beam. For the one component model this moment-curvature response is usually approximated by a bilinear curve. Using this approximation and by assuming that the point of contraflexure remains fixed, a bilinear moment-rotation relation can be obtained as the primary curve for the inelastic rotational springs. Further details are given in Banon *et al* [7]. An inherent danger exists when using hysteresis

models of this nature. Although the models have in a sense been generalized, they cannot account for variations of all the major components or parameters and their interaction which affect the response of the beam. This introduces an element of uncertainty which must be recognised when using empirical force-deformation hysteresis models.

Bar slippage and shear deformation have been included in the one component model as additional inelastic springs at the ends of the member [7]. Each of these springs have independent moment-rotation hysteresis models. A disadvantage of the one component model is that the inelastic rotation at an end is only determined by the moment at that end and not on the curvature distribution along the member or moment at the other end of the member. In addition, by lumping the inelastic deformation at the ends of the beam, the model does not simulate the spread of inelastic deformation along the beam. The use of the one component model is thus restricted to members with nonlinearities localized at the ends of the member and with an inflection point which remains near the centre of the beam.

The effect of distributed inelastic deformation along the member has been included in line element models in various ways. In the multiple spring model [66,67], the beam is divided into segments of constant stiffness. Each segment is represented by an inelastic spring as illustrated in Figure 3.5. In another model, the beam is divided into three sections, an elastic zone and two variable length inelastic zones at the ends [68,69]. The lengths of the inelastic zones are calculated from a linear bending moment distribution. A hysteresis model is used to define the moment-curvature response of the inelastic zone.

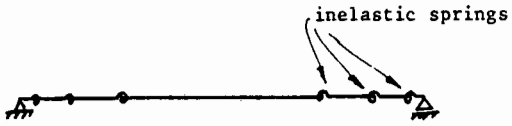

Figure 3.5 : Multiple spring model

An empirical force-deformation relationship to control the stiffness degradation of members is used in all of the models discussed thus far. More refined models have been developed which include the stiffness degradation on a more rational basis. These include layered beam models and finite element models.

Layered models, sometimes referred to as fibre models, consist of dividing the beam into a number of layers through its depth as shown in Figure 3.6. A linear strain distribution is assumed through the depth of the member. By treating each layer as an integration point with its own constitutive relation, the moment-curvature relation can be obtained for a cross section

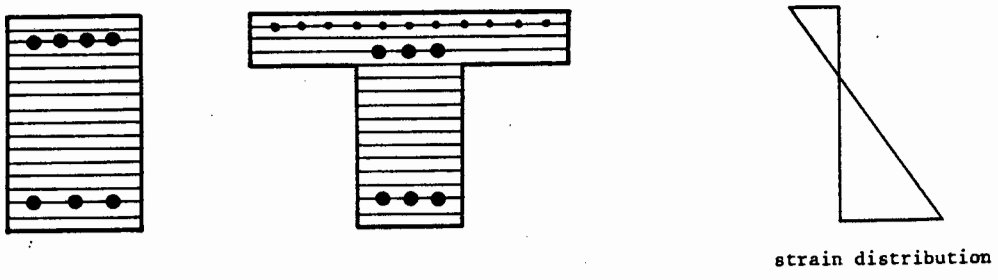

Figure 3.6 : Layered beam sections

at any point along the beam. The stiffness matrix for the member can be obtained by integrating the moment-curvature relations along the member.

The layered model has been used successfully in various studies, see for example [19,33,42,18], but the large computational demands has precluded the model from being used for design purposes. The model accounts for the spread of inelastic deformation along the member as well as the coupling between bending and axial force effects.

The application of the finite element method for the nonlinear analysis of reinforced concrete structures requires significant computing resources [7,70]. Such analyses are not performed in general for cyclically loaded frames due to the large costs involved.

3.2 Proposed Layered Beam Model

In this study an analytical beam model based on the layered approach described in section 3.1 is developed. The main advantage of such a model lies in its ability to simulate the stiffness degradation reasonably accurately as well as the spread of inelastic deformation along the beam. This particular model also seeks to give a more physical interpretation of the damage that occurs and attempts to quantify it. An important aspect in the development of such a model which is addressed in this thesis, is the efficiency and robustness of the numerical algorithms.

Beams in frames subjected to lateral loading, such as encountered during a seismic event, are subjected to double curvature bending with the inelastic deformation concentrated near their ends as described in Chapter 2. Consequently, the proposed model consists of an elastic segment for the centre of the beam, with two inelastic segments at the ends as illustrated in Figure 3.7. In the inelastic zones, the stiffness degradation response

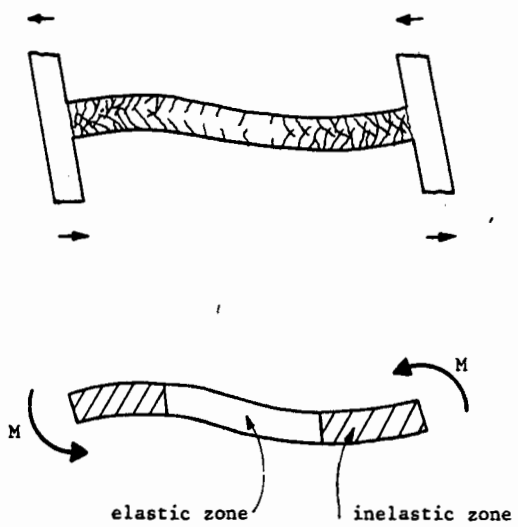

Figure 3.7 : Deformation of girder due to lateral loading of the frame

is evaluated by determining the moment-curvature relation at a number of cross sections. The position of these cross sections, or integration stations, along the beam must be fixed during an analysis. This requires the length of the inelastic zones to be specified prior to an analysis. Although some judgement is required in specifying these lengths, a simple check during the analysis will determine when moments in the elastic zone exceeds the yield moment and the necessary action may be taken. The usual assumption of a linear bending moment distribution along the beam is made. At a cross section of the beam, the moment-curvature response is obtained from the constitutive relations for the steel and concrete, and by assuming a linear strain distribution through the depth of the beam. One of the objectives of this model is to use as few layers as possible to capture the important features of the response.

The analysis of nonsymmetric sections does not present a problem for layered models. Such sections result in different stiffnesses for positive and negative bending; this effect is included in the elastic zone.

The proposed beam model includes the effects of bar-slippage in exterior beam-column joints. Bar slip results in a cracked section developing at the beam-column interface (as discussed in Chapter 2). The model accounts for the crack opening and crack closing mechanism using an approach similar to Filipou *et al* [18]. The model only simulates the effect of a crack developing at the beam-column interface; deformations resulting from other cracks are not considered. The effects of bar slip at interior beam-column connections is not considered in this thesis.

No shear deformation or related effects are included in this model. Consequently, the model can only be considered for problems in which the flexural response is dominant. Axial forces can be included but are assumed to remain constant during an analysis.

In summary, the model is based on a mixed formulation in which the internal force distribution is assumed.

3.3 Kinematics of a Cracked Beam Section

An important issue in developing a model for a cracked beam section concerns the crack closure phenomena and the activation of concrete stresses. The mechanisms at a cracked reinforced concrete section have been described in Chapter 2.

Previously, in studies such as smeared crack models, compatibility between the steel and concrete strains has been assumed [14]. A strain quantity normal to the crack is used to control the contribution of concrete to the section forces. Crack closure is defined as occurring when the strain in the concrete is in compression or is less than the strain at which the crack

opened. Accordingly, the steel is required to go into compression before the crack closes. Results from experimental tests indicate that this seldom occurs. The mechanics of this aspect have been discussed in Chapter 2.

Recently, Filippou *et al* [18] proposed that *strain increment compatibility* exists between the steel and the concrete. Briefly, the increments in steel strains and concrete strains are set equal only when the crack is closed or concrete unloading occurs. When the crack is open, the concrete strains remain 'frozen' in a state corresponding to zero concrete stress. Filippou *et al* [18] support this theory with experimental results from [13] in which the history of concrete strains near a cracked section of a cyclically loaded beam are monitored. These results are given in Figure 3.8. This method also needs to know the crack widths so that the instant of crack opening and closure can be determined.

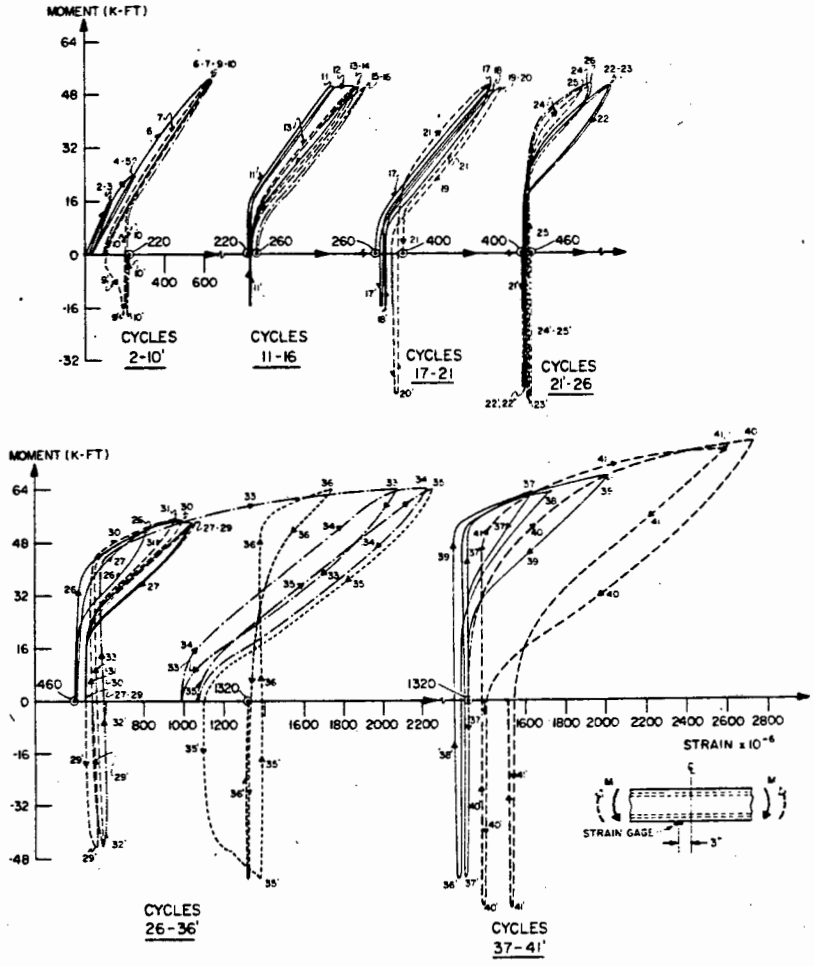

Figure 3.8 : History of concrete strains near a cracked reinforced concrete section, from [13]

The concept of strain increment compatibility is used at the ends of the proposed layered beam model where cracks at the beam-column interface are allowed to develop. The crack widths at the steel layers are defined as equal to the total bar slip on either side of the crack. This requires an analytical model which can determine the amount of bar slip that occurs. A linear distribution of crack width is assumed between the top and bottom steel layers as illustrated in Figure 3.9.

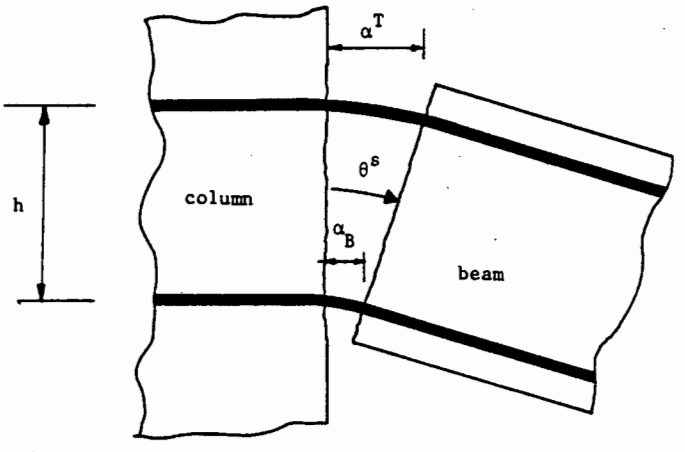

Figure 3.9 : Definition of fixed end rotation at beam-column joint

The fixed end rotation due to bar slip is defined as

$$\theta^s = \frac{\alpha^T - \alpha^B}{h} \qquad (3.1)$$

where α^T and α^B are the crack widths at the top and bottom steel layers, and are functions of the slip that occurs in the stress transfer zone either side of the cracked section

and h is the distance between the top and bottom steel layers (Figure 3.9).

Crack closure is defined as occurring when the crack width is less than a variable β , where $\beta > 0$. This is due to some shear deformation which occurs at an open crack. As the crack starts to close, the rough surfaces at the crack will not interlock in the same way as when the crack opened as a result of the shear deformation. Consequently, closure of the crack occurs at a larger crack width than when it opened. As the crack closes partial strain compatibility exists between the steel and concrete. At the same time, the stresses in the concrete tend to increase gradually and full strain compatibility exists only when the crack is completely closed. Experimental results suggest that β is a function of the maximum crack width, α_{max} [71]. The following relation is used to define the crack closure criterion [18],

$$\beta = 0.1\ \alpha_{max} + \frac{0.125}{\alpha_{max}} \quad . \tag{3.2}$$

3.4 Internal Force-Displacement Relations

The internal force-displacement relations for the layered beam element are derived for a general beam defined with ends A and B and a length of L . The length of the inelastic zone on the left of the beam is x_a and on the right x_b , as illustrated in Figure 3.10(a). The elastic zone has a length of ℓ_e where $\ell_e = L - x_a - x_b$. Points a and b define the extent of the elastic zone. The positive sign convention for the internal forces and the displacements at the ends of the beam are shown in Figures 3.10(b) and 3.10(c) respectively.

A linear bending moment distribution along the beam is assumed as shown in Figure 3.10(d). In the elastic zone, a linear curvature distribution is assumed where ϕ is used to denote the curvature. To account for nonsymmetric sections, the bending stiffness to the left of the point of

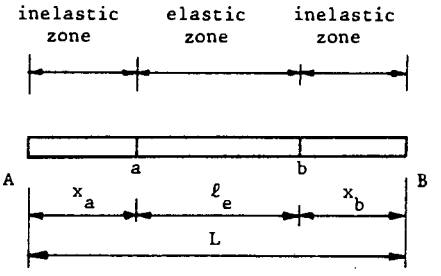

Figure 3.10(a) : Beam topology

Figure 3.10(b) : Beam end forces positive sign convention

Figure 3.10(c) : Beam end displacements positive sign convention

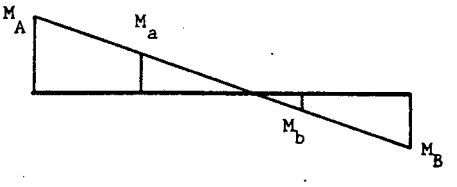

Figure 3.10(d) : Bending moment distribution

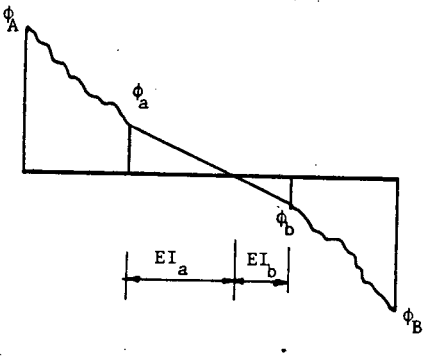

Figure 3.10(e) : Curvature distribution

contraflexure is denoted by EI_a , and to the right by EI_b . The curvature distribution in the inelastic zones is of a highly nonlinear nature as shown in Figure 3.10(e).

The convention for positive bending moment M(x) at a point x along the beam is shown in Figure 3.11, where x is measured from the end A . M(x) is given by the relation

$$M(x) = \left[\frac{x}{L} - 1\right] M_A + \frac{x}{L} M_B \quad . \tag{3.3}$$

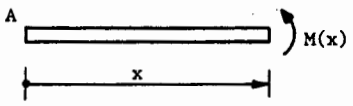

Figure 3.11 : Positive bending moment convention

The kinematic relations for the beam must include the effects of fixed end rotations. Assuming small displacements, the kinematic relations for a beam with no fixed end rotations are,

$$\theta_A = \theta_A^f + \frac{(v_B^f - v_A^f)}{L} \tag{3.4}$$

$$\theta_B = \theta_B^f + \frac{(v_B^f - v_A^f)}{L} \tag{3.5}$$

where v defines the vertical displacement in the local coordinate system,

and θ defines the rotations (small displacement assumptions are implied).

The quantities in equations (3.4) and (3.5) are defined in Figure 3.12(a), where the position of the deformed beam is defined by $A'B'$.

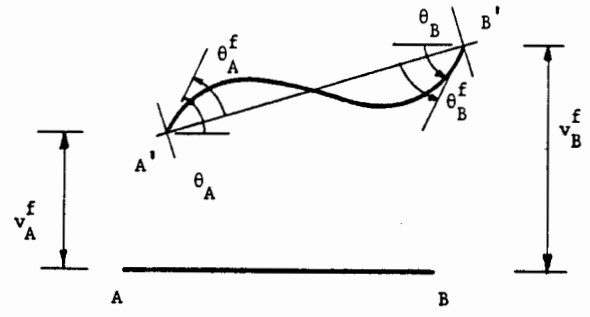

Figure 3.12(a) : Deformed beam with no fixed end rotations

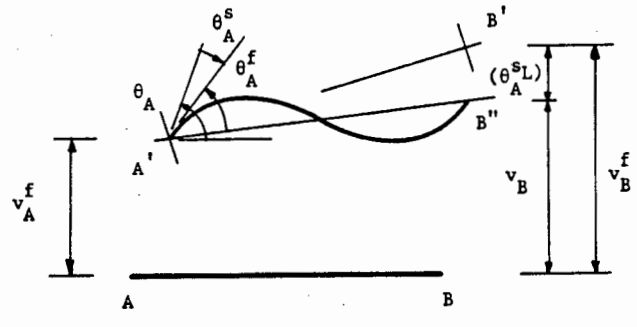

Figure 3.12(b) : Deformed beam with fixed end rotation at end A only

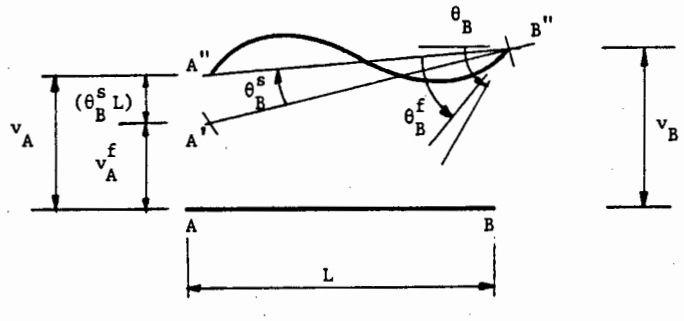

Figure 3.12(c) : Deformed beam with fixed end rotation at end B

If bar slip causes a fixed end rotation θ_A^s to develop at end A , the deformed beam is defined by A'B" in Figure 3.12(b). The fixed end rotation is chosen to be measured clockwise since a positive moment at A will result in a fixed end rotation in the clockwise sense. The vertical displacement

at B is now given by

$$v_B = v_B^f - \theta_A^s L \tag{3.6}$$

where it is assumed that the fixed end rotations θ^s are small.

Following a similar approach, the development of a fixed end rotation at B will cause end A to displace to position A'' in Figure 3.12(c). The vertical displacement at A is now given by

$$v_A = v_A^f + \theta_B^s L \tag{3.7}$$

where θ_B^s is measured clockwise.

Substituting equations (3.6) and (3.7) into equations (3.4) and (3.5), the kinematic relations for the beam which include the fixed end rotations are obtained :

$$\theta_A = \theta_A^f + \frac{(v_B - v_A)}{L} + (\theta_A^s + \theta_B^s) \tag{3.8}$$

$$\theta_B = \theta_B^f + \frac{(v_B - v_A)}{L} + (\theta_A^s + \theta_B^s) \tag{3.9}$$

The strain-displacement relations are obtained by adopting the Euler-Bernoulli theory assumptions. For the inelastic zones we have,

$$\theta_A^f = \theta_a - \int_A^a \phi \, dx \tag{3.10}$$

$$\theta_B^f = \theta_b - \int_b^B \phi \, dx \tag{3.11}$$

where θ_a and θ_b are the rotations relative to the centroidal axis of the deformed beam $\ddot{A}\ddot{B}$, (Figure 3.13)

and ϕ is the curvature.

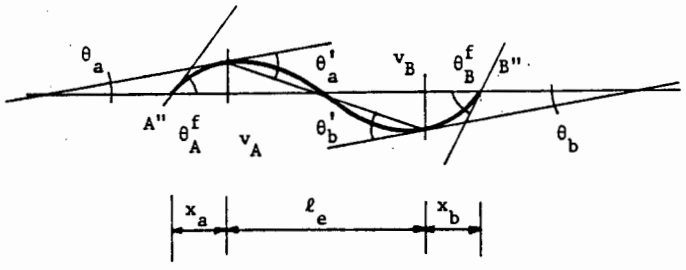

Figure 3.13 : Deformed beam showing kinematic relations for elastic zone

The displacements of the deformed beam relative to the centroidal axis in the deformed configuration $\ddot{A}\ddot{B}$ as shown in Figure 3.13.

By considering the geometry in Figure 3.13, the following relations are obtained,

$$\theta_a = \theta'_a + \frac{(v_b - v_a)}{\ell_e} \tag{3.12}$$

$$\theta_b = \theta'_b + \frac{(v_b - v_a)}{\ell_e} \quad . \tag{3.13}$$

The displacements v_a and v_b, which are defined in Figure 3.13, are obtained by integrating the relation $\frac{dv}{dx} = \theta$, (from the Euler-Bernoulli assumptions). The displacements are expressed as follows :

$$v_a = \int_A^a \theta \, dx \tag{3.14}$$

$$v_b = -\int_b^B \theta \, dx \quad . \tag{3.15}$$

By substituting equations (3.12) - (3.15) into equations (3.10) and (3.11), the following relations are obtained,

$$\theta_A^f = \theta_a' - \int_A^a \phi \, dx - \frac{1}{\ell_e}\left\{\int_A^a \theta \, dx + \int_b^B \theta \, dx\right\} \tag{3.16}$$

$$\theta_B^f = \theta_b' - \int_b^B \phi \, dx - \frac{1}{\ell_e}\left\{\int_A^a \theta \, dx + \int_b^B \theta \, dx\right\} \tag{3.17}$$

The internal force-displacement relations for the elastic zone of a beam in which the section is nonsymmetric, are derived using simple beam theory and given as :

$$\theta_a' = \frac{(M_a^2(2M_a + 3M_b)EI_b - M_b^3 EI_a)}{6EI_a EI_b (M_a + M_b)^2}\ell_e \tag{3.18}$$

$$\theta_b' = \frac{(M_b^2(2M_b + 3M_a)EI_a - M_a^3 EI_b)}{6EI_a EI_b (M_a + M_b)^2}\ell_e \tag{3.19}$$

where $$M_a = \left[1 - \frac{x_a}{L}\right]M_A - \frac{x_a}{L} M_B \quad , \tag{3.20}$$

$$M_b = \left[1 - \frac{x_b}{L}\right]M_B - \frac{x_b}{L} M_A \quad , \tag{3.21}$$

and EI_a, EI_b are as defined in Figure 3.10(e).

For symmetric sections, equations (3.18) and (3.19) reduce to

$$\theta_a' = \frac{(2M_a - M_b)}{6EI}\,\ell_e \qquad (3.22)$$

$$\theta_b' = \frac{(2M_b - M_a)}{6EI}\,\ell_e \qquad (3.23)$$

respectively, where $EI = EI_a = EI_b$.

To complete the internal force-displacement relations for the beam, the integrals in equations (3.16) and (3.17) need to be expressed in terms of the end moments, M_A and M_B . Numerical integration is used to determine these integrals. Simpson's one-third rule is used for the numerical integration, not only because of its simplicity, but also because it can integrate a cubic polynomial exactly. This means that for an elastic beam with a linear moment distribution, only three integration points along the 'inelastic' zone of the beam are needed to obtain the 'exact' displacements.

For the integrals from A to a , the function f is used to represent both the curvatures ϕ , and rotations θ in Figure 3.14(a). The interval x_a is subdivided into n equal intervals, (where n is an even number). The integrals can be expressed as functions Π of the form :

$$\int_A^a \phi \, dx = \Pi(n, x_a, \phi_i) \quad , \qquad 0 \leq i \leq n \qquad (3.24)$$

$$\int_A^a \theta \, dx = \Pi(n, x_a, \theta_i) \quad , \qquad 0 \leq i \leq n \qquad (3.25)$$

Also, $$\theta_i = \theta_A^f + \int_A^i \phi \, dx \quad . \tag{3.26}$$

Therefore equation (3.25) reduces to

$$\int_A^a \theta \, dx = \Pi^*(n, x_a, \phi_i) + x_a \, \theta_A^f \quad , \qquad 0 \leq i \leq n \quad . \tag{3.27}$$

The detailed form of these functions is given in Appendix A.

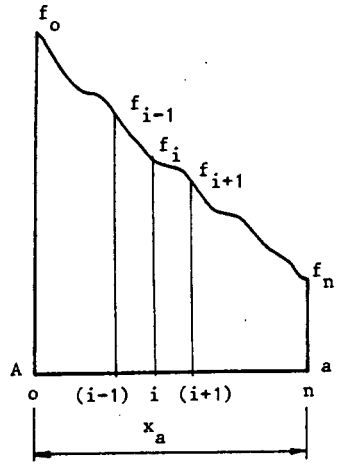

Figure 3.14(a) : Integration stations for inelastic zone A-a

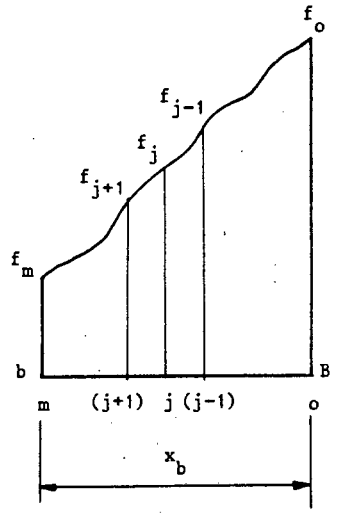

Figure 3.14(b) : Integration stations for elastic zone b-B

Similar expressions can be obtained for the integrals from b to B for the function f in Figure 3.14(b). This interval is subdivided into m equal intervals. The integrals are expressed as

$$\int_b^B \phi \, dx = \Pi(m, x_b, \phi_j) \quad , \qquad 0 \leq j \leq m \tag{3.28}$$

$$\int_b^B \theta \, dx = \Pi^*(m, x_b, \phi_j) + x_b \, \theta_B^f \quad , \qquad 0 \leq j \leq m \quad . \tag{3.29}$$

Further details of these functions are given in Appendix A.

The moment-curvature relationship at the integration stations i and j , $(0 \leq i \leq n \; ; \; 0 \leq j \leq m)$, is discussed in section 3.5.

Substituting equations (3.24), (3.27), (3.28) and (3.29) into equations (3.16) and (3.17) results in the following equations :

$$\left[1 + \frac{x_a}{\ell_e}\right]\theta_A^f + \frac{x_b}{\ell_e}\theta_B^f = \theta_a' + \Omega(\phi_i,\phi_j) \qquad \begin{matrix} 0 \leq i \leq n \\ 0 \leq j \leq m \end{matrix} \quad , \tag{3.30}$$

$$\frac{x_a}{\ell_e}\theta_A^f + \left[1 + \frac{x_b}{\ell_e}\right]\theta_B^f = \theta_b' + \Omega(\phi_i,\phi_j) \qquad \begin{matrix} 0 \leq i \leq n \\ 0 \leq j \leq m \end{matrix} \quad , \tag{3.31}$$

where $\Omega(\phi_i,\phi_j)$ is a function in terms of x_a, x_b, n, m (see equations (A.5) and (A.6) in Appendix A).

Equations (3.30) and (3.31) can be written in matrix form as

$$[H]\,\underset{\sim}{\theta}^f = \underset{\sim}{\theta}' + [G]\,\underset{\sim}{\phi} \tag{3.32}$$

where $\underset{\sim}{\theta}^f = [\theta_A^f \; , \; \theta_B^f]^T$,

$\underset{\sim}{\theta}' = [\theta_a' \; , \; \theta_b']^T$,

$\underset{\sim}{\phi} = [\phi_i,\phi_j]^T$, $\quad 0 \leq i \leq n \quad , \quad 0 \leq j \leq m$

$$[H] = \begin{bmatrix} 1 + \dfrac{x_a}{\ell_e} & \dfrac{x_b}{\ell_e} \\ \dfrac{x_a}{\ell_e} & 1 + \dfrac{x_b}{\ell_e} \end{bmatrix} \quad ,$$

and [G] contains integration constants in terms of x_a, x_b , n, m and ℓ_e .

Equations (3.30) and (3.31) can be uncoupled by reducing equation (3.32) as follows :

$$\underset{\sim}{\theta}^{f} = [H]^{-1}\ \underset{\sim}{\theta}' + [H]^{-1}\ [G]\ \underset{\sim}{\phi} \tag{3.33}$$

or,

$$\underset{\sim}{\theta}^{f} = [H^{*}]\ \underset{\sim}{\theta}' + [G^{*}]\ \underset{\sim}{\phi} \tag{3.34}$$

where $[H^{*}] = [H]^{-1}$ and $[G^{*}] = [H]^{-1}\ [G]$.

Finally, by writing equations (3.8) and (3.9) in matrix form and substituting into equation (3.34), the internal force-displacement relations for the beam are obtained;

$$\underset{\sim}{\theta} = [H^{*}]\ \underset{\sim}{\theta}' + [E]\ \underset{\sim}{v} + [D]\ \underset{\sim}{\theta}^{s} + [G^{*}]\ \underset{\sim}{\phi} \tag{3.35}$$

where $\underset{\sim}{\theta} = [\theta_A\ ,\ \theta_B]^T$,

$\underset{\sim}{v} = [v_A\ ,\ v_B]^T$,

$\underset{\sim}{\theta}^{s} = [\theta_A^{s}\ ,\ \theta_B^{s}]$,

$$[E] = \begin{bmatrix} -1 & 1 \\ & \\ -1 & 1 \end{bmatrix} ,$$

$$[D] = \begin{bmatrix} 1 & 1 \\ & \\ 1 & 1 \end{bmatrix} ,$$

with $\underset{\sim}{\theta}'$, $[H^{*}]$, $[G^{*}]$, $\underset{\sim}{\phi}$ as defined above.

θ_a' and θ_b' are given by equations (3.18) and (3.19).

3.5 Moment-Curvature Relationship

The cross section of a typical reinforced concrete beam cross section is illustrated in Figure 3.15. The depth of the beam is d^* and the width b^*. The concrete is divided into a total of N_c layers. Associated with each layer are its area A_c^j and height above the bottom of the beam d^j, where the superscript j denotes the j-th layer. The top reinforcing steel has an area A_s^T and height d^T, and the bottom reinforcement A_s^B and d^B respectively. h is the distance between the top and bottom reinforcement. A T-section can also be specified with the above information.

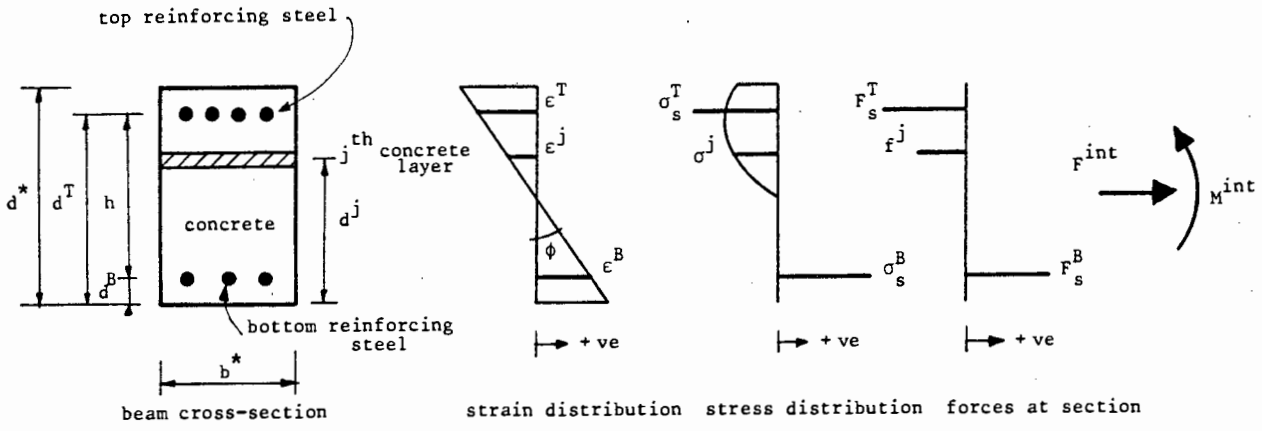

Figure 3.15 : Definition of quantities at a typical section

The strains at the top and bottom steel layers, ϵ^T and ϵ^B respectively, are used to define the curvature at the section, as shown in Figure 3.15.

$$\phi = \frac{\epsilon^B - \epsilon^T}{h} \tag{3.36}$$

Assuming a linear strain distribution, the strain at the j-th layer is given as

$$\epsilon^j = \frac{(d^j - d^B)}{h} \epsilon^T + \frac{(d^T - d^j)}{h} \epsilon^B \quad . \tag{3.37}$$

The stress at each layer is defined by the constitutive relation for the layer. The resulting stress distribution shown in Figure 3.15, assumes the concrete has no strength in tension.

The calculation for the forces in each layer is straightforward. The internal forces at the section are computed as follows :

$$F^{int} = \sum_{j=1}^{N_c} f^j + F_s^T + F_s^B \tag{3.38}$$

$$M^{int} = \sum_{j=1}^{N_c} \left[\frac{d^*}{2} - d^j\right] + F_s^T \left[\frac{d^*}{2} - d^T\right] + F_s^B \left[\frac{d^*}{2} - d^B\right] \quad . \tag{3.39}$$

In these calculations, it is assumed that for a nonsymmetric section there is no initial axial force present, as is typically the situation in girders of a frame structure. However, columns usually have symmetric sections; in this case axial forces are present and equation (3.39) holds.

In the context where the moment-curvature response is required for the layered beam model, the bending moment at the section is known and the curvature must be determined. The equilibrium equations at the section are in this case given in matrix form as

$$\begin{Bmatrix} F^{int} \\ M^{int} \end{Bmatrix} = \begin{bmatrix} F^* \\ M^* \end{bmatrix}$$

or $\underset{\sim}{F}^{int} = \underset{\sim}{F}^*$

where F^* is the initial axial force,

and M^* is the prescribed moment.

The positive convention for these internal forces at a section along the beam is given in Figure 3.16.

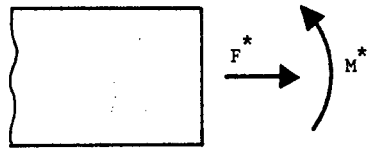

Figure 3.16 : Positive sign convention for forces applied at a section

Various numerical procedures have been adopted in previous studies to solve the strain distribution or curvature if the moment is prescribed, or to solve for the moment given the curvature.

Park and Paulay [4] use an iteration scheme in which the neutral axis is adjusted until equilibrium is achieved. This method presents problems when the curvature is close to zero. Ma *et al* [33] prescribed the curvature and used a numerical scheme based on the bisection method.

In this study, Newton's method is used to solve the set of nonlinear equations given in equation (3.40). The strain quantities ϵ^T and ϵ^B are chosen as the independent variables. Equation (3.40) is cast in the form

$$\underset{\sim}{\Psi} = \begin{Bmatrix} \Psi_1 \\ \Psi_2 \end{Bmatrix} = \begin{bmatrix} F^* - F^{int} \\ M^* - M^{int} \end{bmatrix} = \underset{\sim}{F}^* - \underset{\sim}{F}^{int} \qquad (3.41)$$

where Ψ_1 and Ψ_2 are the residuals.

The strain vector is defined as

$$\underset{\sim}{\epsilon} = \begin{Bmatrix} \epsilon^T \\ \epsilon^B \end{Bmatrix} \quad . \tag{3.42}$$

Equilibrium is achieved when the residuals in equation (3.41) are less than some specified tolerance.

1. Calculate $\underset{\sim}{\psi}^o = (\underset{\sim}{F}^*)_{t+\Delta t} - (\underset{\sim}{F}^{int})_t$
2. Set iteration loop counter i=0
3. Start iteration loop i = i+1
4. Calculate $[J]^i$
5. Solve $[J]^i \, \Delta\underset{\sim}{\epsilon}^i = - \underset{\sim}{\psi}^i$
6. Update strains $\Delta\underset{\sim}{\epsilon}^{i+1}_{t+\Delta t} = \Delta\underset{\sim}{\epsilon}^{i}_{t+\Delta t} + \Delta\underset{\sim}{\epsilon}^{i}$

   $$\underset{\sim}{\epsilon}^{i+1}_{t+\Delta t} = \underset{\sim}{\epsilon}_t + \Delta\underset{\sim}{\epsilon}^{i+1}_{t+\Delta t}$$
7. Determine $(\underset{\sim}{F}^{int})^{i+1}_{t+\Delta t}$
8. Calculate $\underset{\sim}{\psi}^{i+1} = (\underset{\sim}{F}^*)_{t+\Delta t} - (\underset{\sim}{F}^{int})^{i+1}_{t+\Delta t}$
9. Check $\underset{\sim}{\psi}^{i+1}$ for convergence
   Return to step 3 if solution has not converged
10. Calculate curvature $\phi_{t+\Delta t} = \dfrac{(\epsilon^B)_{t+\Delta t} - (\epsilon^T)_{t+\Delta t}}{h}$

Table 3.1 : Newton scheme to obtain moment-curvature relationship

The moment-curvature response is computed at specified time increments. Assume that the solution is known at time t ; i.e. we know the strains $(\epsilon^T)_t$ and $(\epsilon^B)_t$. At time t+Δt the prescribed bending moment is $(M^*)_{t+\Delta t}$. The curvature at time t+Δt is computed using the Newton iteration scheme given in Table 3.1.

The Jacobian matrix [J] in Table 3.1 is defined as

$$[J]^i = \begin{bmatrix} \dfrac{\partial \Psi_1}{\partial \epsilon^T} & \dfrac{\partial \Psi_1}{\partial \epsilon^B} \\ \dfrac{\partial \Psi_2}{\partial \epsilon^T} & \dfrac{\partial \Psi_2}{\partial \epsilon^B} \end{bmatrix}^i \tag{3.43}$$

where the partial derivatives are evaluated using the strains $\underset{\sim}{\epsilon}^i_{t+\Delta t}$ for iteration i .

The partial derivatives are computed as follows ;

$$\frac{\partial \Psi_1}{\partial \epsilon^T} = - \left\{ \sum_{j=1}^{N_c} \frac{\partial f^j}{\partial \epsilon^j} \frac{\partial \epsilon^j}{\partial \epsilon^T} + \frac{\partial F_s^T}{\partial \epsilon^T} \right\} \tag{3.44}$$

$$\frac{\partial \Psi_1}{\partial \epsilon^B} = - \left\{ \sum_{j=1}^{N_c} \frac{\partial f^j}{\partial \epsilon^j} \frac{\partial \epsilon^j}{\partial \epsilon^B} + \frac{\partial F_s^B}{\partial \epsilon^B} \right\} \tag{3.45}$$

$$\frac{\partial \Psi_2}{\partial \epsilon^T} = - \left\{ \sum_{j=1}^{N_c} \frac{\partial f^j}{\partial \epsilon^j} \frac{\partial \epsilon^j}{\partial \epsilon^B} \left[\frac{d^*}{2} - d^j \right] + \frac{\partial F_s^T}{\partial \epsilon^T} \left[\frac{d^*}{2} - d^T \right] \right\} \tag{3.46}$$

$$\frac{\partial \Psi_2}{\partial \epsilon^B} = - \left\{ \sum_{j=1}^{N_c} \frac{\partial f^j}{\partial \epsilon^j} \frac{\partial \epsilon^j}{\partial \epsilon^B} \left[\frac{d^*}{2} - d^j \right] + \frac{\partial F_s^T}{\partial \epsilon^B} \left[\frac{d^*}{2} - d^B \right] \right\} \quad . \qquad (3.47)$$

where $$\frac{\partial f^j}{\partial \epsilon^j} = A_c^j \frac{\partial \sigma^j}{\partial \epsilon^j} \quad ,$$

$$\frac{\partial \epsilon^j}{\partial \epsilon^T} = \frac{(d^j - d^B)}{h} \quad ,$$

$$\frac{\partial \epsilon^j}{\partial \epsilon^B} = \frac{(d^T - d^j)}{h} \quad ,$$

$$\frac{\partial F_s^T}{\partial \epsilon^T} = A_s^T \frac{\partial \sigma_s^T}{\partial \epsilon^T} \quad ,$$

$$\frac{\partial F_s^B}{\partial \epsilon^B} = A_s^B \frac{\partial \sigma_s^B}{\partial \epsilon^B} \quad ,$$

$\frac{\partial \sigma^j}{\partial \epsilon^j}$, $\frac{\partial \sigma_s^T}{\partial \epsilon^T}$, $\frac{\partial \sigma_s^B}{\partial \epsilon^B}$, are obtained from the corresponding constitutive relations.

The partial derivatives $\frac{\partial \epsilon^T}{\partial M^{int}}$, $\frac{\partial \epsilon^B}{\partial M^{int}}$ and $\frac{\partial \phi}{\partial M}$ are required later in section 3.7. These are obtained as follows :

the derivatives of Ψ_1 amd Ψ_2 with respect to M are, ($M = M^{int}$)

$$\frac{d\Psi_1}{dM} = 0 = \frac{\partial \Psi_1}{\partial M} + \frac{\partial \Psi_1}{\partial \epsilon^T} \frac{\partial \epsilon^T}{\partial M} + \frac{\partial \Psi_1}{\partial \epsilon^B} \frac{\partial \epsilon^B}{\partial M} \qquad (3.48)$$

$$\frac{d\Psi_2}{dM} = 0 = \frac{\partial \Psi_2}{\partial M} + \frac{\partial \Psi_2}{\partial \epsilon^T}\frac{\partial \epsilon^T}{\partial M} + \frac{\partial \Psi_2}{\partial \epsilon^B}\frac{\partial \epsilon^B}{\partial M} \qquad (3.49)$$

where $\frac{\partial \Psi_1}{\partial M} = 0$, $\frac{\partial \Psi_2}{\partial M} = -1$,

and $\frac{\partial \Psi_1}{\partial \epsilon^T}$, $\frac{\partial \Psi_1}{\partial \epsilon^B}$, $\frac{\partial \Psi_2}{\partial \epsilon^T}$, $\frac{\partial \Psi_2}{\partial \epsilon^B}$ are given by equations (3.44) - (3.47).

Equations (3.48) and (3.49) can be solved to give $\frac{\partial \epsilon^T}{\partial M}$ and $\frac{\partial \epsilon^B}{\partial M}$. $\frac{\partial \phi}{\partial M}$ is computed from the relation,

$$\frac{\partial \phi}{\partial M} = \frac{\partial \sigma}{\partial \epsilon^T}\frac{\partial \epsilon^T}{\partial M} + \frac{\partial \sigma}{\partial \epsilon^B}\frac{\partial \epsilon^B}{\partial M} \qquad (3.50)$$

where $\frac{\partial \phi}{\partial \epsilon^T} = -\frac{1}{h}$ and $\frac{\partial \phi}{\partial \epsilon^B} = \frac{1}{h}$.

Some insight into the moment-curvature response can be obtained by studying a simple model consisting of 2 concrete layers as shown in Figure 3.17. The

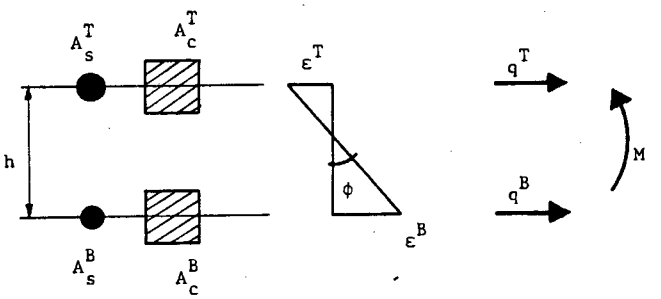

Figure 3.17 : Two-layer beam model

concrete layers are assumed to be at the same level as the steel layers, and there is no axial force at the section. For a given bending moment M , and assuming that the initial axial force is zero, equilibrium occurs when the

force at the bottom of the beam, q^B , is equal to the negative value of the force in the top of the beam, q^T . For a positive bending moment, q^B is simply the force in the bottom steel, (the concrete has no tensile strength). The relation between q^B and ϵ^B is given for monotonic loading in Figure 3.18(b). At the same time the relation between the force in the top of the beam, q^T and ϵ^B is shown in Figure 3.18(a) with $(-q^T)$ plotted in the

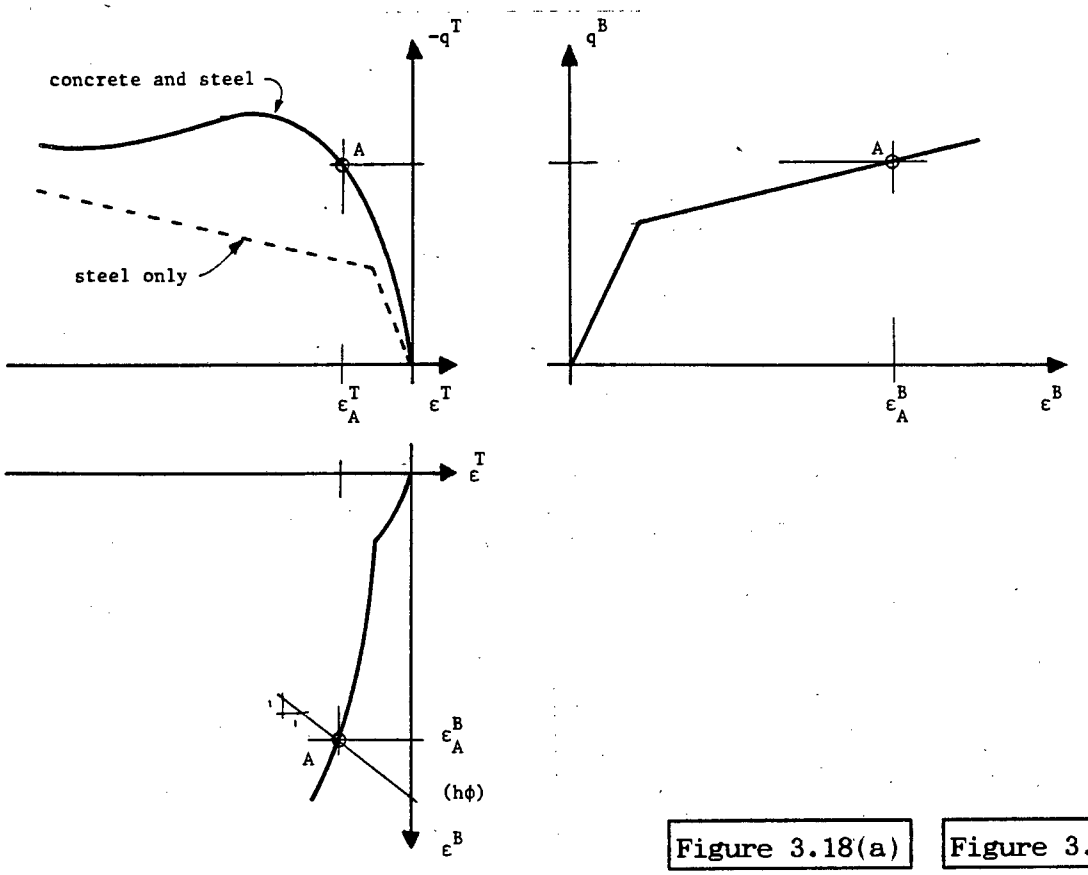

Figure 3.18(a) Figure 3.18(b)

Figure 3.18(c)

Figure 3.18 : Equilibrium path for two-layer beam model

same direction as q^B . The possible equilibrium positions are obtained by the intersection of these two curves with a horizontal line in Figures 3.18(a) and (b), i.e. where $q^B = -q^T$. Point A indicates such a position in Figures 3.18(a) and (b). The curve of equilibrium points is shown in strain space in Figure 3.18(c). A three dimensional illustration of the equilibrium curve is given in Figure 3.19. Such a representation was found

to be particularly useful when the Newton scheme had difficulty in converging.

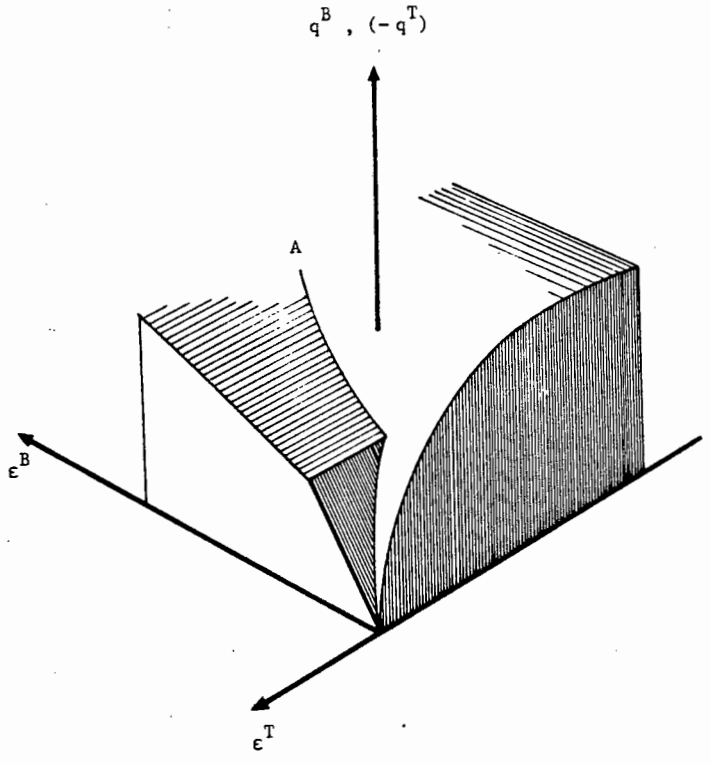

Figure 3.19 : Three-dimensional view of equilibrium path

The computer implementation of the Newton iteration scheme to obtain the moment-curvature response is discussed in Chapter 4, along with examples and some of the numerical difficulties encountered.

The Newton iteration scheme described above can also be used when the curvature is prescribed and the bending moment must be computed. In this case, the curvature-strain compatibility equation is used along with the axial force equilibrium equation as the two fundamental equations to be satisfied. They are

$$F^{int} = F^* \tag{3.51}$$

$$\epsilon^B - \epsilon^T = h\,\phi^* \tag{3.52}$$

where ϕ^* is the prescribed curvature.

These equations can be cast in a residual form similar to equation (3.41). The independent variables are also ϵ^T and ϵ^B and a Newton iteration scheme similar to the one given in Table 3.1 is used.

3.6 Bar-Slippage Model for Anchorage

Although a simple approximation to the bar slip-bond stress relationship may suffice for monotonic loading, it cannot model the mechanisms described in Chapter 2 which occur during cyclic loading. A simple one dimensional finite element model is thus chosen to model the steel-concrete interaction at the beam-column joints and to calculate the steel stress-slip relationship. Such a model has been used previously in simulating experimental specimens, see for example [36,54]. In the context of the layered beam model, the finite element model is required to have as few elements and integration points as possible in order to model the steel stress-slip relation sufficiently well.

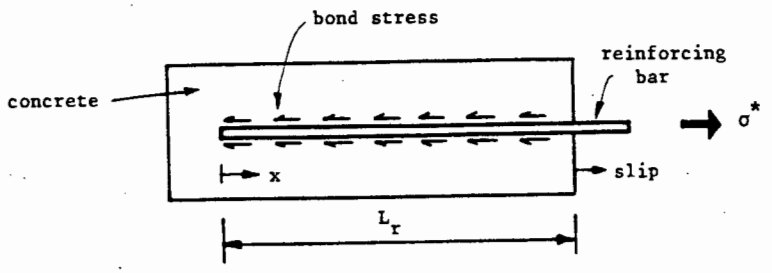

Figure 3.20 : Steel-concrete interaction model

In order to develop the equations governing the steel-concrete interaction, a section of reinforced concrete consisting of a single steel bar surrounded by concrete as depicted in Figure 3.20 is considered. The bar with a length L_r , is only loaded at the one end. The position of a point along the bar is defined by its coordinate along the x axis. The relative slip of the bar with respect to the concrete is represented by ω and is a function of position. The free body diagram of a small section of the bar, dx long, is shown in Figure 3.21. The bond stress q acts on the bar surface and σ is the axial stress in the steel.

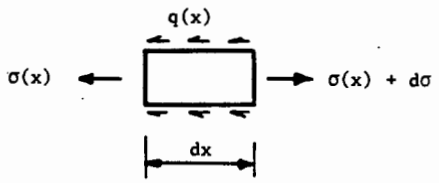

Figure 3.21 : Stresses acting on section of bar

Equilibrium of a small section of bar requires that,

$$\frac{d\sigma(x)}{dx} - \frac{\Psi_o}{A} q(x) = 0 \qquad (3.53)$$

or

$$\frac{d\sigma(x)}{dx} - p.q(x) = 0 \qquad (3.54)$$

with $p = \frac{\Psi_o}{A}$;

and where Ψ_o is the circumference of the bar

A is the cross sectional area of the bar

q(x) the bond stress, is a function of position

$\sigma(x)$ the steel stress, is a function of position.

The kinematic relationship is given by

$$\frac{d\omega}{dx} = \epsilon_s - \epsilon_c \tag{3.55}$$

where ϵ_s and ϵ_c are the steel and concrete strains respectively. Since we are concerned with large inelastic responses, it can be argued that the contribution of the concrete strains to the relative slip will be negligible and can thus be ignored. This simplifies the computations with equation (3.55) reducing to

$$\frac{d\omega}{dx} = \epsilon_s \quad . \tag{3.56}$$

The constitutive relation for the reinforcing bar can be described in the form of a function S as follows :

$$\sigma(x) = S(\epsilon_s(x)) \tag{3.57}$$

where $\epsilon_s(x)$ is the axial strain in the steel bar.

The constitutive relation for the bond stress-bond slip relationship can be described in the form of a function Q as follows :

$$q(x) = Q(\omega) \tag{3.58}$$

where ω is the relative bond slip.

The bar is positioned from $x = 0$ to $x = L_r$ as shown in Figure 3.22. In the finite element formulation that follows, the boundary conditions consist of a prescribed slip ω^* at $x = L_r$, and a stress of zero at $x = 0$.

A substitution of equations (3.54), (3.56), (3.57) and (3.58) leads to the following governing equation :

$$\frac{d}{dx}\left[S\left(\frac{d\omega}{dx}\right)\right] - p.Q(\omega) = 0 \qquad (3.59)$$

with

$$\left.\begin{aligned} S\left(\frac{d\omega}{dx}\right)\Big|_{x=0} &= 0 \\ \omega\Big|_{x=L_r} &= \bar{\omega} \end{aligned}\right\} \qquad (3.60)$$

In the finite element approximation, the domain Ω is discretized into disjoint element subdomains Ω^e , e = 1,2 ..., N_E where N_E is the total number of elements. Each element subdomain is defined by a set of ordered

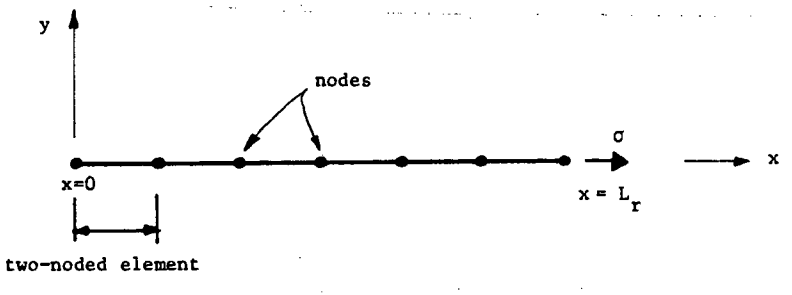

Figure 3.22 : Finite element model of bar

nodal points, i = 1,2, ..., N_p , where N_p is the total number of nodes defining the element. This discretization is illustrated in Figure 3.22. N_p is defined with a maximum value of 4 for the present studies. The various element types are depicted in Figure 3.23.

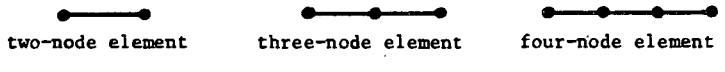

Figure 3.23 : Element definitions

The displacement field for an element is approximated by

$$\omega(x) = \sum_{i=1}^{N_p} N_i(x)\, d_i^e = \underset{\sim}{N}^T(x)\, \underset{\sim}{d}^e \qquad (3.61)$$

where N_p is the total number of nodes defining an element

d_i^e is the displacement of node i of the element e

and N_i are the shape functions which must satisfy the interpolation property and the conditions :

$$N_i(x) = \begin{cases} 1 \ , \ x = x_i \\ 0 \ , \ x = x_j \ , \ i \neq j \end{cases} .$$

From the approximation of the displacement field, the following relations can be stated :

$$\epsilon(x) = \frac{d\omega}{dx} = \sum_{i=1}^{N_c} B_i(x)\, d_i^e = \underset{\sim}{B}^T(x)\, \underset{\sim}{d}^e \qquad (3.62)$$

where $B_i = \dfrac{dN_i}{dx}$

$$\sigma(x) = S\left(\frac{d\omega}{dx}\right) = S\left[\sum_{i=1}^{N_p} B_i(x)\, d_i^e\right] = S(x, \underset{\sim}{d}^e) \qquad (3.63)$$

$$q(x) = Q\left[\sum_{i=1}^{N_p} N_i(x)\, d_i^e\right] = Q(x, \underset{\sim}{d}^e) \ . \qquad (3.64)$$

Vectors are defined to contain the nodal quantities for all the nodes in the finite element model. For example, the displacement vector $\underset{\sim}{d}$ is defined to contain displacements related to all nodal degrees of freedom.

The finite element matrix form of the problem reduces to a set of nonlinear equations, written as

$$\underset{\sim}{R}(\underset{\sim}{d}) = \underset{\sim}{F} \tag{3.65}$$

where the internal force vector $\underset{\sim}{R}(\underset{\sim}{d})$ is

$$\underset{\sim}{R}(\underset{\sim}{d}) = \mathop{\Lambda}_{e=1}^{N_E} \underset{\sim}{r}^e(\underset{\sim}{d}^e) \quad . \tag{3.66}$$

Λ is a finite element assembly operator which consists of a mapping of the local element degrees of freedom to global degrees of freedom and a summation of all element contributions in a global sense.

The element internal force vector is given by

$$\underset{\sim}{r}^e(\underset{\sim}{d}^e) = \{r_i^e(\underset{\sim}{d}^e)\} \tag{3.67}$$

with components

$$r_i^e(\underset{\sim}{d}^e) = \int_{\Omega^e} B_i(x)\, \sigma(x)\, d\Omega + \int_{\Omega^e} p\, N_i(x)\, q(x)\, d\Omega \quad . \tag{3.68}$$

The load vector $\underset{\sim}{F}$ contains zeros for all nodal degrees of freedom. The bar slip is prescribed to have a value $\bar{\omega}$ for the node at $x = L_r$.

1. Calculate $\underset{\sim}{\Psi}(\underset{\sim}{d}_t)^o = \underset{\sim}{R}(\underset{\sim}{d}_t) - \underset{\sim}{F}_{t+\Delta t}$

2. Set iteration counter i=0 , $\Delta \underset{\sim}{d}^o_{t+\Delta t} = 0$

3. Start of iteration loop i = i+1

4. Determine tangent operator $\mathscr{D}\ \underset{\sim}{\Psi}(\underset{\sim}{d}^i_{t+\Delta t})$

5. Solve $\mathscr{D}\ \underset{\sim}{\Psi}(\underset{\sim}{d}^i_{t+\Delta t})\ \Delta \underset{\sim}{d}^i = - \underset{\sim}{\Psi}(\underset{\sim}{d}^i_{t+\Delta t})$

6. Update $\Delta \underset{\sim}{d}^{i+1}_{t+\Delta t} = \Delta \underset{\sim}{d}^i_{t+\Delta t} + \Delta \underset{\sim}{d}^i$

   $\underset{\sim}{d}^{i+1}_{t+\Delta t} = \underset{\sim}{d}_t + \Delta \underset{\sim}{d}^{i+1}_{t+\Delta t}$

7. Calculate $\underset{\sim}{\Psi}(\underset{\sim}{d}^{i+1}_{t+\Delta t}) = \underset{\sim}{R}(\underset{\sim}{d}^{i+1}_{t+\Delta t}) - \underset{\sim}{F}_{t+\Delta t}$

8. Check for convergence

   Return to step 3 if solution has not converged

Table 3.2 : Newton-Raphson iteration procedure

Numerically it is expedient to solve equation (3.65) incrementally in time. Thus, we write equation (3.65) as

with element contributions

$$\mathcal{D}\, \underset{\sim}{r}^e(\underset{\sim}{d}^e) = \frac{\partial r_i^e(\underset{\sim}{d}^e)}{\partial d_j^e} \tag{3.74}$$

and components

$$\frac{\partial r_i^e(\underset{\sim}{d}^e)}{\partial d_j^e} = \int_{\Omega^e} B_i(x)\; k^T\; B_j(x)\; d\Omega + \int_{\Omega^e} p\; N_i(x)\; k_b^T\; N_j(x)\; d\Omega \tag{3.75}$$

where $$k^T = \frac{\partial \sigma(x)}{\partial \epsilon} \tag{3.76}$$

and $$k_b^T = \frac{\partial q(x)}{\partial \omega} \quad . \tag{3.77}$$

In the corrector phase of the Newton-Raphson iteration scheme, the computations for updating the stresses and calculating the internal force vector $\underset{\sim}{R}$, were performed using an equilibrated stress state at the end of the last converged time step. The incremental strains are then calculated using the incremental displacements $\Delta \underset{\sim}{d}_{t+\Delta t}^{i+1}$.

A finite element program was written to model the steel-concrete interaction problem. The program uses the Newton-Raphson iteration scheme described above and includes three types of elements : 2 noded, 3 noded and 4 noded, (linear, quadratic and cubic interpolation respectively). The numerical integrations were performed using Gaussian quadrature. The order of integration is controlled by the 2nd terms in equations (3.65) and (3.75) so that for example, the two noded element requires 2 Gauss points for full integration.

Examples illustrating the results obtained with the program, as well as details concerning the implementation into the layered beam element are given in Chapter 4.

3.7 Numerical Solution Procedures for Layered Beam Element

In this section the numerical procedures used to determine the internal forces and the stiffness matrix for the layered beam element are outlined.

In the context of determining the internal forces of the element, the internal force-displacement relations in equation (3.35) are essentially a compatibility requirement that must be satisfied, since the rotations θ_A and θ_B , as well as the vertical displacements v_A and v_B are known. In addition to these equations, equilibrium at the ends of the beam must be satisfied. This can be expressed as

$$- F_A^{int} = N_A \tag{3.78}$$

$$F_B^{int} = N_B \tag{3.79}$$

where N_A and N_B are the axial end forces as defined in Figure 3.10(b),

and, F_A^{int} and F_A^{int} are the forces calculated at the end sections once the strain distribution is known. The negative sign in equation (3.78) is required as a result of the sign convention used at sections, see Figure 3.15.

Equation (3.35) is written with the known values on the right hand side,

$$(H^*_{11}\,\theta'_a + H^*_{12}\,\theta'_b) + (\theta^s_A + \theta^s_B) + (G^*_{1k}\,\phi_k) = \theta_A + (v_A - v_B) \qquad (3.80)$$

$$(H^*_{21}\,\theta'_a + H^*_{22}\,\theta'_b) + (\theta^s_A + \theta^s_B) + (G^*_{2k}\,\phi_k) = \theta_B + (v_A - v_B) \qquad (3.81)$$

where $0 \le k \le n$ and $0 \le k \le m$.

Equations (3.78) - (3.81) can be written in the form

$$\underset{\sim}{F}^{int} = \underset{\sim}{F}^{ext} \qquad (3.82)$$

where $$\underset{\sim}{F}^{int} = \begin{Bmatrix} -F^{int}_A \\ F^{int}_B \\ (H^*_{11}\,\theta'_a + H^*_{12}\,\theta'_b) + (\theta^s_A + \theta^s_B) + (G^*_{1k}\,\phi_k) \\ (H^*_{21}\,\theta'_a + H^*_{22}\,\theta'_b) + (\theta^s_A + \theta^s_B) + (G^*_{2k}\,\phi_k) \end{Bmatrix}$$

and $$\underset{\sim}{F}^{ext} = \begin{Bmatrix} N_A \\ N_B \\ \theta_A + (v_A - v_B) \\ \theta_B + (v_A - v_B) \end{Bmatrix} .$$

In this study variations in the axial force during the response of the beam are not permitted. Consequently, N_A and N_B do not change during the response and are always known. Thus, when the internal forces of the beam are required to be determined at a time $t+\Delta t$, the vector $\underset{\sim}{F}^{ext}$ contains known quantities. Writing equation (3.82) in a residual form, a Newton iteration scheme can be employed to solve equation (3.82). The residual

form is given as

$$\underset{\sim}{\Psi} = \underset{\sim}{F}^{ext} - \underset{\sim}{F}^{int} \tag{3.83}$$

and equilibrium is achieved when $\underset{\sim}{\Psi}$ is within some prescribed tolerance.

Four independent variables $\bar{u}_i$ are chosen as follows :

(i) if bar slip is allowed at an end, then the bar slips ω^T amd ω^B are used as the independent variables (the superscripts refer to the top and bottom steel layers respectively)

(ii) if no bar slip is allowed at an end, then the strains at the steel layers ϵ^T amd ϵ^B are used as the independent variables.

In (i) above, the bar slips are used to avoid possible numerical problems which can occur if the steel stress is known and the bar slip needs to be determined; at large enough stress levels total pull out of the bar can occur. Thus, in a case where bar slip is allowed at both ends of the beam, the vector of independent variables is defined as

$$\underset{\sim}{\bar{u}} = [\omega_A^T , \omega_A^B , \omega_B^T , \omega_B^B]^T$$

where the subscripts refer to the ends A and B of the beam.

In another case, if bar slip is allowed at end A but not at end B, then

$$\underset{\sim}{\bar{u}} = [\omega_A^T , \omega_A^B , \epsilon_B^T , \epsilon_B^B]^T \quad .$$

The solution at a time step $t+\Delta t$ can be computed using the Newton iteration scheme in Table 3.3, if the converged solution at a previous time step t is known.

Given : (1) solution at a previous time step t : $\bar{\underset{\sim}{u}}_t$, $\underset{\sim}{F}^{int}_t$

(2) rotations θ_A , θ_B and displacements v_A and v_B for step $t+\Delta t$.

1. Set iteration counter i=0 , $\Delta\bar{\underset{\sim}{u}}^{i}_{t+\Delta t} = 0$

2. Calculate $\underset{\sim}{\psi}^{i} = \underset{\sim}{F}^{ext}_{t+\Delta t} - (\underset{\sim}{F}^{int})_t$

3. Start iteration loop i = i+1

4. Calculate $[J]^i$

5. Solve $[J]^i \Delta\underset{\sim}{u}^i = - \underset{\sim}{\psi}^i$

6. Update $\Delta\bar{\underset{\sim}{u}}^{i+1}_{t+\Delta t} = \Delta\bar{\underset{\sim}{u}}^{i}_{t+\Delta t} + \Delta\bar{\underset{\sim}{u}}^{i}$

$\bar{\underset{\sim}{u}}^{i+1}_{t+\Delta t} = \bar{\underset{\sim}{u}}_t + \Delta\bar{\underset{\sim}{u}}^{i+1}_{t+\Delta t}$

7. Determine $(\underset{\sim}{F}^{int})^{i+1}_{t+\Delta t}$

8. Calculate $\underset{\sim}{\psi}^{i+1} = \underset{\sim}{F}^{ext}_{t+\Delta t} - (\underset{\sim}{F}^{int})^{i+1}_{t+\Delta t}$

9. Check $\underset{\sim}{\psi}^{i+1}$ for convergence

Return to step 3 if the solution has not converged

Table 3.3 : Newton iteration scheme for internal force calculations

The Jacobian matrix $[J]^i$ is defined with components $J_{\ell s}$ as

$$J_{\ell s} = \frac{\partial \Psi_\ell}{\partial u_s} \quad , \qquad \ell \text{ and } s = 1,2,3,4 \quad . \tag{3.84}$$

The partial derivatives in equation (3.84) with independent variables of strain are :

$$\text{(i)} \quad \frac{\partial \Psi_\ell}{\partial \epsilon^r_p} = - \left\{ \sum_{j=1}^{N_c} \frac{\partial f^j}{\partial \epsilon^j} \frac{\partial \epsilon^j}{\partial \epsilon^r_p} + \frac{\partial F^r_p}{\partial \epsilon^r_p} \right\} \qquad \begin{array}{l} \text{for : } \ell = 1,2 \\ \qquad\; p = A,B \\ \qquad\; r = T,B \end{array} \tag{3.85}$$

and also if : (a) $\ell = 1$, $p = A$ then $\dfrac{\partial \Psi_1}{\partial \epsilon^r_B} = 0$

(b) $\ell = 2$, $p = B$ then $\dfrac{\partial \Psi_2}{\partial \epsilon^r_A} = 0$

$$\text{(ii)} \quad \frac{\partial \Psi_\ell}{\partial \epsilon^r_p} = - \left\{ H^*_{g1} \frac{\partial \theta'_a}{\partial \epsilon^r_p} + H^*_{g2} \frac{\partial \theta'_b}{\partial \epsilon^r_p} + G^*_{gk} \frac{\partial \Phi_k}{\partial \epsilon^r_p} \right\} \qquad \begin{array}{l} \text{for : } \ell = 3,4 \\ \qquad\; p = A,B \\ \qquad\; r = T,B \\ \qquad\; g = \ell - 2 \\ 0 \leq k \leq n \\ 0 \leq k \leq m \end{array}$$

(3.86)

where :

$$\frac{\partial \theta'_a}{\partial \epsilon^r_p} = \frac{\partial \theta'_a}{\partial M_a} \frac{\partial M_a}{\partial M_p} \frac{\partial M_p}{\partial \epsilon^r_p} + \frac{\partial \theta'_a}{\partial M_b} \frac{\partial M_b}{\partial M_p} \frac{\partial M_p}{\partial \epsilon^r_p}$$

$$\frac{\partial \theta'_b}{\partial \epsilon^r_p} = \frac{\partial \theta'_b}{\partial M_a} \frac{\partial M_a}{\partial M_p} \frac{\partial M_p}{\partial \epsilon^r_p} + \frac{\partial \theta'_b}{\partial M_b} \frac{\partial M_b}{\partial M_p} \frac{\partial M_p}{\partial \epsilon^r_p}$$

$$\frac{\partial M_p}{\partial \epsilon_p^r} = \left[\sum_{j=1}^{N_c} \frac{\partial f^j}{\partial \epsilon^j} \frac{\partial \epsilon^j}{\partial \epsilon_p^r} \left[\frac{d^*}{2} - d_p^j\right]\right] + \frac{\partial F_p^r}{\partial \epsilon_p^r} \left[\frac{d^*}{2} - d_p^r\right]$$

$$\frac{\partial M_a}{\partial M_A} = \left[1 - \frac{x_a}{L}\right] \quad , \quad \frac{\partial M_a}{\partial M_B} = -1 - \frac{x_a}{L}$$

$$\frac{\partial M_b}{\partial M_A} = -\frac{x_b}{L} \quad , \quad \frac{\partial M_b}{\partial M_B} = \left[1 - \frac{x_b}{L}\right]$$

$$\frac{\partial \phi_k}{\partial \epsilon_p^r} = \frac{\partial \phi_k}{\partial M_k} \frac{\partial M_k}{\partial M_p} \frac{\partial M_p}{\partial \epsilon_p^r}$$

$$\frac{\partial M_k}{\partial M_A} = \left[\frac{x}{L} - 1\right]$$

$$\frac{\partial M_k}{\partial M_B} = \frac{x}{L} \quad , \quad \text{where x is the coordinate of the integration station k}$$

$\frac{\partial \theta'_a}{\partial M_a}$, $\frac{\partial \theta'_a}{\partial M_b}$, $\frac{\partial \theta'_b}{\partial M_a}$ and $\frac{\partial \theta'_b}{\partial M_b}$ are obtained from equations (3.18) and (3.19)

$\frac{\partial \phi_k}{\partial M_k}$ is given in equation (3.50) .

The following contributions in equations (3.85) and (3.86) are obtained at the ends of the beam,

$$\sum_{j=1}^{N_c} \frac{\partial f^j}{\partial \epsilon^j} \frac{\partial \epsilon^j}{\partial \epsilon_p^r} \; ; \; \frac{\partial F_p^r}{\partial \epsilon_p^r} \; ; \; \sum_{j=1}^{N_c} \frac{\partial f^j}{\partial \epsilon^j} \frac{\partial \epsilon^j}{\partial \epsilon_p^r} \left[\frac{d^*}{2} - d^j\right]$$

and $\frac{\partial \phi_p}{\partial M_p}$.

The partial derivatives in equation (3.84) with independent variables of bar slip are :

(i) $$\frac{\partial \Psi_\ell}{\partial \omega_p^r} = \frac{\partial \Psi_\ell}{\partial \epsilon_p^r} \frac{\partial \epsilon_p^r}{\partial \omega_p^r} \qquad \text{for : } \ell = 1,2;\ p = A,B;\ r = T,B \qquad (3.87a)$$

where $\frac{\partial \Psi_\ell}{\partial \epsilon_p^r}$ is defined in equation (3.85)

and $$\frac{\partial \epsilon_p^r}{\partial \omega_p^r} = \frac{\partial \epsilon_p^r}{\partial F_p^r} \frac{\partial F_p^r}{\partial \omega_p^r} \quad .$$

(ii) $$\frac{\partial \Psi_\ell}{\partial \omega_p^r} = \frac{\partial \Psi_\ell}{\partial \epsilon_p^r} \frac{\partial \epsilon_p^r}{\partial \omega_p^r} - \frac{\partial \theta_p^s}{\partial \omega_p^r} \qquad \text{for } \ell = 3,4;\ p = A,B;\ r = T,B \qquad (3.87b)$$

where $\frac{\partial \Psi_\ell}{\partial \epsilon_p^r}$ is defined in equation (3.86)

$\frac{\partial F_p^r}{\partial \omega_p^r}$ is obtained from the finite element model for bar slip

$\frac{\partial \theta_p^s}{\partial \omega_p^r}$ is obtained from equations (3.1) .

The procedure to calculate $\underset{\sim}{F}^{int}$ in Table 3.3, including the internal forces M_A and M_B is given in Table 3.4.

Given : ϵ_p^r or ω_p^r $\qquad$ $r = T,B$; $p = A,B$

1. Calculate θ_p^s : $\theta_p^s = \dfrac{\alpha_p^T - \alpha_p^B}{h_p}$

(equation (3.1))

2. Determine F_p^r : $F_p^r = A_p^r \sigma_p^r$

(i) given ϵ_p^r : σ_p^r can be determined from the steel constitutive relation

(ii) given ω_p^r : Determine σ_p^r using the finite element model for bar slip. Hence, determine ϵ_p^r using steel constitutive relation

3. Calculate M_p, F_p

Use equations (3.38) and (3.39), taking into account the conditions relating to the crack opening criteria

4. Determine ϕ_k

Calculate $M_k = \left[\dfrac{x_b}{L} - 1\right] M_A + \left[\dfrac{x}{L}\right] M_B$, and determine ϕ_k using moment-curvature relationship

5. Calculate $\underset{\sim}{F}^{int}$

Use equations (3.80) and (3.81)

Table 3.4 : Procedure to determine $\underset{\sim}{F}^{int}$, and the end moments M_A and M_B

Once the end moments M_A and M_B have been determined, the end shear forces can be calculated from the following relationship :

$$\begin{Bmatrix} P_A \\ P_B \end{Bmatrix} = \frac{1}{L} \begin{bmatrix} 1 & 1 \\ -1 & -1 \end{bmatrix} \begin{Bmatrix} M_A \\ M_B \end{Bmatrix} \quad . \tag{3.88}$$

The element internal force vector is defined as

$$\underset{\sim}{R}_e^{int} = [F_A^{int} \ , \ P_A \ , \ M_A \ , \ F_B^{int} \ , \ P_B \ , \ M_B]^T \tag{3.89}$$

In the following discussion, the layered beam element stiffness matrix is derived for the shear and bending terms only. The element displacement vector is defined as $[v_A, \ \theta_A, \ v_B, \ \theta_B]^T$, and the element internal force vector as $[P_A, \ M_A, \ P_B, \ M_B]^T$. The element stiffness matrix $[k]_e$ for element e , is then defined as

$$[k]_e = \begin{bmatrix} \frac{\partial P_A}{\partial v_A} & \frac{\partial P_A}{\partial \theta_A} & \frac{\partial P_A}{\partial v_B} & \frac{\partial P_A}{\partial \theta_B} \\ \frac{\partial M_A}{\partial v_A} & \frac{\partial M_A}{\partial \theta_A} & \frac{\partial M_A}{\partial v_B} & \frac{\partial M_A}{\partial \theta_B} \\ \frac{\partial P_B}{\partial v_A} & \frac{\partial P_B}{\partial \theta_A} & \frac{\partial P_B}{\partial v_B} & \frac{\partial P_B}{\partial \theta_B} \\ \frac{\partial M_B}{\partial v_A} & \frac{\partial M_B}{\partial \theta_A} & \frac{\partial M_B}{\partial v_B} & \frac{\partial M_B}{\partial \theta_B} \end{bmatrix} \tag{3.90}$$

The element stiffness matrix is defined in a general sense : at any time during the response it can be considered the tangent stiffness operator.

Taking the derivatives of the third and fourth components in equation (3.83), (Ψ_3 and Ψ_4) with respect to θ_A, θ_B, v_A and v_B gives,

$$\frac{\partial \Psi_3}{d\theta_A} = 0 = \frac{\partial \Psi_3}{\partial \theta_A} + \frac{\partial \Psi_3}{\partial M_A}\frac{\partial M_A}{\partial \theta_A} + \frac{\partial \Psi_3}{\partial M_B}\frac{\partial M_B}{\partial \theta_A} \tag{3.91}$$

$$\frac{\partial \Psi_4}{d\theta_A} = 0 = \frac{\partial \Psi_4}{\partial \theta_A} + \frac{\partial \Psi_4}{\partial M_A}\frac{\partial M_A}{\partial \theta_A} + \frac{\partial \Psi_4}{\partial M_B}\frac{\partial M_B}{\partial \theta_A} \tag{3.92}$$

$$\frac{\partial \Psi_3}{d\theta_B} = 0 = \frac{\partial \Psi_3}{\partial \theta_B} + \frac{\partial \Psi_3}{\partial M_B}\frac{\partial M_A}{\partial \theta_B} + \frac{\partial \Psi_3}{\partial M_B}\frac{\partial M_B}{\partial \theta_B} \tag{3.93}$$

$$\frac{\partial \Psi_4}{d\theta_B} = 0 = \frac{\partial \Psi_4}{\partial \theta_B} + \frac{\partial \Psi_4}{\partial M_A}\frac{\partial M_A}{\partial \theta_B} + \frac{\partial \Psi_4}{\partial M_B}\frac{\partial M_B}{\partial \theta_B} \tag{3.94}$$

$$\frac{\partial \Psi_3}{dv_A} = 0 = \frac{\partial \Psi_3}{\partial v_A} + \frac{\partial \Psi_3}{\partial M_A}\frac{\partial M_A}{\partial v_A} + \frac{\partial \Psi_3}{\partial M_B}\frac{\partial M_B}{\partial v_A} \tag{3.95}$$

$$\frac{\partial \Psi_4}{dv_A} = 0 = \frac{\partial \Psi_4}{\partial v_A} + \frac{\partial \Psi_4}{\partial M_A}\frac{\partial M_A}{\partial v_A} + \frac{\partial \Psi_4}{\partial M_B}\frac{\partial M_B}{\partial v_A} \tag{3.96}$$

$$\frac{\partial \Psi_3}{dv_B} = 0 = \frac{\partial \Psi_3}{\partial v_B} + \frac{\partial \Psi_3}{\partial M_A}\frac{\partial M_A}{\partial v_B} + \frac{\partial \Psi_3}{\partial M_B}\frac{\partial M_B}{\partial v_B} \tag{3.97}$$

$$\frac{\partial \Psi_4}{dv_B} = 0 = \frac{\partial \Psi_4}{\partial v_B} + \frac{\partial \Psi_4}{\partial M_A}\frac{\partial M_A}{\partial v_B} + \frac{\partial \Psi_4}{\partial M_B}\frac{\partial M_B}{\partial v_B} \tag{3.98}$$

where : $\dfrac{\partial \Psi_3}{\partial \theta_A} = \dfrac{\partial \Psi_4}{\partial \theta_B} = \dfrac{\partial \Psi_3}{\partial v_A} = \dfrac{\partial \Psi_4}{\partial v_A} = 1$

$$\frac{\partial \Psi_3}{\partial \theta_B} = \frac{\partial \Psi_4}{\partial \theta_A} = 0$$

$$\frac{\partial \Psi_3}{\partial v_B} = \frac{\partial \Psi_4}{\partial v_A} = -1 \quad .$$

Also,

$$\frac{\partial \Psi_\ell}{\partial M_p} = -\left\{\left[H^*_{g1}\frac{\partial \theta'_a}{\partial M_p} + H^*_{g2}\frac{\partial \theta'_b}{\partial M_p}\right] + \frac{\partial \theta^s_p}{\partial M_p} + G^*_{gk}\frac{\partial \theta_k}{\partial M_p}\right\} \qquad (3.99)$$

for $\ell = 3,4$
$p = A,B$
$g = \ell - 2$
$0 \le k \le n$, $0 \le k \le m$

where :

$$\frac{\partial \theta'_a}{\partial M_p} = \frac{\partial \theta'_a}{\partial M_a}\frac{\partial M_a}{\partial M_p} + \frac{\partial \theta'_a}{\partial M_b}\frac{\partial M_b}{\partial M_p}$$

$$\frac{\partial \theta'_b}{\partial M_p} = \frac{\partial \theta'_b}{\partial M_a}\frac{\partial M_a}{\partial M_p} + \frac{\partial \theta'_b}{\partial M_b}\frac{\partial M_b}{\partial M_p}$$

$$\frac{\partial \theta^s_p}{\partial M_p} = \frac{\partial \theta^s_p}{\partial \omega^T_p}\frac{\partial \omega^T_p}{\partial \epsilon^T_p}\frac{\partial \epsilon^T_p}{\partial M_p} + \frac{\partial \theta^s_p}{\partial \omega^B_p}\frac{\partial \omega^B_p}{\partial \epsilon^B_p}\frac{\partial \epsilon^B_p}{\partial M_p}$$

$$\frac{\partial \omega^r_p}{\partial \epsilon^r_p} = \frac{\partial \omega^r_p}{\partial F^r_p}\frac{\partial F^r_p}{\partial \epsilon^r_p}$$

$$\frac{\partial \phi_k}{\partial M_p} = \frac{\partial \phi_k}{\partial M_k}\frac{\partial M_k}{\partial M_p}$$

$\frac{\partial \omega^r_p}{\partial F^r_p}$ is obtained from the bar slip finite element model

$\frac{\partial F^r_p}{\partial \epsilon^r_p}$, $\frac{\partial \epsilon^r_p}{\partial M_p}$ and $\frac{\partial \phi_p}{\partial M_p}$ are obtained from the moment-curature relation for the end of the beam

$\frac{\partial \phi_k}{\partial M_k}$ is obtained from the moment-curvature relationship for integration station k .

From equations (3.91) and (3.92), $\frac{\partial M_A}{\partial \theta_A}$ and $\frac{\partial M_B}{\partial \theta_A}$ can be determined. Likewise, equations (3.93) and (3.94) give $\frac{\partial M_A}{\partial \theta_B}$ and $\frac{\partial M_B}{\partial \theta_B}$; equations (3.95) and (3.96) give $\frac{\partial M_A}{\partial v_A}$ and $\frac{\partial M_B}{\partial v_A}$; and equations (3.97) and (3.98) give $\frac{\partial M_A}{\partial v_B}$ and $\frac{\partial M_B}{\partial v_B}$. The remaining terms in $[k]_e$ can be determined from the following relations;

$$\frac{\partial P_A}{\partial v_A} = \frac{1}{L}\left[\frac{\partial M_A}{\partial v_A} + \frac{\partial M_B}{\partial v_A}\right] \tag{3.100}$$

$$\frac{\partial P_A}{\partial \theta_A} = \frac{1}{L}\left[\frac{\partial M_A}{\partial \theta_A} + \frac{\partial M_B}{\partial \theta_A}\right] \tag{3.101}$$

$$\frac{\partial P_A}{\partial v_B} = \frac{1}{L}\left[\frac{\partial M_A}{\partial v_B} + \frac{\partial M_B}{\partial v_B}\right] \tag{3.102}$$

$$\frac{\partial P_A}{\partial \theta_B} = \frac{1}{L}\left[\frac{\partial M_A}{\partial \theta_B} + \frac{\partial M_B}{\partial \theta_B}\right] \tag{3.103}$$

$$\frac{\partial P_B}{\partial v_A} = -\frac{\partial P_A}{\partial v_A} \tag{3.104}$$

$$\frac{\partial P_B}{\partial \theta_A} = -\frac{\partial P_A}{\partial \theta_A} \tag{3.105}$$

$$\frac{\partial P_B}{\partial v_B} = -\frac{\partial P_A}{\partial v_B} \tag{3.106}$$

$$\frac{\partial P_B}{\partial \theta_B} = -\frac{\partial P_A}{\partial \theta_B} \quad . \tag{3.107}$$

Details concerning the implementation of the layered beam element into a finite element computer program are given in Chapter 4.

CHAPTER 4

COMPUTATIONAL IMPLEMENTATION AND SOLUTION STRATEGIES

The proposed layered beam element model was implemented into a nonlinear frame analysis program. An outline of the program is included in this chapter along with a discussion of the solution strategies employed in the aspects of the layered beam model. The nonlinear aspects contained in the constitutive models as well as the crack opening and closing criterion, present computational problems when attempting to converge onto a solution. The solution strategies form an important component in the exercise of developing a program which is robust and practical to use. Two aspects of the layered beam model - the moment-curvature response and the bar-slippage model were studied individually, prior to their implementation as part of the proposed layered beam model. These studies involved developing separate computer programs along with the necessary solution strategies. These two programs are also discussed in this chapter. Figure 4.1 illustrates how the various aspects concerning the layered beam model are related in the frame analysis program.

4.1 Computer Program for Frame Analyses

A computer program was developed for the nonlinear static analysis of plane frames on a UNIVAC 1100-81 computer. Various two-noded beam elements are included in the program, including the proposed layered beam element. A data management system developed by Vos [73] was used for the extensive data manipulation required by the program. The frame analysis program includes

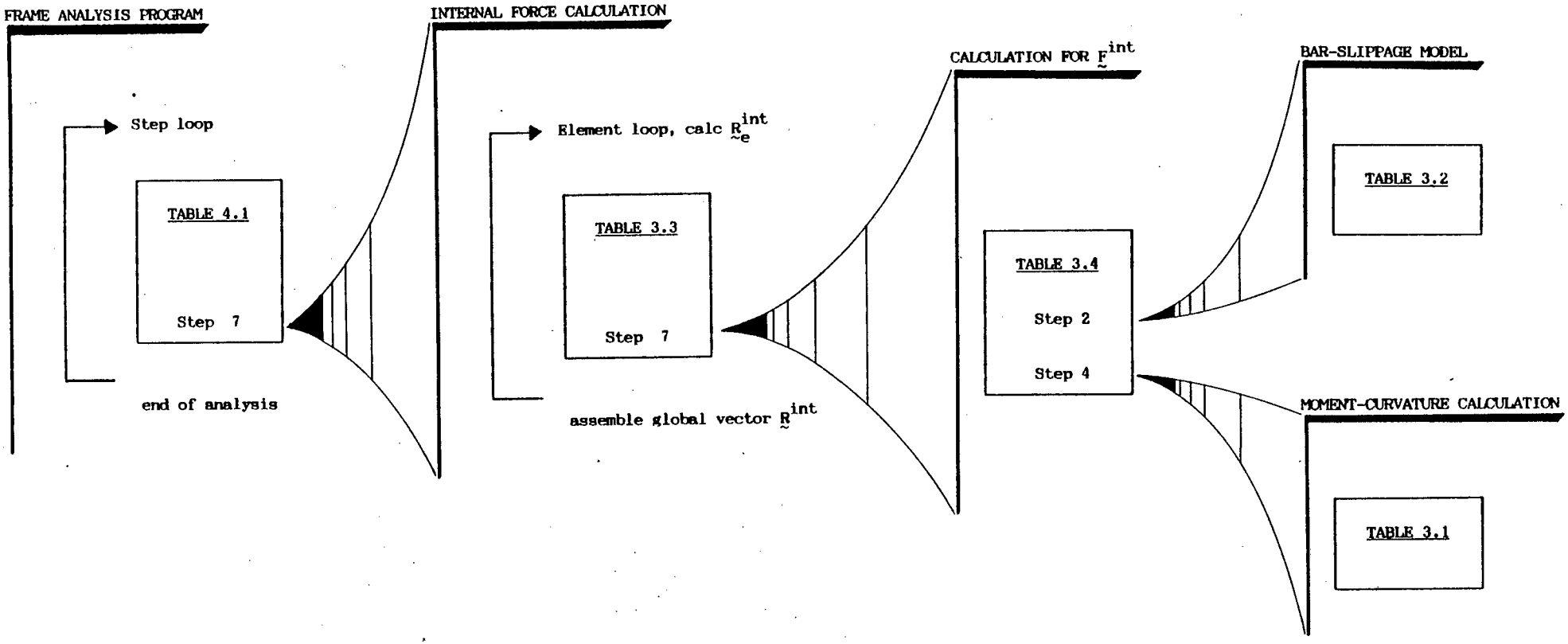

Figure 4.1 : Important aspects of computer implementation for layered beam model

standard boundary conditions and applied loads, as well as prescribed displacements. The program has out of core solvers for both symmetric and non-symmetric matrices.

In a static analysis, the problem reduces to a set of nonlinear equilibrium equations that need to be satisfied. They are written as

$$\underset{\sim}{R}^{int} = \underset{\sim}{R}^{ext} \tag{4.1}$$

where $\underset{\sim}{R}^{int}$ is the global vector of internal forces corresponding to the unknown displacement degrees of freedom,

and $\underset{\sim}{R}^{ext}$ is the global vector of external loads corresponding to the unknown displacement degrees of freedom.

The global internal force vector is assembled from the element internal force vectors, $\underset{\sim e}{R}^{int}$, defined in equation (3.89). The global displacement vector is defined by $\underset{\sim}{u}$. Assuming that the solution to equation (4.1) is known at time t , an iterative solution scheme is required to solve equation (4.1) at time t+Δt . This is achieved by first casting equation (4.1) in a residual form :

$$\underset{\sim}{r} = \underset{\sim}{R}^{ext} - \underset{\sim}{R}^{int} \tag{4.2}$$

where $\underset{\sim}{r}$ is the residual force vector.

A Newton-Raphson iterative scheme is used to determine the solution at time t+Δt . The numerical procedure is given in Table 4.1. Convergence is achieved when all the residuals in $\underset{\sim}{r}$ are within a specified tolerance.

1. Calculate $\underset{\sim}{r}^0 = (\underset{\sim}{R}^{ext})_{t+\Delta t} - (\underset{\sim}{R}^{int})_t$
2. Set iteration loop counter i=0 , $\Delta \underset{\sim}{u}^0_{t+\Delta t}$
3. Start iteration loop, i=i+1
4. Calculate $[K_T]$
5. Solve $[K_T]\ \Delta \underset{\sim}{u}^i = \underset{\sim}{r}^i$
6. Update $\Delta \underset{\sim}{u}^{i+1}_{t+\Delta t} = \Delta \underset{\sim}{u}^i_{t+\Delta t} + \Delta \underset{\sim}{u}^i$

   $\underset{\sim}{u}_{t+\Delta t} = \underset{\sim}{u}_t + \Delta \underset{\sim}{u}^{i+1}_{t+\Delta t}$
7. Determine $(\underset{\sim}{R}^{int})^{i+1}_{t+\Delta t}$
8. Calculate $\underset{\sim}{r}^{i+1} = (\underset{\sim}{R}^{ext})_{t+\Delta t} - (\underset{\sim}{R}^{int})^{i+1}_{t+\Delta t}$
9. Check $\underset{\sim}{r}^{i+1}$ for convergence

   Return to step 3 if solution has not converged

Table 4.1 : Newton-Raphson scheme to obtain equilibrium at time t+Δt

The tangent stiffness matrix $[K_T]$ is assembled from the element stiffness matrices given in equation (3.90). For the layered beam element the tangent stiffness matrix is nonsymmetric. For the calculation of $(\underset{\sim}{R}^{int})_{t+\Delta t}$, the solution is always incremented from the converged solution at time t . Details of these calculations are given in section 3.7. The check for convergence in step 9 of Table 4.1 consists of checking the maximum residual against a specified tolerance. A further check is made to ensure that the maximum residual does not get larger than a specified value. If this occurs, or if convergence is not obtained within a certain number of iterations, then the increment is restarted with a smaller step size. Figure 4.2 illustrates the various strategies adopted when convergence difficulties are encountered. 'No convergence likely' in Figure 4.2 refers to such an event. When convergence has been obtained, the step size for the

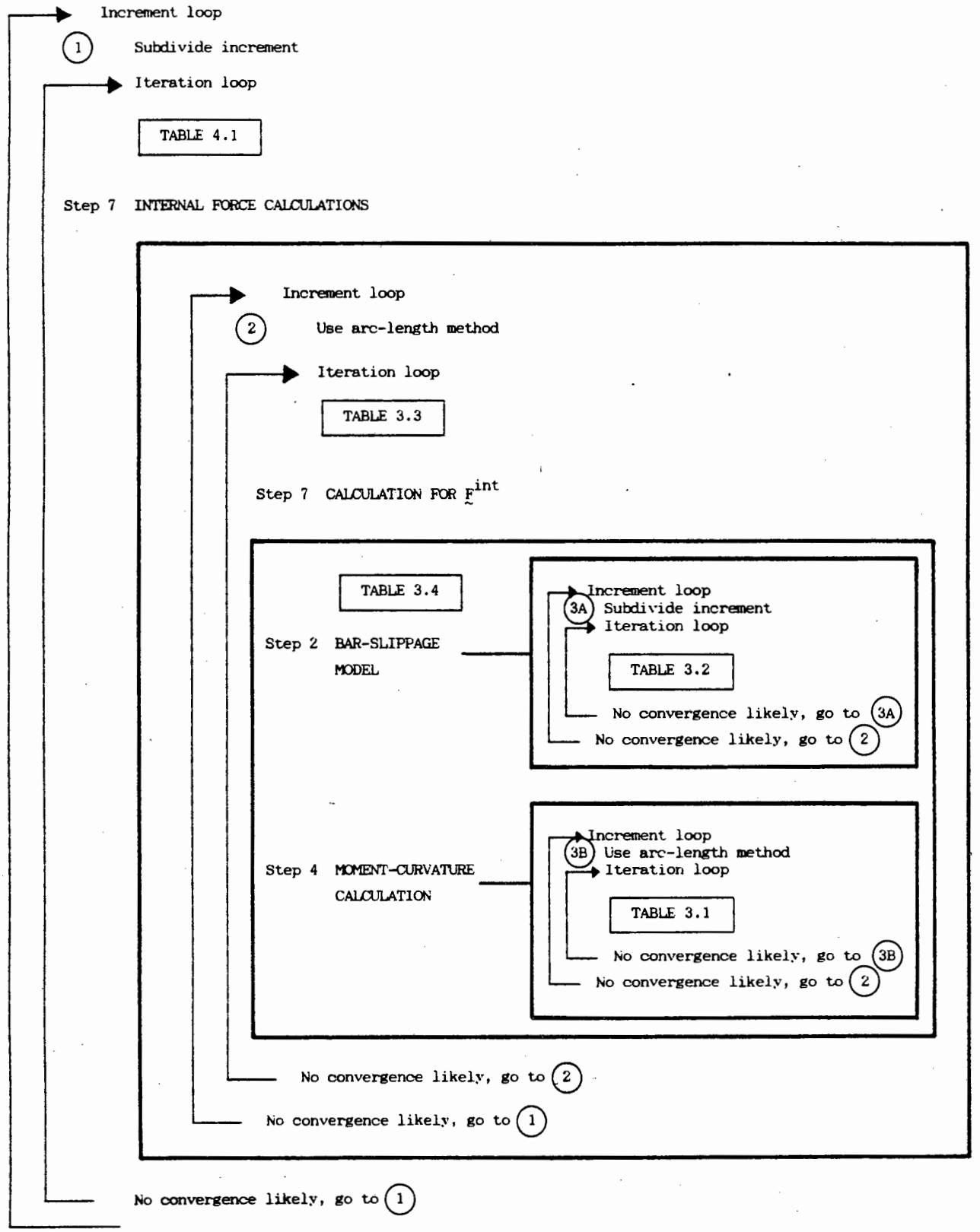

Figure 4.2 : Solution strategies when convergence difficulties are encountered

following increment is adjusted according to the number of iterations used to converge in the previous increment. Thus, when the solution has difficulty in converging, smaller step sizes are automatically used. The step sizes are increased when the solution converges easily.

The element internal force calculations for the proposed layered beam element are calculated using the Newton iteration scheme given in Table 3.3. This procedure was implemented as part of the element calculations in the frame analysis program as shown in Figure 4.1. In this iteration scheme the convergence check consists of checking the maximum residual against some prescribed tolerance. A check is also made to ensure that the maximum residual does not become too large as this can usually result in convergence problems in the moment-curvature response calculations and the bar-slippage finite element model. The maximum change in the end moments during an increment is restricted to prevent possible convergence problems in the moment-curvature response calculations.

The strategies used for various stages of the internal force calculations are summarized in Figure 4.2. When convergence problems are encountered, either the increment size in the internal force calculations is reduced or the arc-length method can be used, (2) in Figure 4.2. The arc-length method was preferred as it generally resulted in a converged solution for the internal force calculations. If a converged solution within a reasonable number of attempts is not obtained, the step size for the increment in the frame analysis program is reduced and the main increment loop restarted, (1) in Figure 4.2.

When convergence problems are encountered in the bar-slippage finite element model after the increment has been subdivided ((3A) in Figure 4.2), then the

element internal force increment loop is restarted using the arc-length method, (2) in Figure 4.2. Similarly, when the moment-curvature response does not converge after the arc-length method has been used ((3B) in Figure 4.2), then the element internal force increment loop is restarted using the arc-length method, (2) in Figure 4.2.

Studies showed that by using relatively small convergence tolerances, the results converged with relatively large increments. The maximum number of iterations allowed was taken as 7 since most of the converged solutions were obtained within 5 iterations. This helped to reduce the computational time.

4.2 Moment-Curvature Relationship

A computer program was developed to calculate the moment-curvature relationship. The same computer code was used as part of the proposed layered beam model. For the moment-curvature program, either the moment or the curvature can be prescribed. (Note that for the layered beam model the moment is prescribed.) Each layer of concrete or steel can have its own constitutive model. This means that the confined and unconfined concrete can be modelled with different constitutive relations.

The program uses the Newton scheme given in Table 3.1 to calculate the moment-curvature response. Convergence is achieved once the maximum residual is less than a specified value. As in the frame analysis program, a check is made to ensure that the residuals do not become too large. If this occurs, or if the solution has not converged within the allowable number of iterations, two options are available. The first is to subdivide the step size and restart the increment. This strategy was not successful at limit points of the moment-curvature response. In such cases Crisfield's

arc-length method [76] was used to obtain the solution. This is the second option available. A general form of the arc-length method as used in the solution procedure is given in Appendix B.

The arc-length method was used in situations where convergence problems were encountered, since in most cases it converged to a solution. In the cases where the convergence tolerance was not small enough, the arc-length method failed to converge due to the large residual loads present.

The moment-curvature response for a section consisting of two concrete layers and two steel layers is shown in Figure 4.3. In this case the concrete is prescribed to have some tensile strength. When the bottom layer

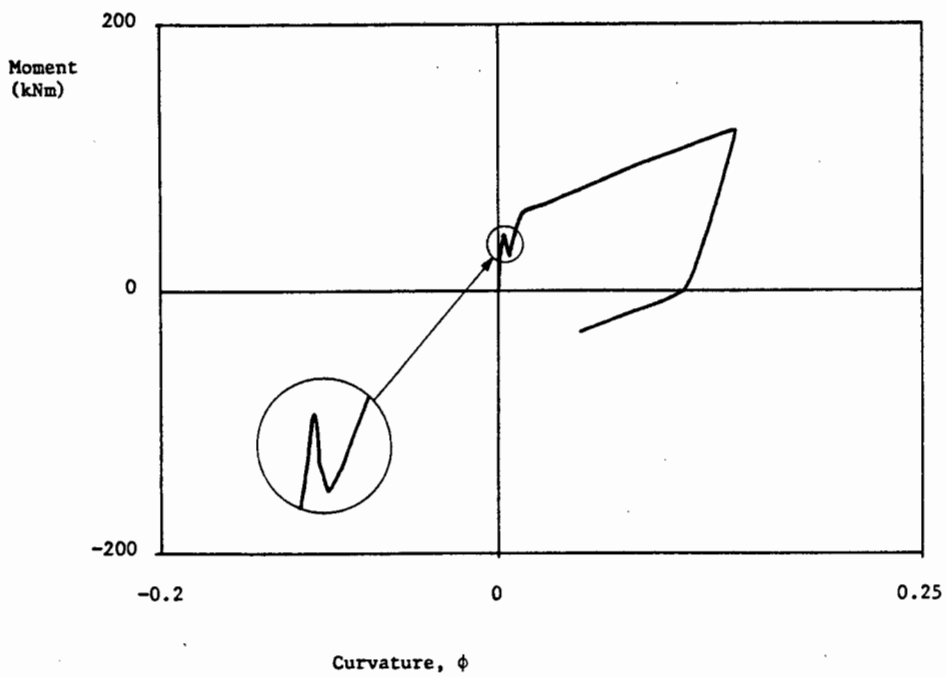

Figure 4.3 : Moment-curvature response using arc-length method; concrete cracks in tension

of concrete cracks in tension, a limit point in the moment-curvature response is reached. As the curvature increases, the moment first decreases before increasing again. The limit point and subsequent moment-curvature

response was obtained using the arc-length method. Although this is a situation which was generally not encountered, (in all subsequent examples the tensile strength was ignored) it serves to illustrate the capabilities of the arc-length method.

A situation more generally encountered occurred when the concrete reached its maximum compressive stress. In a section consisting of two concrete layers, this resulted in a limit point as illustrated in Figure 4.4. In sections consisting of more concrete layers, the limit points were more localized.

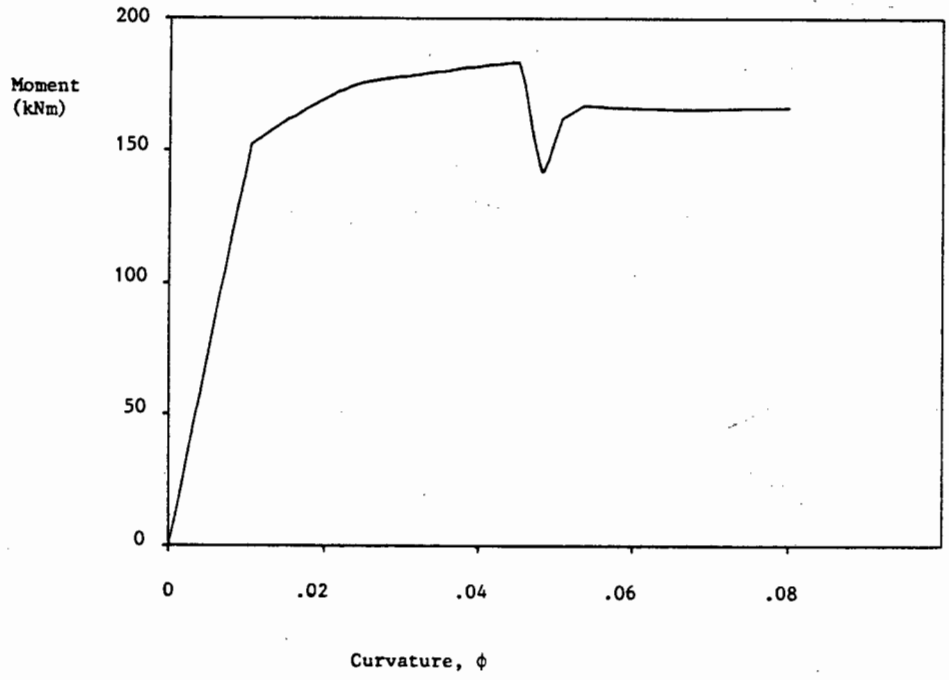

Figure 4.4 : Moment-curvature response using arc-length method; concrete softens in compression

Unloading during the moment-curvature response also provided convergence problems. Since the unloading situation can be recognised at the beginning of an increment, it is expedient to rather calculate the Jacobian in step 4 of Table 3.1 using the unloading stiffness moduli of all the relevant constitutive models. The unloading stiffnesses are predominantly elastic and by using such a scheme, the solution generally converged in one iteration.

4.3 Bar-Slippage Finite Element Model

A computer program was developed for the one dimensional bar-slippage finite element model described in section 3.6. For the context in which the model is used in the proposed layered beam model, the slip is prescribed and the corresponding steel stress is calculated using the finite element model. The computer program assumes that all the elements are of equal length and that all integration points have the same bond stress-slip constitutive model. The Newton-Raphson iteration procedure given in Table 3.2 is used in the computer program. In the convergence check, the maximum residual is checked against some prescribed tolerance. When the solution failed to converge, the step size was reduced and the increment restarted. The only situations in which this did not eventually result in convergence, were those in which the prescribed tolerance was too large.

Unloading could be identified at the start of an increment and the tangent operator in step 4 of Table 3.2 was then calculated using the element stiffness matrices with the material constitutive relations unloading. In such situations, the solution generally converged in one iteration for the increment.

CHAPTER 5

EVALUATION OF MULTI-LAYERED BEAM MODEL

In general the performance of an analytical model is evaluated by investigating the quality and consistency of the results predicted by the model. In this study this is achieved by a parametric study involving a cantilever beam, and a comparison of predicted and experimental results for a variety of cantilevers. A further aspect which needs to be considered in the evaluation of a model, is the ease with which the results can be interpreted and applied in the design process. In the context of the proposed layered beam model, this is achieved with suitable measures of damage.

This chapter starts by reviewing damage measures and proposing new ones. This is followed by an evaluation of the numerical results obtained from the moment-curvature program and the bar-slippage finite element model. The numerical results obtained using the multi-layered beam model for a parametric study are discusssed next. The purpose of the study is to show that the model presents consistent results and to determine the influence of particular variables in the modelling process. The chapter concludes with a comparison of the results predicted by the proposed layered beam model and the experimental results for some cantilever beams.

The results for the layered beam model presented in this chapter, use 50 layers to model the concrete, hence the reference to a multi-layered beam model. A simplified model in which only two concrete layers are used is evaluated in the following chapter.

5.1 Damage Measures

One of the most common measures of damage for reinforced concrete beams subjected to cyclic loading is the ductility factor. Ductility can be measured in various forms, for example rotational ductility μ_θ , curvature ductility μ_ϕ and displacement ductility μ . Rotational ductility is defined as the ratio of the maximum rotation recorded to the yield rotation, as shown in Figure 5.1. One of the problems associated with ductility measures

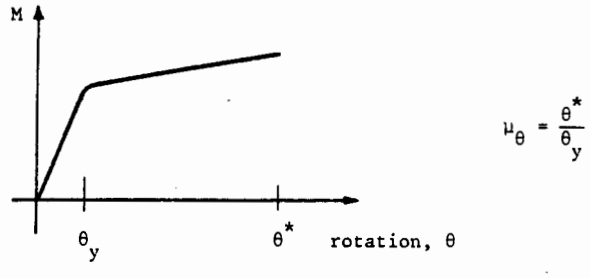

Figure 5.1 : Rotational ductility

occurs when the yield point is not clearly defined as illustrated in Figure 5.2(a). Another shortcoming of ductility is that it cannot reflect the amount of stiffness degradation which occurs during cyclic responses as shown in Figure 5.2(b). This has encouraged researchers to develop other measures of damage.

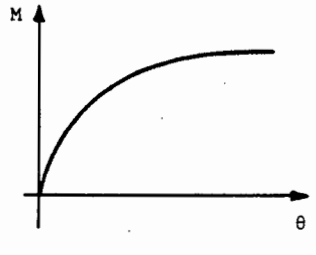

Figure 5.2(a)

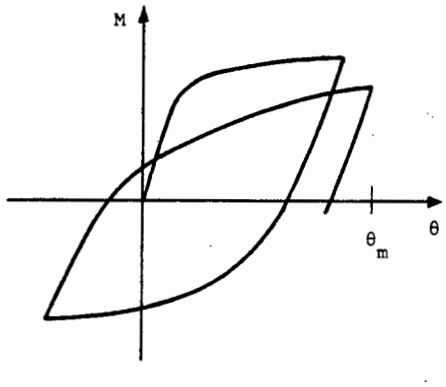

Figure 5.2(b)

Figure 5.2 : Problems associated with ductility factors

Banon *et al* [7] proposed a stochastic model of damage based on two damage measures; a flexural damage ratio and the dissipated energy. The flexural damage ratio (FDR) is defined as the ratio of the initial flexural stiffness of a member to its reduced secant stiffness at maximum displacement. Only displacements attributed to flexure are used for this damage measure. The reduced secant stiffness is thus defined using the end moment-flexural rotation relationship as illustrated in Figure 5.3. The flexural damage ratio clearly accounts for any stiffness degradation. The dissipated energy

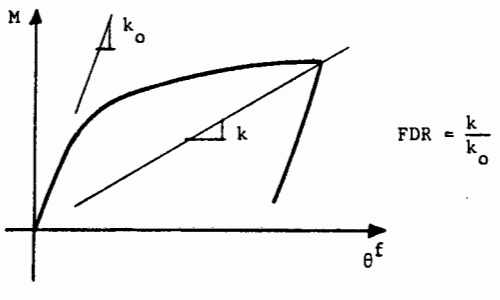

Figure 5.3 : Flexural damage ratio

is used to account for the damage effects resulting from cumulative inelastic deformation in reinforced concrete. The dissipated energy is computed by integrating the area under the moment-rotation curve at the end of a member. This energy is then normalized with respect to the maximum elastic flexural strain energy for a member subjected to antisymmetric bending. The normalized dissipated energy (E_n) is defined as follows :

$$E_n = \frac{E^*}{E_o} \qquad (5.1)$$

where E^* is the dissipated energy given by

$$E^* = \int_{time} M(\theta)\, d\theta \quad ,$$

and E_o is the maximum elastic flexural strain energy defined as

$$E_o = \frac{M_y^2 L}{12 EI}$$

where M_y is the yield moment,

L is the length of the member in antisymmetric bending.

For this definition, the point of contraflexure is assumed to occur at the centre of the beam.

Roufaiel and Meyer [74] have proposed a modified flexural damage ratio (MFDR) defined as follows :

$$MFDR = \max[MFDR^+ , MFDR^-] \qquad (5.2)$$

where

$$MFDR^{\pm} = \frac{\left[\frac{\phi_x}{M_x}\right]^{\pm} - \left[\frac{\phi_y}{M_y}\right]^{\pm}}{\left[\frac{\phi_m}{M_m}\right]^{\pm} - \left[\frac{\phi_y}{M_y}\right]^{\pm}} .$$

The + and - superscripts refer to positive and negative bending,

ϕ_y and M_y are the curvature at yield and moment at yield respectively,

ϕ_m and M_m are the curvature and moment at the onset of failure,

ϕ_x and M_x are the curvature and moment at the point in the response under consideration.

These quantities are illustrated in Figure 5.4.

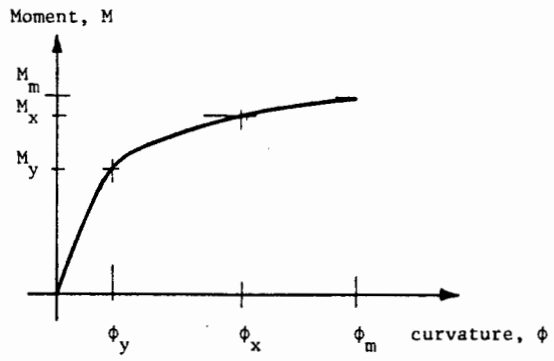

Figure 5.4 : Damage measure MFDR

The onset of failure is defined by the curvature at which the concrete strain in the extreme fibre reaches a critical value ϵ_{cr}, given empirically in [74] as

$$\epsilon_{cr} = (2 + 600\ \rho'')\ \epsilon_m \qquad (5.3)$$

where ρ'' is the volume of hoop steel as defined in section 2.3,

and ϵ_m is the strain at which the concrete stress is at a maximum.

When MFDR = 0 , the section is in an undamaged state, whereas for MFDR = 1 the member has failed.

In this thesis, a damage measure is proposed for a member which incorporates aspects of damage that can lead to failure in the response of members dominated by flexure. In the damage measures used in the following definitions, Λ is zero in the undamaged state and equal to 1 in the totally damaged or failure state.

A flexural damage measure Λ_f is defined by rewriting the FDR in the form,

$$\Lambda_f = \frac{k_o - k}{k_o} \tag{5.4}$$

where k_o and k are as defined for the FDR.

For this damage measure, failure will usually occur before $\Lambda_f = 1$. However, it does give an indication of how much flexural damage has occurred.

An anchorage damage measure Λ_a, is defined to indicate how close the anchored reinforcing bar is to pullout. It is defined as

$$\Lambda_a = \left[\frac{k_o - k}{k_o - k^*}\right]\left(\frac{k^*}{k}\right) \tag{5.5}$$

where k_o and k^* are the initial and failure stiffness defined in Figure 5.5,

and k is the stiffness for the point at which the maximum slip has occurred.

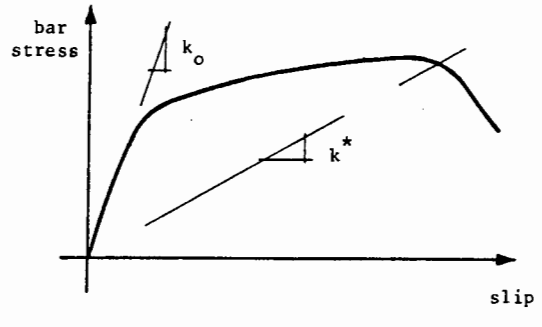

Figure 5.5 : Anchorage damage measure

A monotonic loading analysis is required to determine the slip at which pullout of the anchored bar will occur and the corresponding stiffness k^*. Pullout can of course occur at a smaller slip after some cyclic loading. A study showed that in these cases the critical stiffness k^* was still a good approximation for defining pullout.

Generally, reinforced concrete members dominated by flexure fail when the reinforcing bars lose their concrete cover and tend to buckle. A damage measure for the concrete Λ_c is defined with the objective of indicating how close the reinforced concrete member is to this type of failure. When $\Lambda_c = 1$, cover to the reinforcing bars has been lost and the bars are on the point of buckling. Apart from the observation that significant cracking of the concrete occurs prior to spalling, little information is available on the state of the concrete when this happens. Roufaiel and Meyer [74] suggest that the onset of failure can be characterised by the concrete strain in the extreme fibre as given by equation (5.3). It would seem that a damage measure based on the concept of comparing an average strain quantity in the concrete with a critical value could be feasible. Obviously it would be very difficult, if not impossible, to try and determine such a critical strain measure with a great deal of accuracy. Also, using strain measures directly would result in a damage measure with a large amount of variation. However, if the damage measure is based on the damage variable used in the concrete constitutive model, then far less variation in the results is obtained. The reason is that the damage variable used in the concrete constitutive relation does not change much at larger strain measures. The concrete damage measure is defined as

$$\Lambda_c = \frac{\lambda_{avg}}{\lambda_{cr}} \quad . \tag{5.6}$$

In this definition, λ_{avg} is the average value of the concrete damage variables in a specified number of concrete layers. Typically these would be the layers nearest the reinforcing steel and in the confined region. The critical damage variable, λ_{cr} , is the damage variable corresponding to the critical strain measure.

It should be recognised that Λ_c is defined for beams dominated by flexural characteristics only. A more complete definition of Λ_c should include a dependence on the shear stresses present. These stresses are critical in controlling the action of crushing and spalling of the concrete at the crack interface.

An overall damage measure Λ_D is defined as

$$\Lambda_D = \max[\Lambda_a, \Lambda_c] \tag{5.7}$$

where Λ_a and Λ_c are defined as the maximum respective values at an end of a beam member.

The proposed damage measures Λ_f, Λ_a, Λ_c and Λ_D are used to evaluate the analytical model along with the previously defined measures FDR, E_n and MFDR.

5.2 Moment-Curvature Relationship

An investigation to determine the optimum number of concrete layers to be used in the layered model, was conducted for a typical reinforced concrete section using the computer program developed to determine the

moment-curvature response. The concrete layers were defined in three regions; the unconfined top and bottom regions and the confined central region. The unconfined concrete was modelled using a different constitutive relation to the confined concrete as discussed in Chapter 2. The areas of the concrete layers in the central region were calculated using only the confined concrete area and not the unconfined concrete on the sides.

The moment-curvature responses for models where the number of concrete layers was varied, are presented in Figure 5.6. The study showed that sections modelled with 70, 50 and 25 concrete layers gave almost identical results. The sections modelled with 12, 6 and 4 layers did not give good results. They also presented some numerical difficulties, especially evident in the 4 layer model. The response of the 4 layer model is worth discussing further since it clearly displays the numerical difficulties sometimes experienced for the cyclic response of models with more concrete layers.

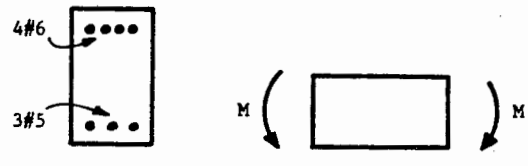

Figure 5.6(a) : Beam cross-section and loading

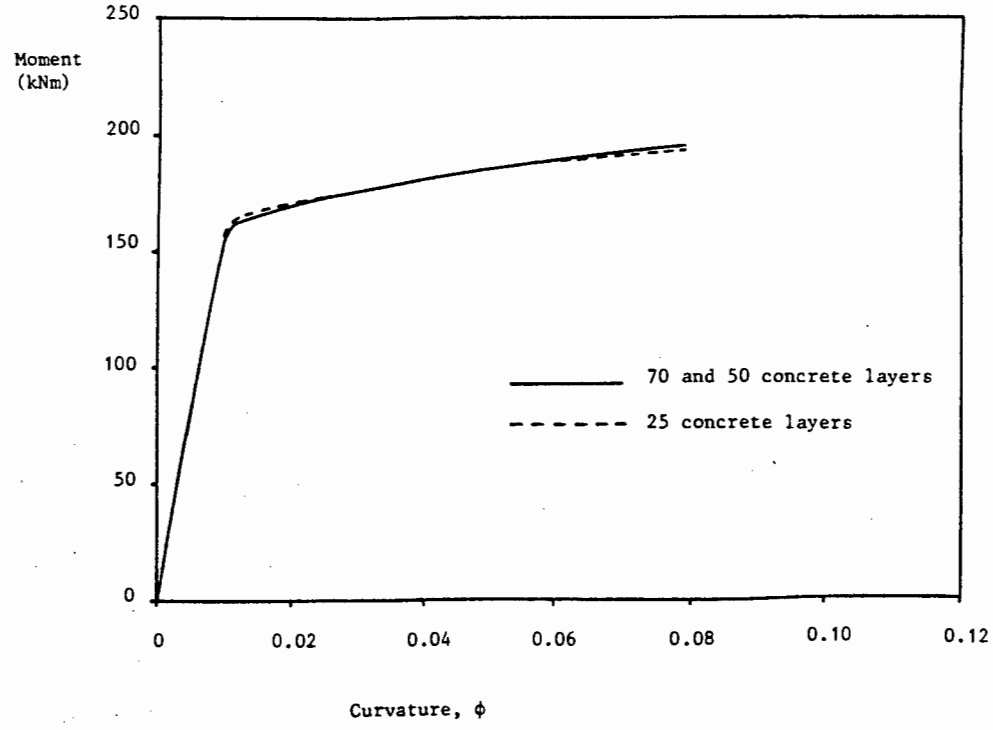

Figure 5.6(b)

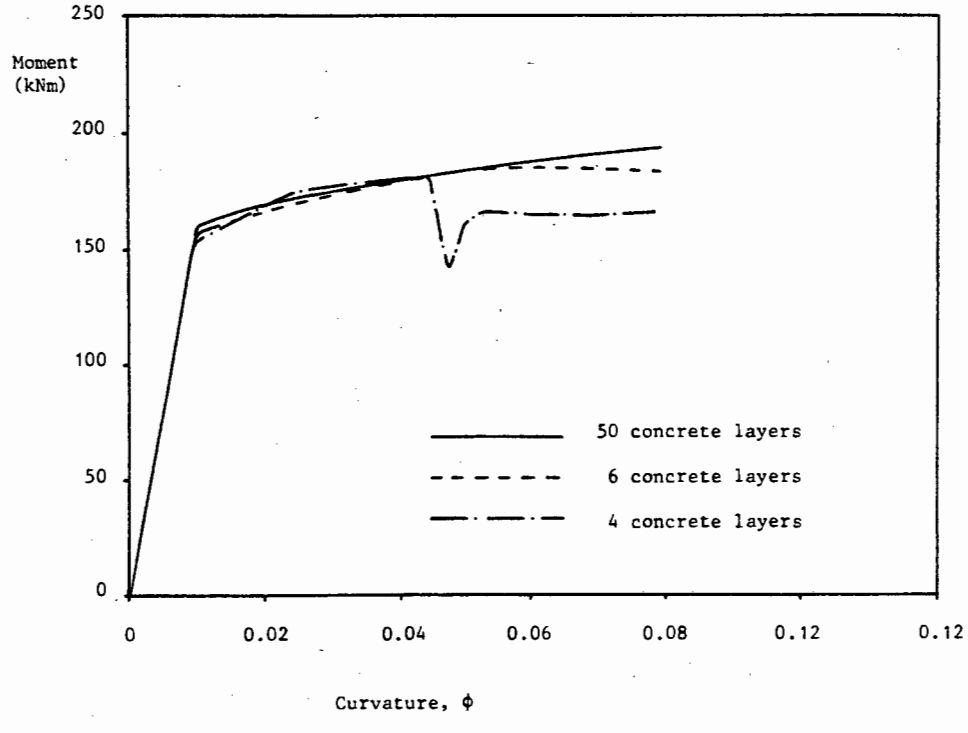

Figure 5.6(c)

Figure 5.6 : Moment-curvature response with a varying number of concrete layers

For the 4 layer model, the total force acting in the top section of the beam q_T , is plotted against the strain of the top steel layer in Figure 5.7(b). Alongside this, Figure 5.7(a) shows the total force in the bottom section (- q_B) plotted against the strain in the bottom steel. The corresponding relationship in strain space is shown in Figure 5.7(c). The moment-curvature response is defined as the intersection of two surfaces in a 3-dimensional space defined with the top and bottom strains as the two horizontal axes, and the forces q_T and (- q_B) measured along the vertical axis. The intersection of these two surfaces is illustrated in Figure 5.8.

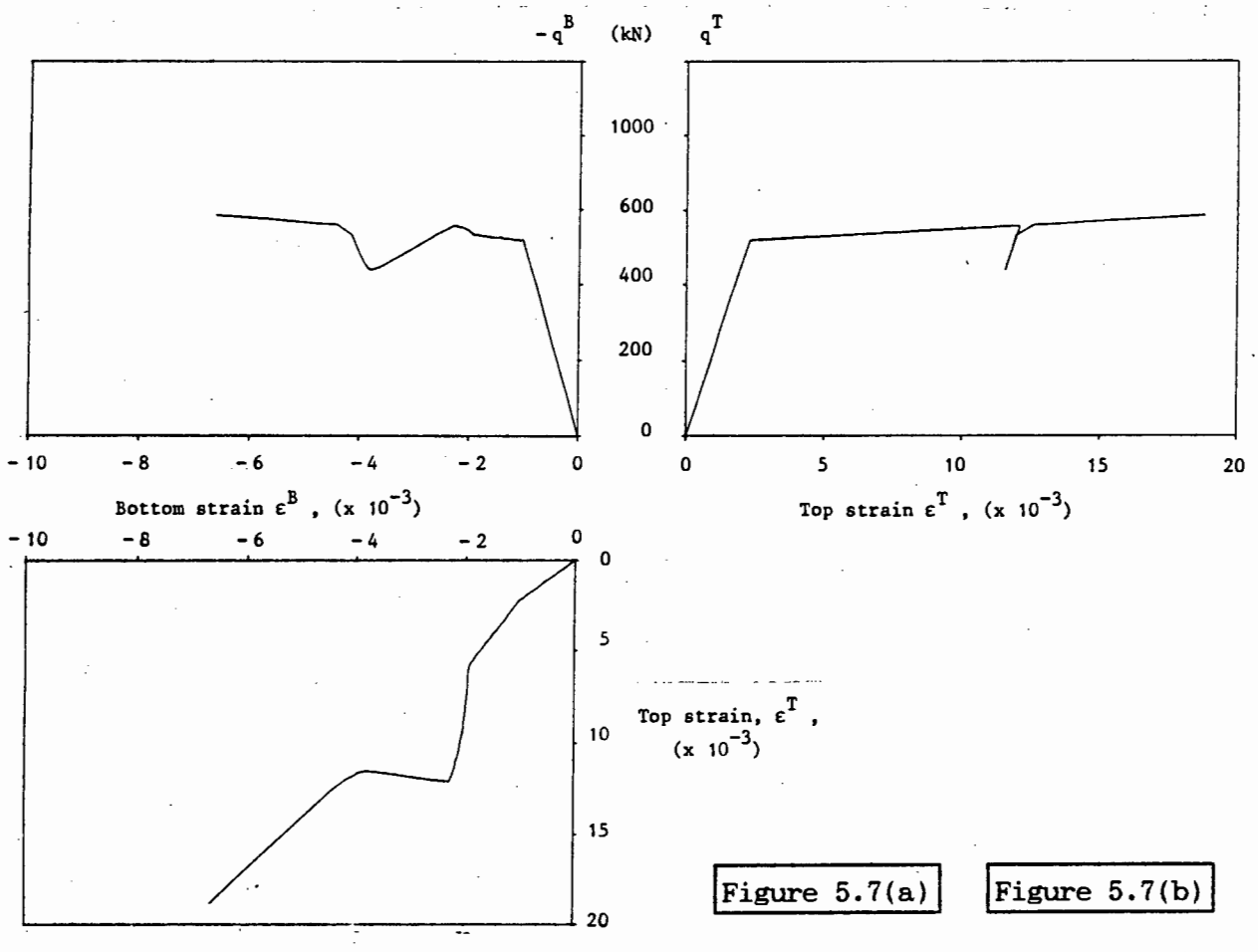

Figure 5.7 : Four-layered model

The limit point occurs when the concrete layer closest to the bottom of the beam reaches its maximum compressive stress. At this point the top steel starts to unload elastically. The response after the limit point in Figure 5.8 clearly explains why the top steel unloads, reloads and yields again.

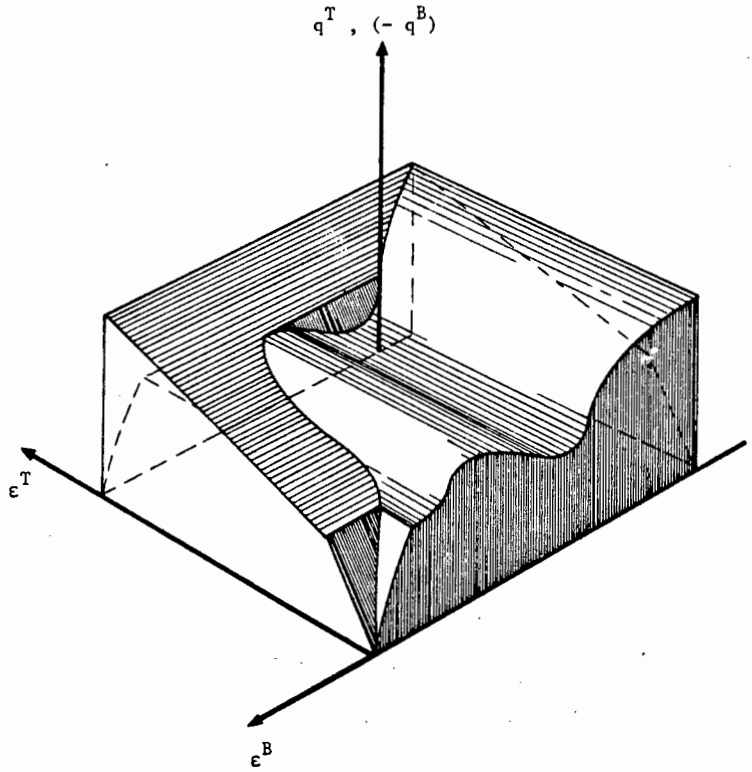

Figure 5.8 : Three-dimensional representation of equilibrium curve

As a result of this study, it was decided to use a model consisting of 50 concrete layers for the evaluation of the multi-layered beam model. The rationale is that 50 layers provides a satisfactory compromise between the computation time required for the material calculations with a larger number of layers, and the additional computation time required for limit points. In addition it provides a comparable basis for further studies in which a 2 layered model is used. This is discussed further in Chapter 6.

A typical cyclic moment-curvature response for a section modelled with 50 concrete layers is shown in Figure 5.9. The aspects of bar slippage and crack development are not included in the calculation of the moment-curvature response, but are accounted for in the layered beam model. These

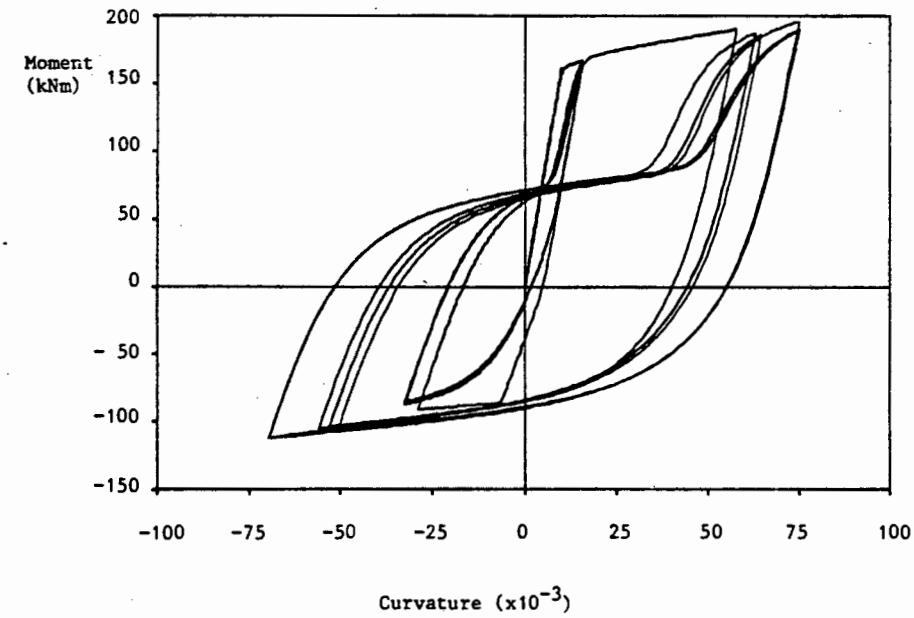

Figure 5.9 : Typical cyclic response

aspects, as discussed in Chapter 3, explain the sharp change in stiffness which occurs as the moment increases.

5.3 Bar-Slippage Finite Element Model

Numerical tests were conducted in order to determine a computationally efficient finite element model. The constraints for using the bar-slippage finite element model as part of the layered beam model was to keep the number of integration points as low as possible. There are two reasons for this. Firstly, to reduce the computational time, and secondly to keep the

computer storage requirements to a minimum. Results reported by Mercer and Martin [17] show that a few higher order elements can be used to achieve this.

The results reported here concern the cyclic response of a 25mm diameter bar with an anchorage length of 625mm. The experimental results are reported in [56]. A sketch of the anchored bar and the bond stress-bond slip constitutive model is shown in Figure 5.10(a). In the finite element model,

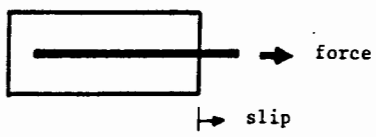

Figure 5.10(a) : Bar-slippage problem

all the integration points have identical constitutive relations. The results for 1, 2 and 8 four-noded elements are shown in Figures 5.10(b) - (d) respectively. The experimental results are indicated by a dashed line.

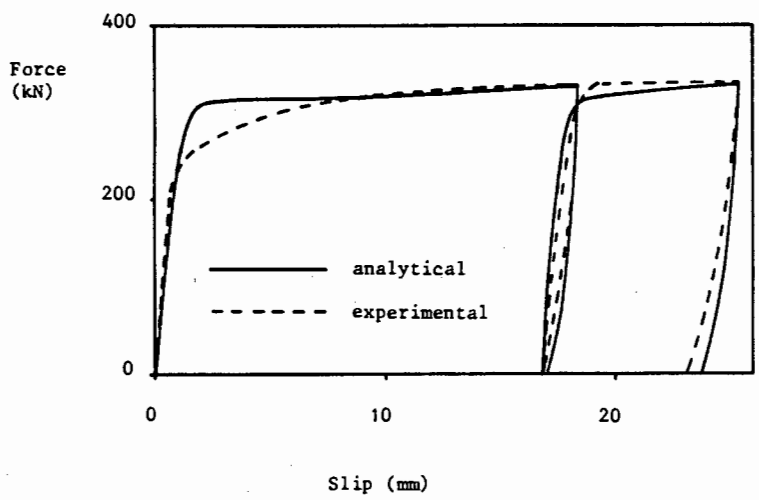

Figure 5.10(b) : Results for 1 four-noded element

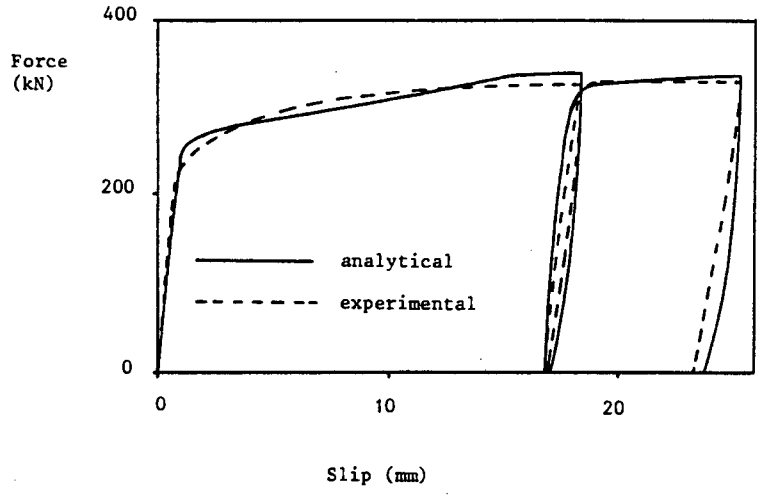

Figure 5.10(c) : Results for 2 four-noded elements

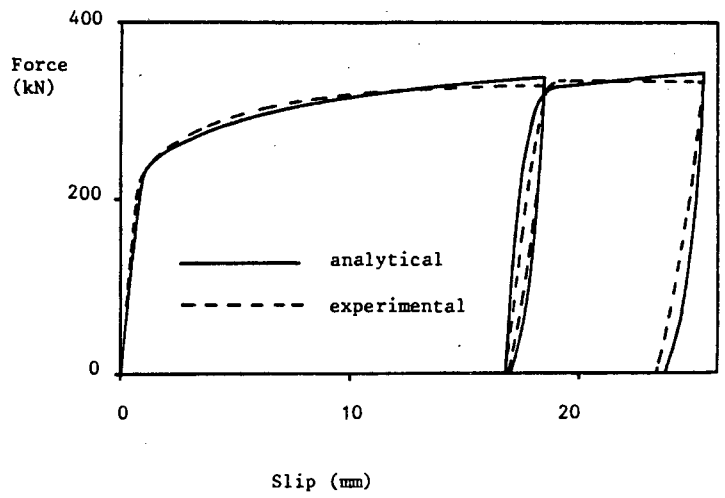

Figure 5.10(d) : Results for 8 four-noded elements

The results for a single element are notably different from the experimental results immediately after yielding has occurred. The results for 2 elements compare favourably with the experimental results, while the model consisting of 8 elements shows results which correspond closely with the experimental results.

Based on these results and those reported in [17], it was decided to use 2 four-noded elements to model the bar-slippage response. Incorporated in this decision are a number of assumptions which need to be discussed. The first concerns the variation in the bond stress-bond slip characteristics along a bar anchored in an exterior beam-column joint. The bars are usually bent with hooks as depicted in Figure 5.11. Eligehausen *et al* [75] conducted experimental studies on the cyclic response of hooked bars. Briefly they concluded that the cyclic bond behaviour of hooked bars was superior to that of straight bars for an equivalent length of 5 times the

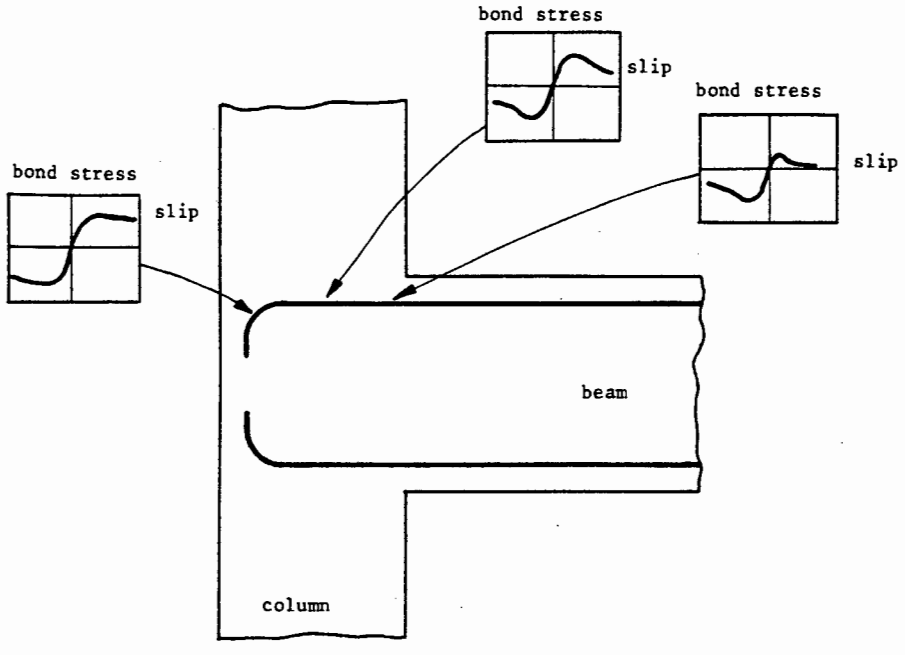

Figure 5.11 : Variation in bond stress-slip characteristics along anchored bar

diameter of the bar. The variation in the bond stress-slip relationship for an anchored bar is illustrated in Figure 5.11. Since the program assumes that the bond characteristics are identical along the beam, the question of how these characteristics are chosen needs to be addressed. If the properties at a bend are used, the model will show little degradation in strength, whereas using the properties at the centre of the bar will cause the model to predict pullout sooner than it would occur in reality. In most of the examples considered in section 5.4 and 5.5 total pullout does not occur and reasonable results were obtained when the bond characteristics at the centre of the anchorage length were used. The results are discussed further in section 5.5.

Another assumption concerns the slippage of the bars in the beam near the beam-column joint. This slippage contributes to the crack widths at the beam-column interface and depends on the extent of cracking along the beam. It was assumed that this slippage is approximated simply as a proportion of the slippage that occurs in the beam-column joint. In view of the other uncertainties involved, such an assumption does not seem unreasonable as long as pullout of the bar does not occur. Studies showed that by using 30-40% of the slippage in the beam-column joint for the slippage in the end of the beam, results for the fixed end rotation corresponded closely with the experimental results.

5.4 Parametric Study of a Cantilever using the Multi-layered Beam Model

Numerical studies using the proposed layered beam model were performed to investigate the effect of the parameters defining the material properties and numerical approximations. The beam chosen for these studies was from a

series of cantilever beams tested by Ma *et al* [33]. The beams are half-scale specimens of a typical girder in a 20 storey moment resisting frame. An assessment of the numerical results obtained for some of the other beams are presented in the following section.

The beam used for these particular studies is referred to as beam R-1 and was dominated by flexural behaviour. Details concerning the beam dimensions and reinforcement are given in Figure 5.12(a). The area of top steel is approximately twice the area of the bottom steel. The tip displacement was

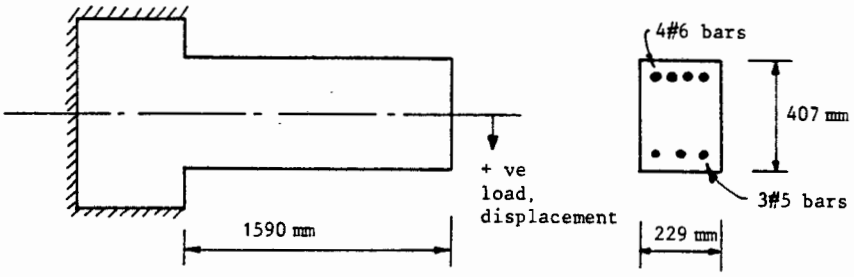

Figure 5.12(a) : Beam R-1

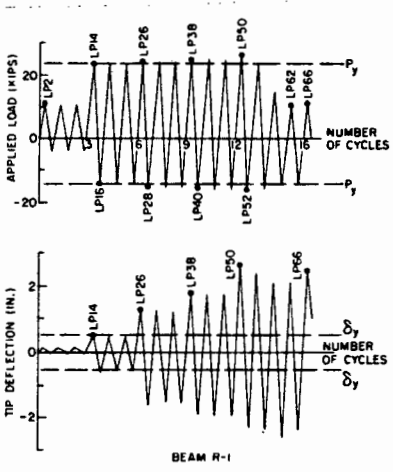

Figure 5.12(b) : Loading history (Beam R-1)

prescribed using the cyclic loading sequence shown in Figure 5.12(b). The experimental load-displacement response for the beam is given in Figure 5.13 where positive load and displacement are measured downwards. Failure of the beam was initiated when the bottom reinforcing bars started to buckle after load point 50 (LP50). This is apparent by the sharp decrease in strength which occurs from LP54 onwards.

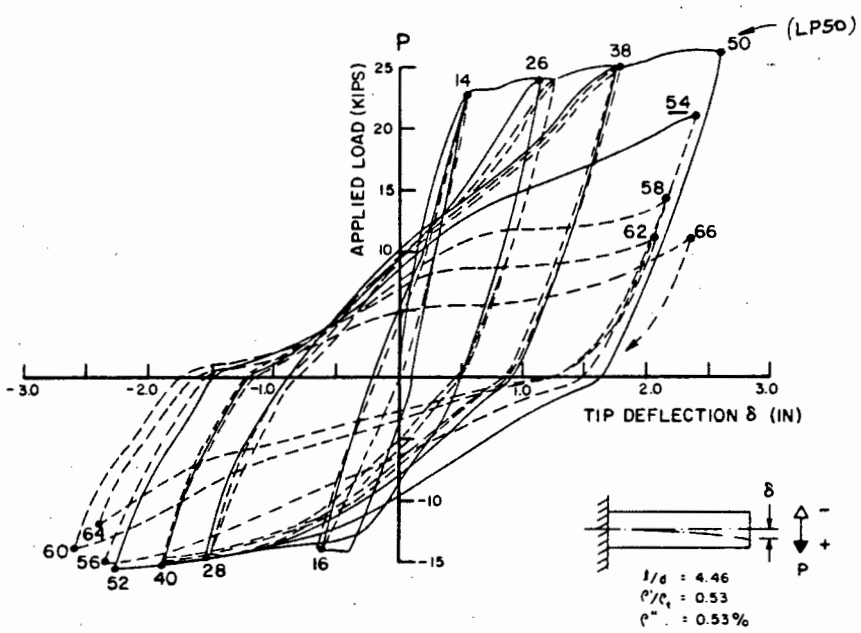

Figure 5.13 : Load-displacement response for Beam R-1

In the numerical studies with the multi-layered beam model, the concrete was modelled using 50 layers as illustrated in Figure 5.14. The properties used for the concrete constitutive model were based on the experimental concrete tests by Ma *et al* [33], and the amount of confining steel (ρ") . Similarly, the values given in [33] were used for the steel constitutive model. The parameters used for the bond stress-bond slip constitutive model were based on the experimental results given by Eligehausen *et al* [75] for a bar in well confined concrete. The values were adjusted for variations in factors such as bar size, concrete strength, etc., by using the modifications suggested in [75].

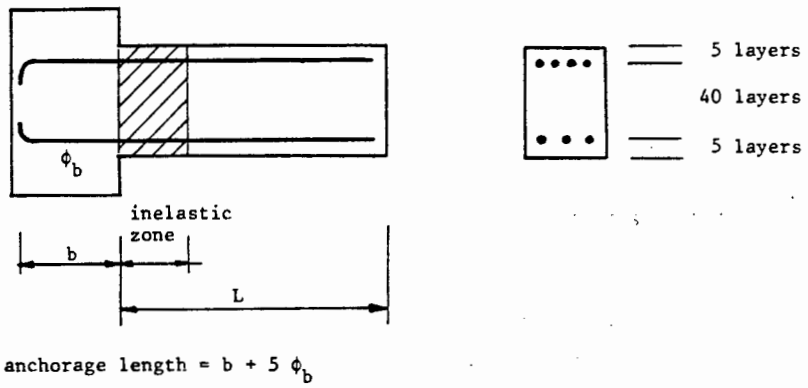

Figure 5.14 : Beam R-1, definitions for analytical model

The elastic stiffnesses and yield moments for bending in the positive and negative directions were obtained from the computer program used to calculate the moment-curvature response. The length of the inelastic zone was calculated using the expected maximum moment at the support and the yield moment. A length equal to 25% of the length of the cantilever proved satisfactory for the studies of beam R-1.

For the parametric study the following aspects were considered :

(i) the number of integration stations approximating the inelastic zone,

(ii) the bar slippage model,

(iii) the steel constitutive model,

(iv) the elastic stiffness,

(v) the concrete constitutive model,

(vi) the crack closure criterion.

The investigations into each of these aspects is now discussed.

The number of integration stations for the inelastic zone

For this investigation the results for the three analyses are presented. In the first, R-1A , 3 integration stations were used (n = 2 in Chapter 3). The load-displacement response is shown in Figure 5.15(a). The damage measures calculated at LP50 are given in Table 5.1. The stress-strain relations for the top and bottom steel layers are given in Figures 5.16(a) and 5.17(a) respectively. For the other two analyses, R-1B and R-1C , 5 and 7 integration stations (n = 4 and n = 6) were used respectively. The corresponding load-displacement responses are given in Figures 5.15(b) and (c), and the damage measures at LP50 in Table 5.1. Comparing the results for the three analyses, it is evident that the load-displacement responses are very similar and the differences in the damage measures are relatively small. Figures 5.18 shows the curvature distribution along the inelastic zone at LP50 for the three analyses.

Analysis	FDR	MFDR	Dissipated Energy kNm	E_n	Λ_f	Λ_a	Λ_c
R-1A	5.3	2.3	29.1	108	0.81	0.14	1.03
R-1B	5.4	2.5	28.5	106	0.81	0.15	1.03
R-1C	5.4	2.5	28.1	105	0.82	0.13	1.04
R-1D	6.5	2.7	42.2	156	0.85	-	1.04
R-1E	4.9	2.1	35.2	130	0.80	0.14	1.03
R-1F	5.4	2.2	29.0	107	0.81	0.14	1.03

Table 5.1 : Results of parametric study for Beam R-1

In summary, the results show that when only 3 integration stations are used for the numerical approximations in the inelastic zone, results are obtained which correspond closely with the results when more integration stations are used. Three integration stations are used for all further analyses presented in this chapter.

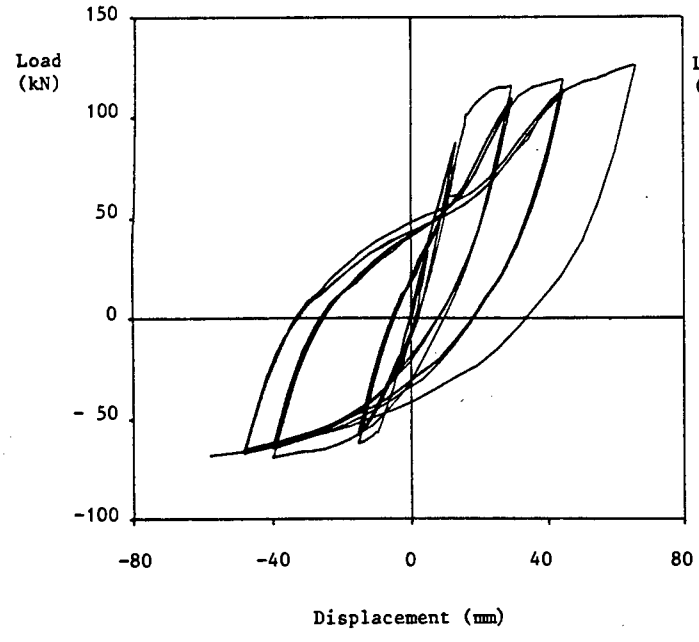

Figure 5.15(a) : Beam R-1A

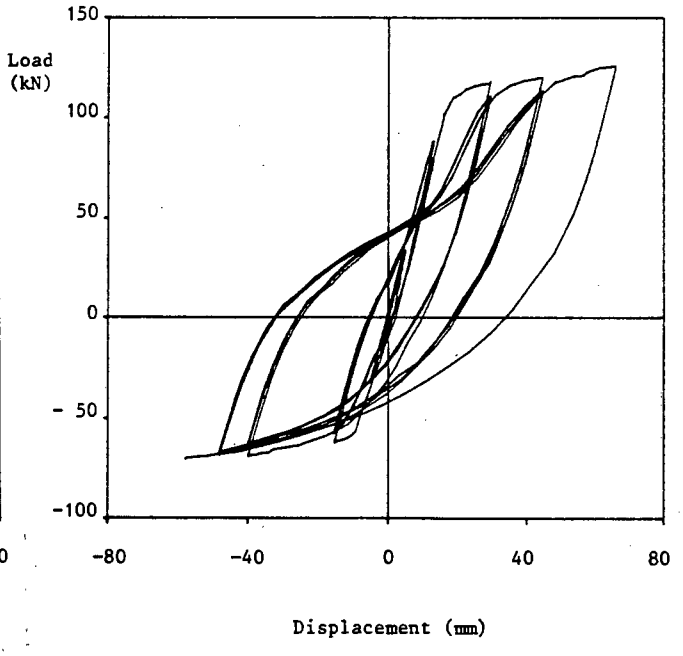

Figure 5.15(b) : Beam R-1B

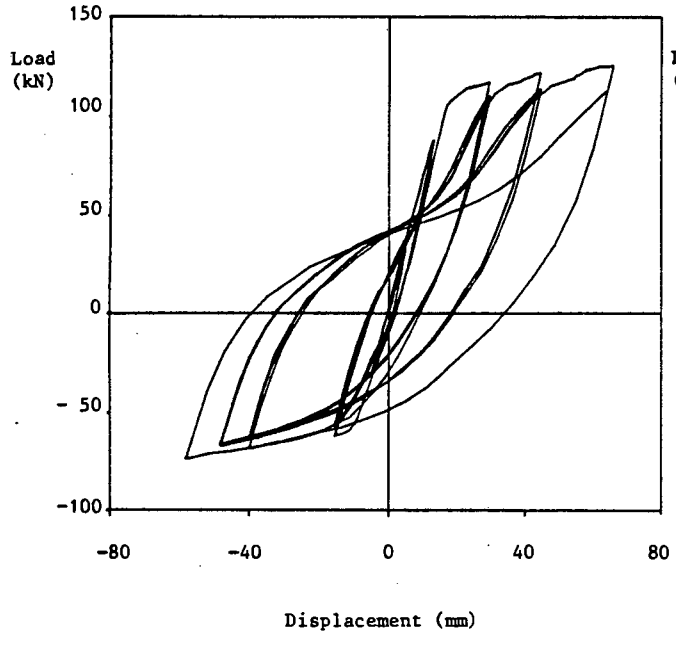

Figure 5.15(c) : Beam R-1C

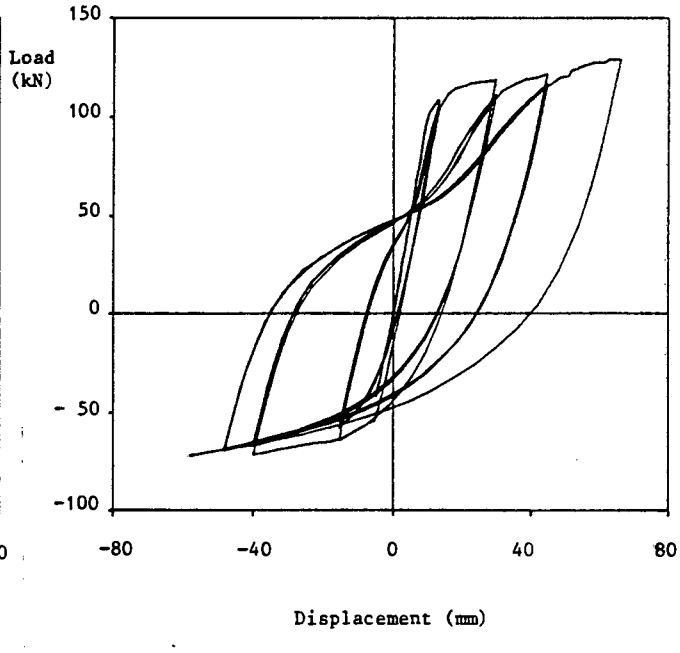

Figure 5.15(d) : Beam R-1D

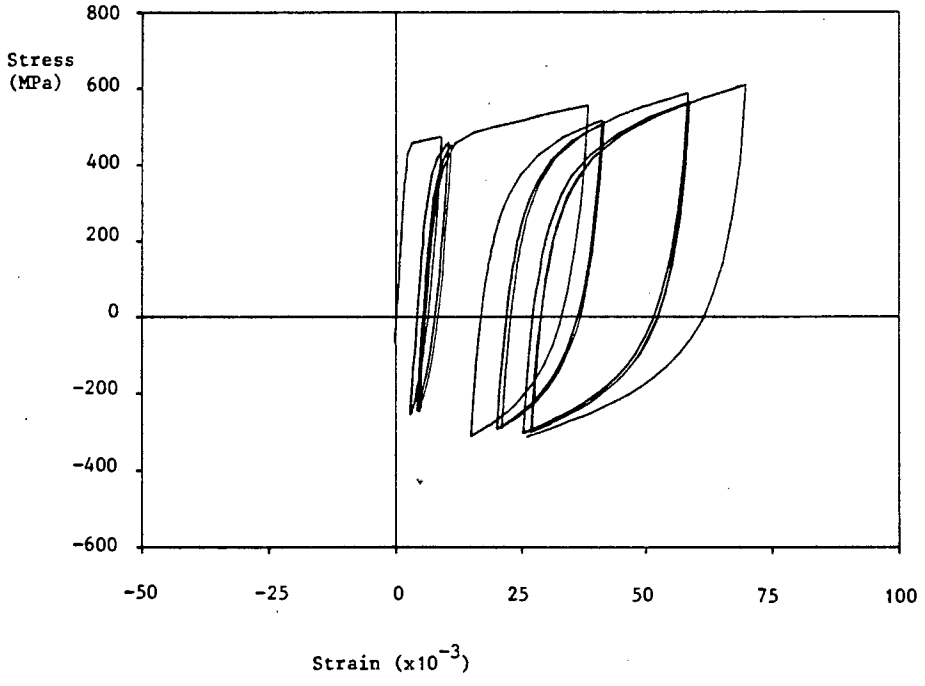

Figure 5.16(b) : Beam R-1D, top steel

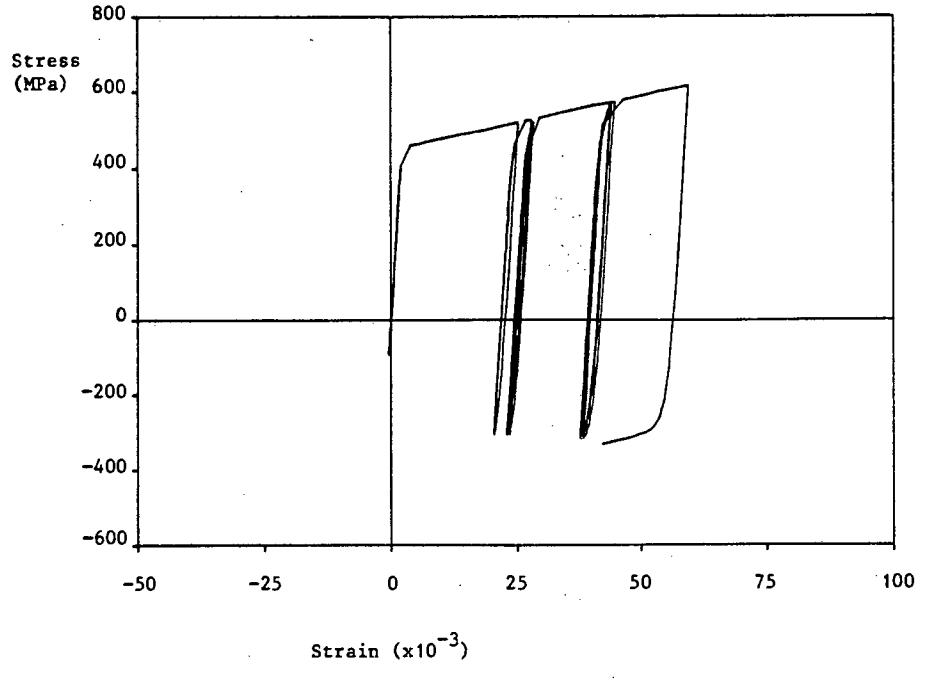

Figure 5.16(c) : Beam R-1E, top steel

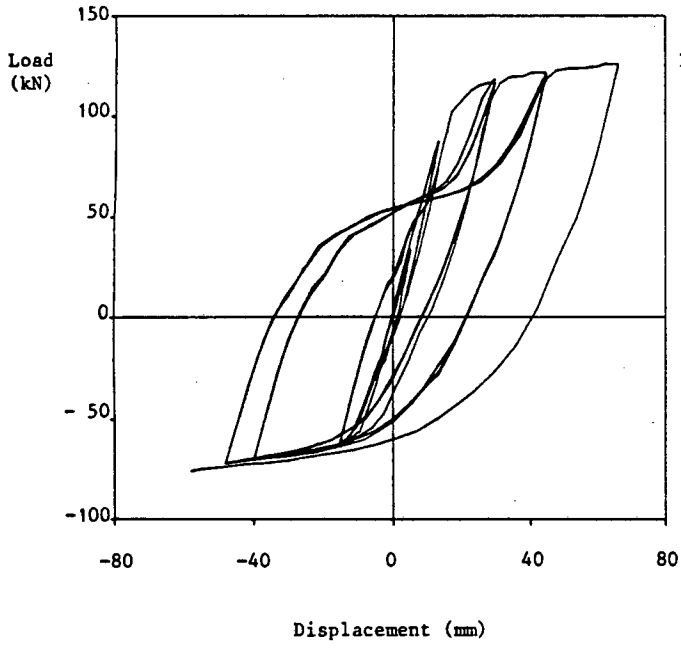

Figure 5.15(e) : Beam R-1E

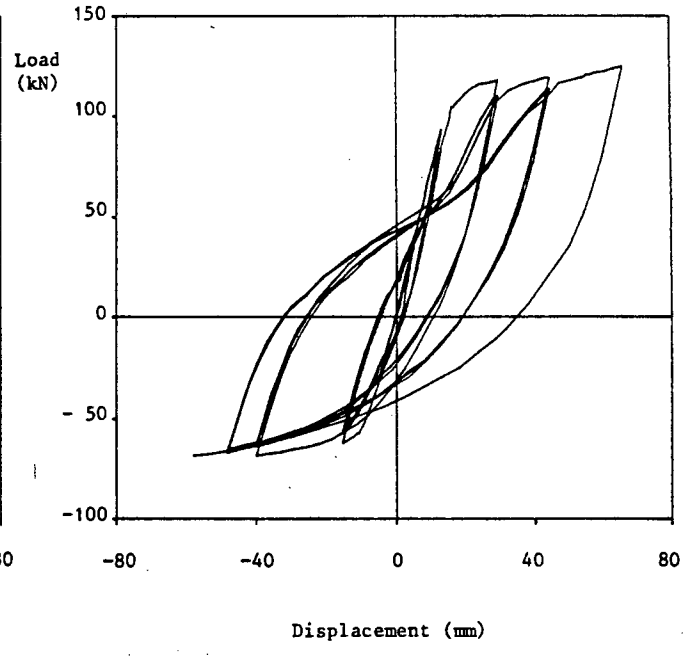

Figure 5.15(f) : Beam R-1F

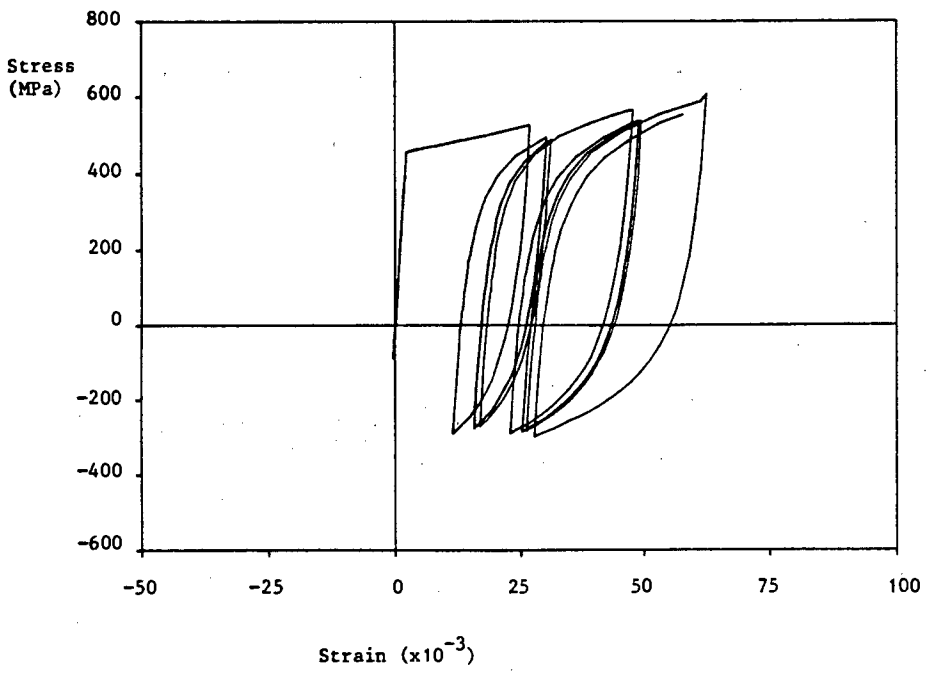

Figure 5.16(a) : Beam R-1, top steel

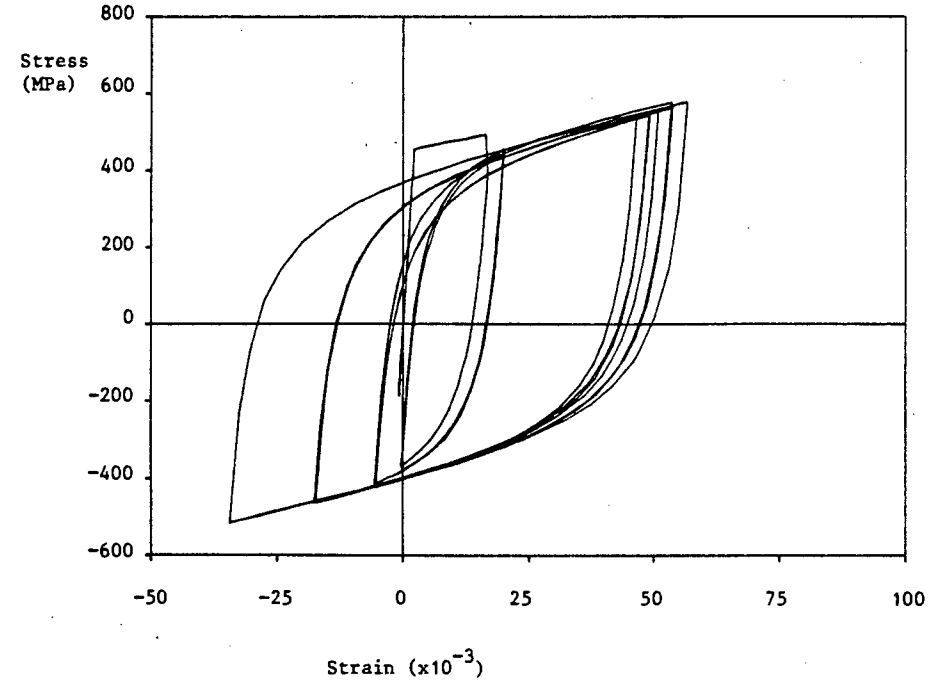

Figure 5.17(a) : Beam R-1A, bottom steel

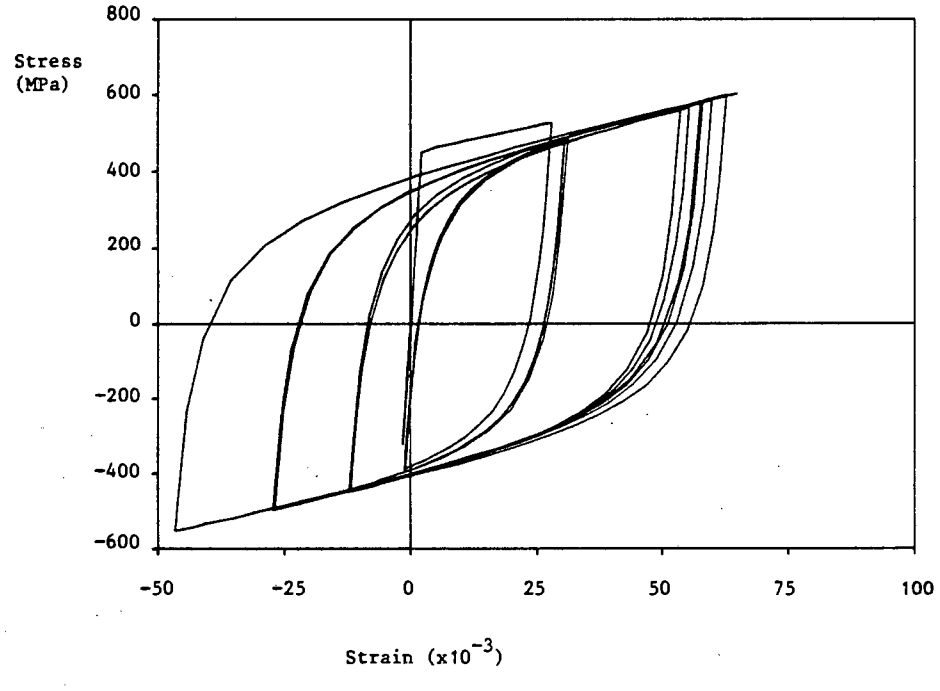

Figure 5.17(b) : Beam R-1D, bottom steel

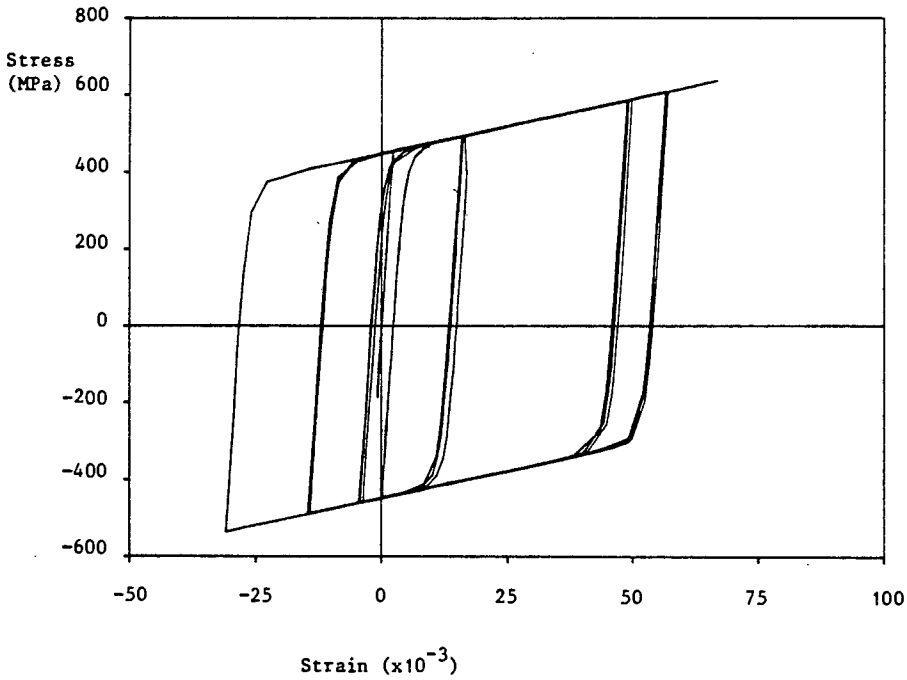

Figure 5.17(c) : Beam R-1E, bottom steel

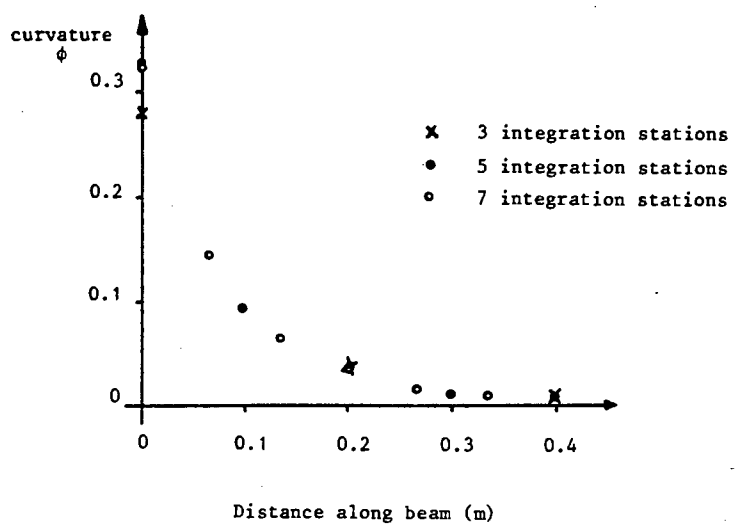

Figure 5.18 : Curvature distribution in inelastic zone

The bar slippage model

The purpose of this investigation was to determine the influence of the bar-slippage model on the calculated response of the proposed layered beam model. In analysis R-1D, the bar-slippage model was excluded from the numerical model of R-1A. The load-displacement response is given in Figure 5.15(d), and the top and bottom steel stress-strain relations are given in Figures 5.16(b) and 5.17(b) respectively. The results of R-1D confirms the expected behaviour of the beam when the bar-slippage is ignored. This is demonstrated by comparing the envelopes for the load-displacement responses in Figure 5.19, where for example, a displacement at a particular load in R-1A is larger than the corresponding displacement in R-1D. The steel stress-strain responses for the bottom bars indicate that larger compressive

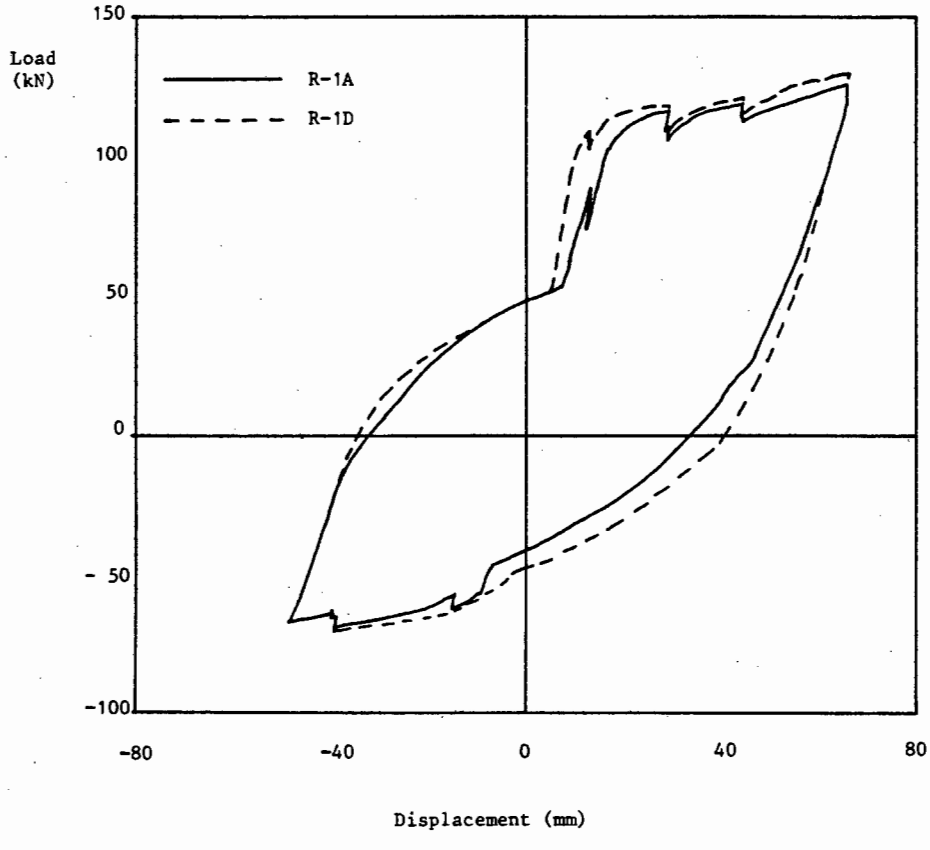

Figure 5.19 : Comparison of envelopes for R-1A and R-1D

strains are obtained for R-1D than R-1A. This is a result of the assumptions concerning bar-slippage and strain increment compatibility. Table 5.1 shows that significantly more energy is dissipated in R-1D as well as consistently higher values for all the other damage measures.

The steel constitutive model

It is generally accepted that the cyclic response of reinforced concrete beams is dominated by the behaviour of the steel. Two aspects of the steel behaviour that are important in defining the constitutive relation were studied. The first was the parameter used to define the amount of hardening. The actual stress-strain response for monotonic loading is shown in Figure 5.20. This is approximated by a bilinear model and clearly the slope chosen to represent the hardening depends on the maximum strain that is expected. The amount of hardening was found to have a significant influence on the response. The conclusion drawn from this was that it is important to choose this parameter carefully. The second aspect concerns modelling of the Baushinger effect. Experimental results given by Ma *et al*

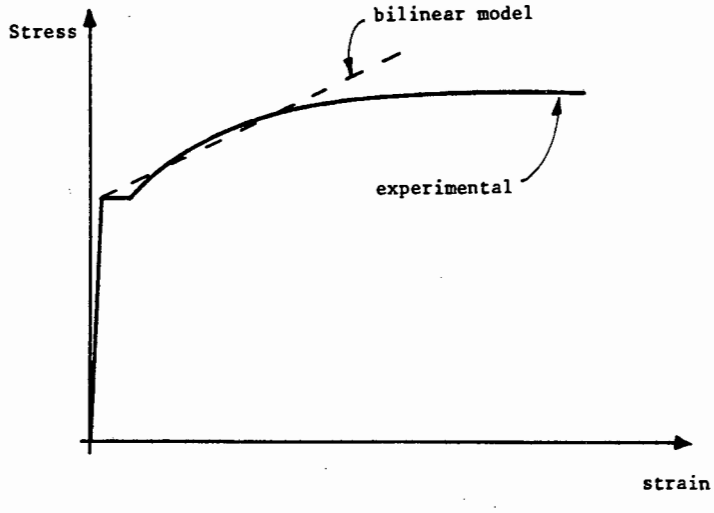

Figure 5.20 : Steel stress-strain relation

[33] were used to determine the parameters used to define the amount of curvature. These parameters were used in R-1A. An analysis was performed to determine whether a simpler bilinear elastic-plastic model could be used for the steel constitutive relation. For R-1E the curvature parameters were adjusted to obtain an approximately bilinear elastic plastic steel model. The load-displacement response is given in Figure 5.15(e), and the stress-strain relations for the top and bottom steel in Figures 5.16(c) and 5.17(c) respectively. The damage measures in Table 5.1 show a significant increase in the amount of dissipated energy when compared to R-1A. However, the amount of flexural damage decreases. A comparison of the envelopes for

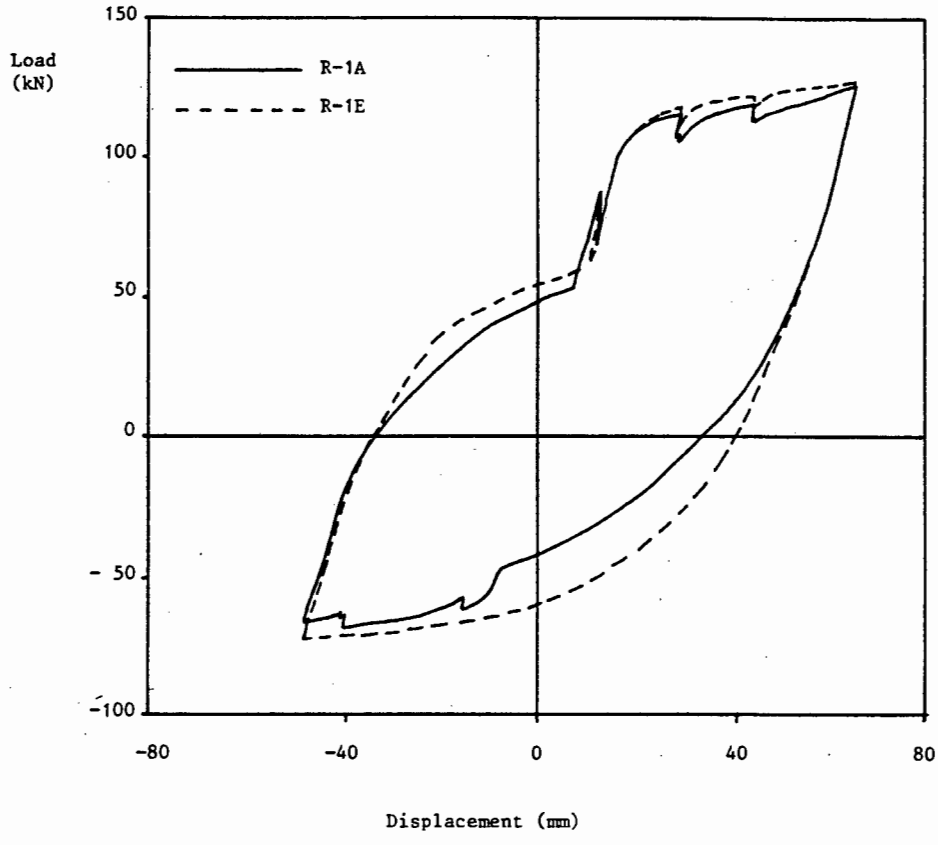

Figure 5.21 : Comparison of envelopes for R-1A and R-1E

the load-displacement responses in Figure 5.21 shows a significant difference in response when the load is acting up and when the load starts

to act downwards. These results show that a simpler constitutive model for the steel cannot be justified for reinforced concrete members subjected to large cyclically applied loads.

The elastic stiffness

As a result of the differences in the areas of the top and bottom reinforcement, the elastic stiffnesses for positive and negative bending differ. For beam R-1 the elastic stiffnesses are : $EI^{+} = 10.4 \times 10^{6}$ Nm^{2} and $EI^{-} = 15.4 \times 10^{6}$ Nm^{2} . In R-1A the average of these two stiffnesses was used for positive and negative bending. This assumption consequently reduced the computations required. An analysis R-1F, was performed in which the different stiffnesses for positive and negative bending were used. The load-displacement response for R-1F is given in Figure 5.15(f) and the damage measures in Table 5.1. A comparison of the results for R-1F and R-1A shows little difference. Therefore, using an average stiffness for rectangular sections is justified.

The concrete constitutive model

Variations in the material properties which define the concrete constitutive model were considered. The purpose was to determine the sensitivity of the analytical model's response. The one aspect that was found to have a notable effect on the response was the rate of softening of the concrete. This illustrates the importance of including a dependence of the amount of hoop steel in the model. Small variations in other material properties did not produce such notable differences in the response.

The crack closure criterion

Changes in the value of the initial crack width were found to have little effect on the response of the analytical model.

In summary, it is evident that the layered beam model produces results which are consistent with the expected trends. For example, the case of the beam modelled with the bar slippage effect included and compared to a model of the beam where the effect is ignored. The results also highlight the importance of including the Bauschinger effect in the steel constitutive model. It has also been shown that the inelastic zone can be adequately modelled with three integration stations.

5.5 Comparison of Results Predicted by Multi-layered Beam Model with Experimental Results

To validate the layered beam model, numerical results were compared with experimental results for a series of cantilever beams and an exterior beam-column connection. The experimental tests of Ma *et al* [33] were conducted with a series of cantilever beams, one of which was used in the parametric study in section 5.4. Five out of a total of nine tests were used in this

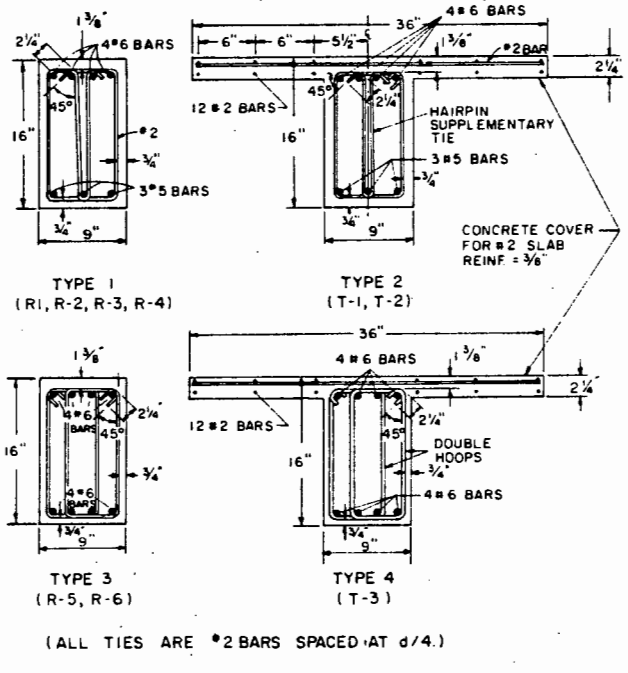

Figure 5.22 : Beam section details

study. The beams consisted of rectangular and T cross-sections, all with the same length. The reinforcement details are given in Figure 5.22. All but one of the beams examined in this thesis failed as a result of flexure. The exception was beam R-6 which failed as a result of shear. The loading histories are given in Figure 5.23. The beam-column connection was chosen from a series of tests conducted by Ehsani and Wight [31] in which the response was dominated by anchorage failure.

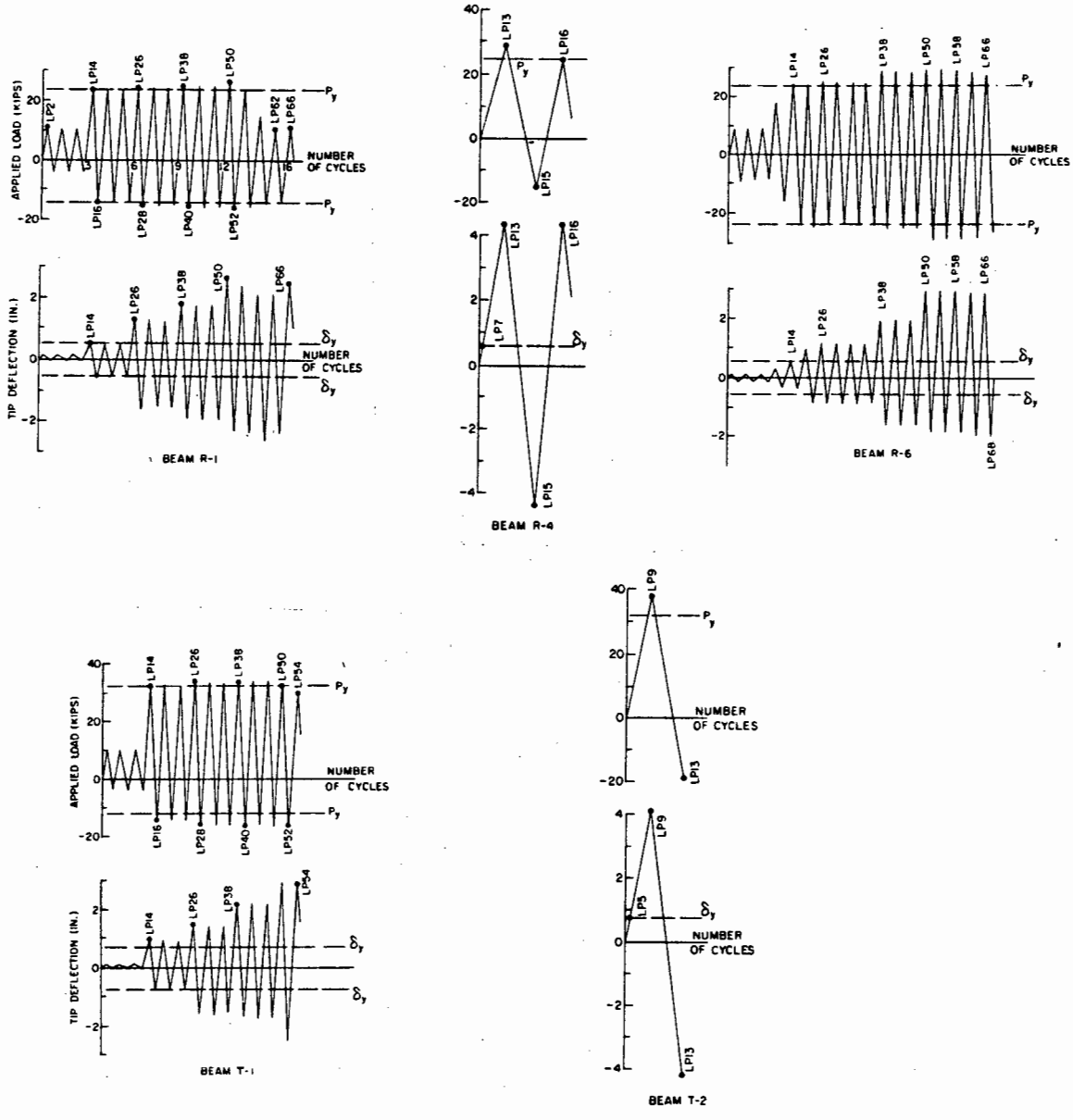

Figure 5.23 : Loading histories of Beams R-1, R-4, R-6, T-1 and T-2

For all the analytical results, 3 integration stations were used to approximate the inelastic zone. The yield moments were obtained by calculating the moment-curvature responses and the concrete was assumed to have no tensile strength. Bar-slippage at the end of the beam was taken as 40% of the slip in the anchorage block or beam-column joint.

BEAM R-1

The experimental and predicted load-displacement responses are given in Figures 5.24(a) and (b) respectively. The envelopes for these responses are

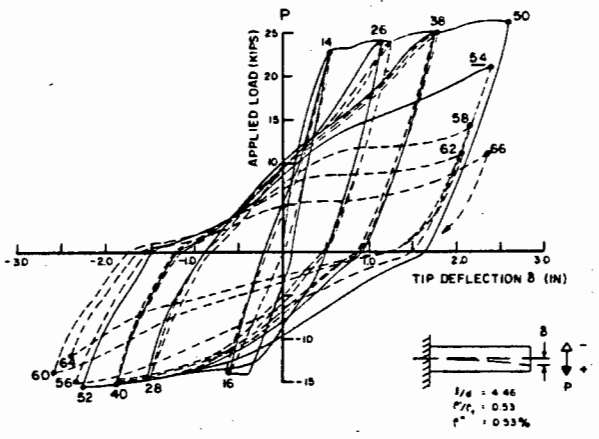

Figure 5.24(a) : Beam R-1, experimental response

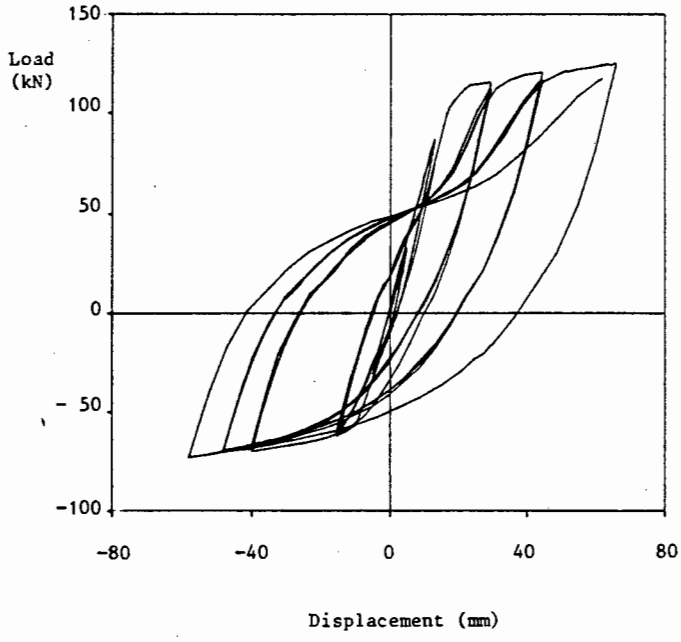

Figure 5.24(b) : Beam R-1, analytical response

compared in Figure 5.25. The results show that the analytical model tends to overestimate the load in the downward direction. The damage measures at various stages of the response are given in Table 5.2. In the first two

columns of Table 5.2, the percentage of the total displacement due to bar-slippage at the support is compared with the experimental results. The predicted results are considered acceptable in view of the assumptions made

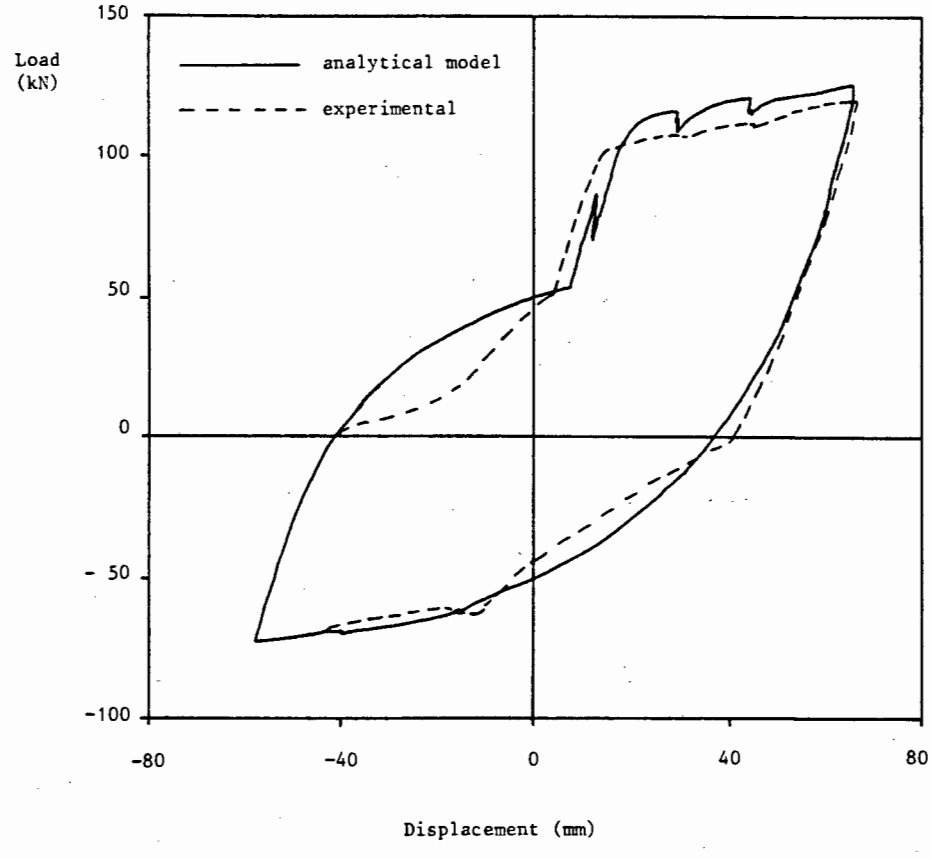

Figure 5.25 : Comparison of envelopes, Beam R-1

in modelling the bar-slippage. At LP50 the concrete at the joint started to lose its integrity and during the following cycle (LP54) failure of the beam occured when the bottom reinforcing bars buckled. The FDR and dissipated energy compare well with the experimental results and the results given by Banon [7]. The MFDR predicts that failure is initiated earlier than LP50. The amount of anchorage damage Λ_a is small when the beam fails. The concrete damage measure Λ_c correctly indicates that the concrete cover to the bottom reinforcing bars is lost between LP38 and LP50.

Load Point	% Bar-slippage Experimental	Predicted	FDR	MFDR	Dissipated Energy kNm	E_n	λ_f	λ_a	λ_c
LP14	25	34	1.1	0.	0.4	1	0.10	0.05	0.09
LP26	32	26	2.1	0.8	3.1	9	0.51	0.05	0.50
LP38	23	21	4.3	1.6	13.3	40	0.77	0.09	0.97
LP50	30	23	5.3	2.3	29.1	88	0.81	0.12	1.03
LP54			6.3	2.3	35.6	108	0.84	0.14	1.03
Experiment					37.8	123			
Banon *et al* [7]			6.8			116			

Table 5.2 : Results for Beam R-1

BEAM R-4

The beam R-4 is similar to R-1 in terms of reinforcement and concrete, however the loading history is very different and only consists of one large cycle. The load-displacement responses for the experimental and analytical

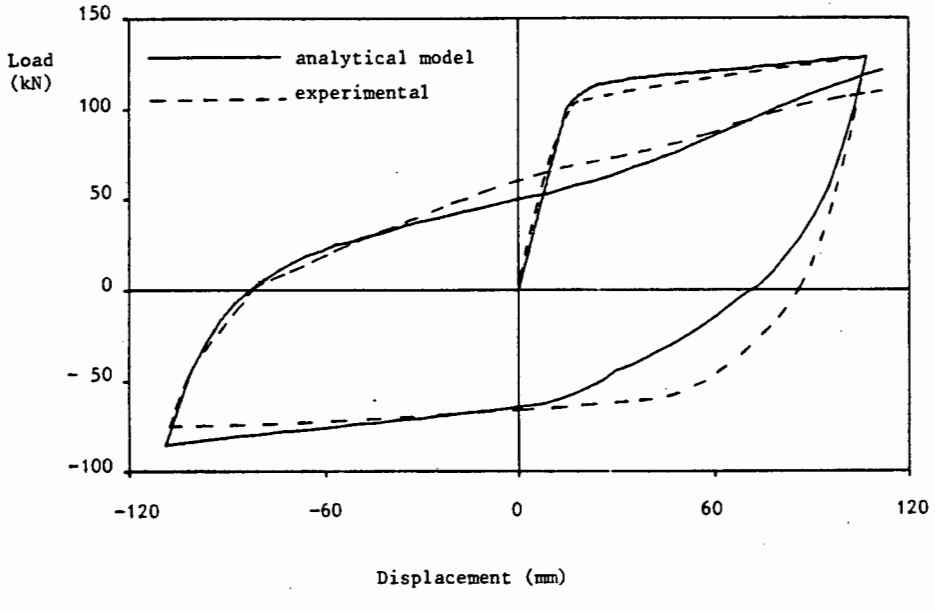

Figure 5.26 : Comparison of responses, Beam R-4

results are compared in Figure 5.26 and the damage measures given in Table 5.3. The predicted results correlate well with the experimental results up to LP13, but differ substantially when the loading is applied in the opposite direction. This explains the differences obtained for the dissipated energy. The predicted results correspond fairly well for the rest of the cycle to LP16. Buckling of the steel occurs during the end of the first cycle and beginning of the second cycle. The concrete damage measure at LP13 indicates that the concrete around the bottom steel bars is totally damaged.

Load Point	% Bar-slippage Experimental	Predicted	FDR	MFDR	Dissipated Energy kNm	E_n	Λ_f	Λ_a	Λ_c
LP13	25	23	6.3	2.9	9.2	35	0.84	0.14	1.01
LP16		26	10.4	3.1	26.0	99	0.90	0.20	1.01
Experiment					37.9	122			
Banon *et al* [7]			10.6			98			

Table 5.3 : Results for Beam R-4

BEAM R-6

This beam contains equal amounts of top and bottom reinforcement. The experimental load-displacement response is given in Figure 5.27(a) and the predicted response in Figure 5.27(b). The envelopes for these responses is compared in Figure 5.28. The predicted response is larger in both the positive and negative loading directions. The beam failed as a result of shear in the load cycles following LP50. Pinching of the load-displacement response is evident during these cycles. The layered beam model cannot reproduce the shear degradation and consequently does not show the pinching

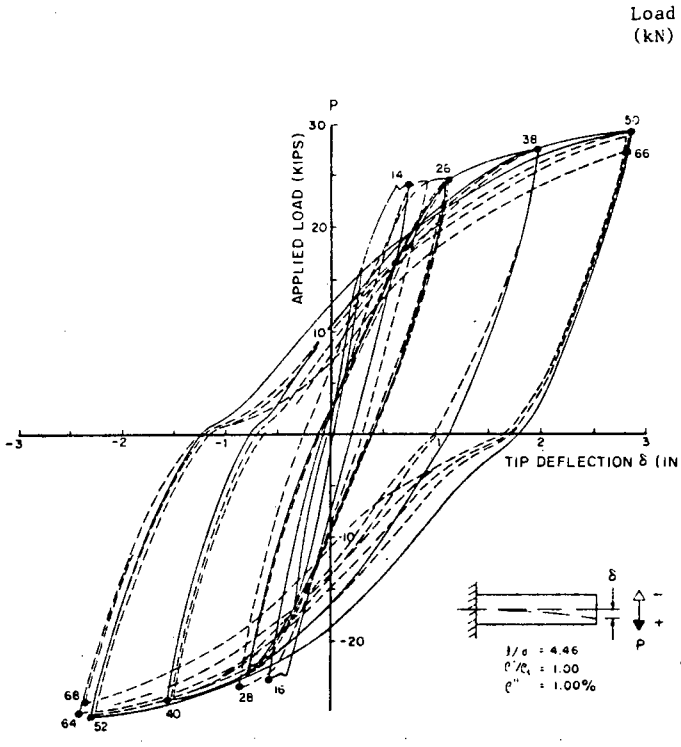

Figure 5.27(a) : Beam R-6, experimental response

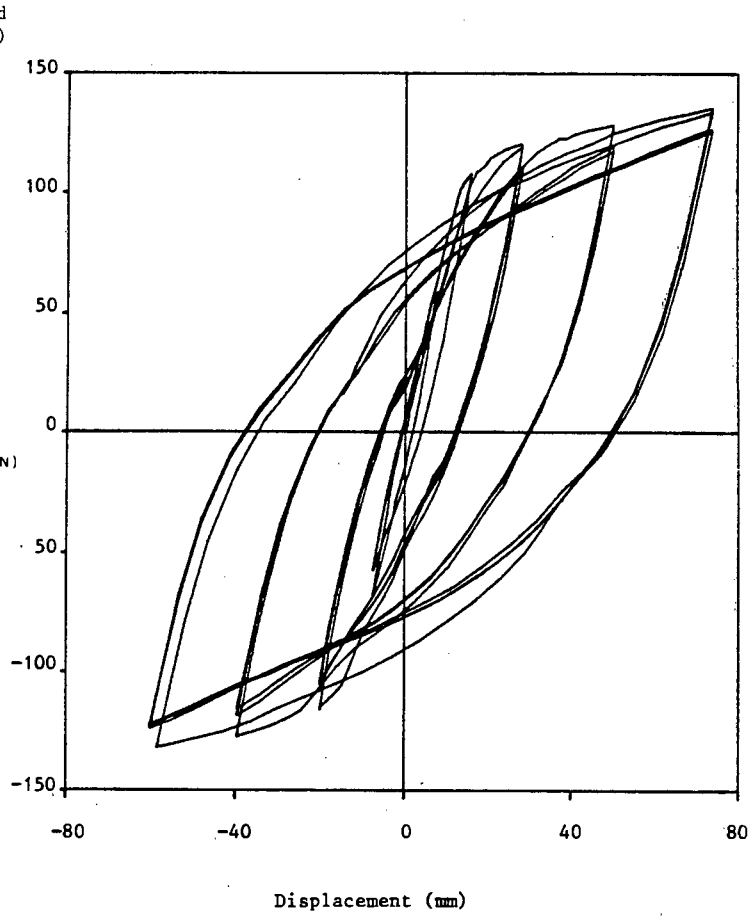

Figure 5.27(b) : Beam R-6, analytical response

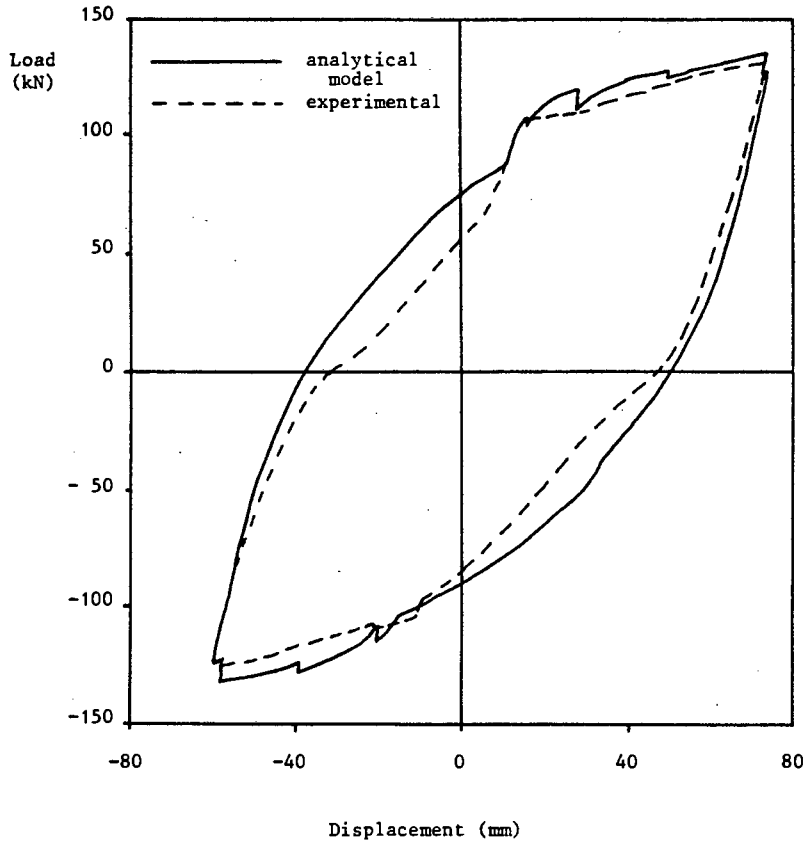

Figure 5.28 : Comparison of envelopes, Beam R-6

effect or predict failure at LP66. The damage measures are given in Table 5.4.

Load Point	% Bar-slippage Experimental	Predicted	FDR	MFDR	Dissipated Energy kNm	E_n	Δ_f	Δ_a	Δ_c
LP26	27	26	2.2	0.43	1.9	5	0.54	0.05	0.1
LP38	18	19	3.96	0.76	15.0	37	0.75	0.07	0.20
LP50	27	17	5.64	0.97	40.5	100	0.82	0.10	0.35
LP66			5.64	0.97	100.1	247	0.82	0.14	0.66
Experiment					83.4	206			
Banon *et al* [7]			7.4			182			

Table 5.4 : Results for Beam R-6

BEAM T-1

This beam has a T cross-section with different amounts of top and bottom reinforcement. The beam is modelled with different stiffnesses for positive and negative bending. The experimental and predicted load-displacement responses are given in Figure 5.29(a) and (b) respectively. A comparison of their response envelopes is given in Figure 5.30. The only parts of the response that do not correspond well are those where the load is reduced in the downward direction and increased in the upward direction. The beam failed in flexure with the bottom steel buckling before it fractured. The damage measures are given in Table 5.5. The analytical model predicts failure after LP38. The experimental results show that for LP50, the load is distinctly less than at LP38. Failure has clearly occurred by LP54.

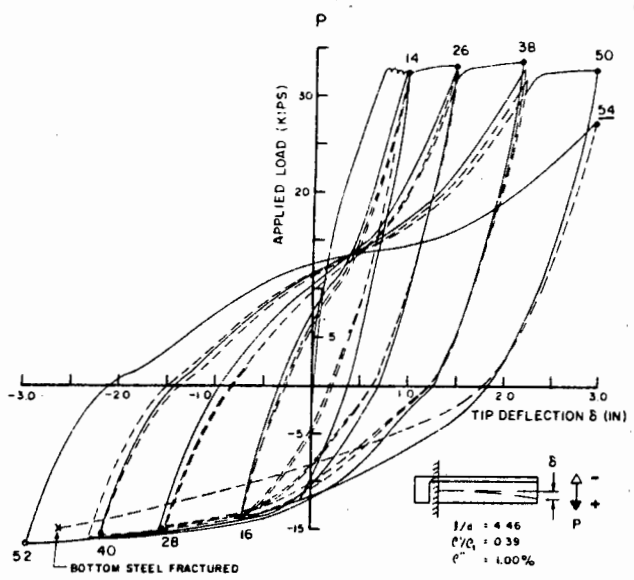

Figure 5.29(a) : Beam T-1, experimental response

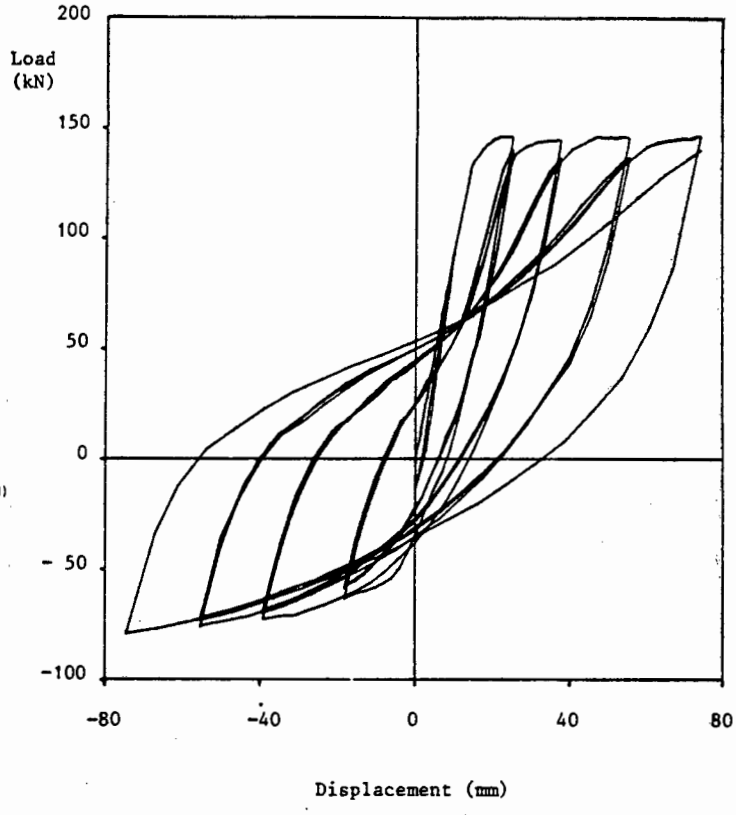

Figure 5.29(b) : Beam T-1 analytical response

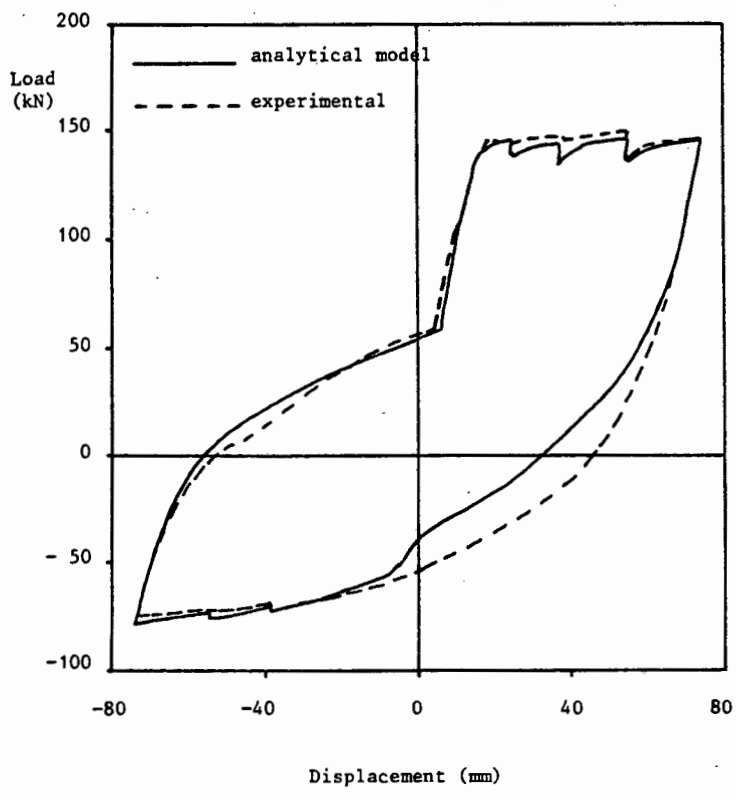

Figure 5.30 : Comparison of response envelopes, Beam T-1

Load Point	% Bar-slippage Experimental	Predicted	FDR	MFDR	Dissipated Energy kNm	E_n	Λ_f	Λ_a	Λ_c
LP26	38	22	3.0	1.1	7.2	22	0.66	0.05	0.97
LP38	37	22	4.4	2.1	20.0	62	0.77	0.13	1.0
LP50	42	25	5.6	2.9	39.7	123	0.82	0.19	1.01
LP54			6.3	3.0	48.2	149	0.84	0.24	1.01
Experiment					58.6	181			
Banon *et al* [7]			9.0			169			

Table 5.5 : Results for Beam T-1

BEAM T-2

The only difference between beams T-1 and T-2 is in the loading history. Beam T-2 had less than one cycle of loading before the bottom steel fractured. A comparison of the experimental and predicted load-displacement

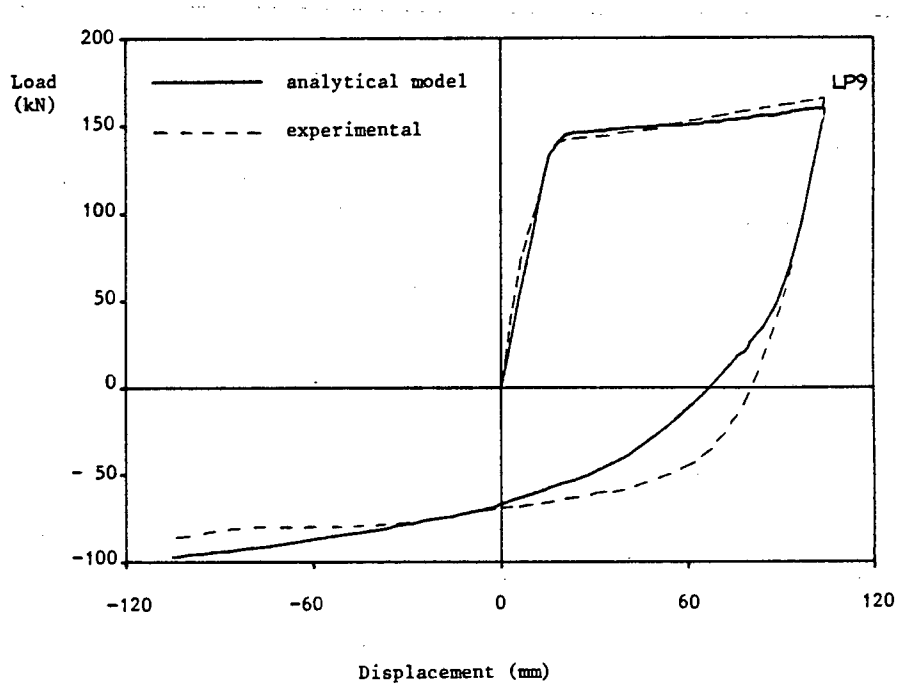

Figure 5.31 : Comparison of responses, Beam T-2

responses is given in Figure 5.31. Up to LP9 the results compare well, however when the loading is applied in the upward direction the results differ. The damage measures are given in Table 5.6.

Load Point	% Bar-slippage Experimental	Predicted	FDR	MFDR	Dissipated Energy kNm	E_n	Λ_f	Λ_a	Λ_c
LP 9	21	24	9.9	2.5	17.8	55	0.90	0.27	1.01
Experiment					26.4	81			
Banon *et al* [7]			11.4			63			

Table 5.6 : Results for Beam T-2

BEAM-COLUMN CONNECTION 4B

The configuration and dimensions for the beam-column connection tested by Ehsani and Wight [31] is given in Figure 5.32(a). The loading history used to prescribe the displacement at the tip of the cantilever is illustrated in Figure 5.32(b). The column has an initial axial force of 220 kN. The experimental load-displacement response is given in Figure 5.33. Halfway through the loading sequence pullout of the beam reinforcement from the joint occurred as well as some slippage of the column reinforcing bars. This resulted in a significant loss of strength and stiffness. Bar-slippage was modelled for the main reinforcing bars but not for the column reinforcement. The beam and columns were modelled with inelastic zones near the joint. For the beam, the reinforcement was approximated by two steel

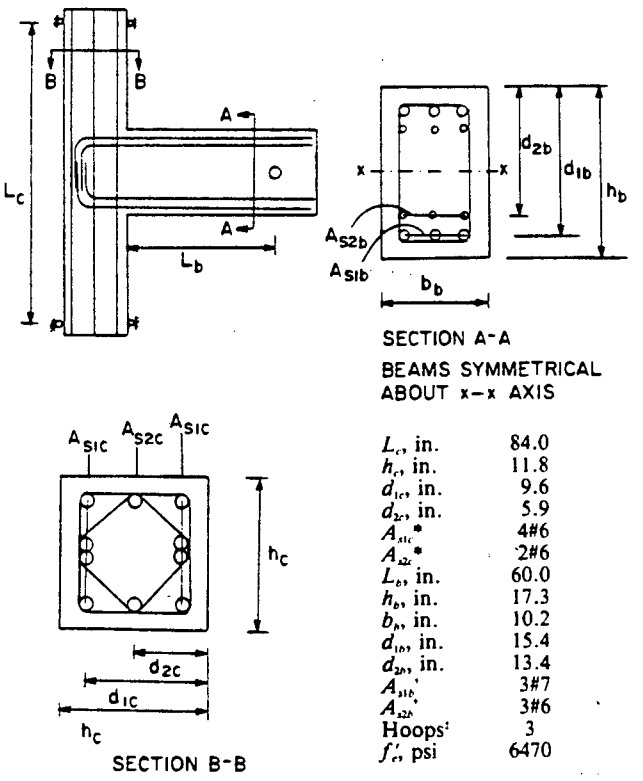

L_c, in.	84.0
h_c, in.	11.8
d_{1c}, in.	9.6
d_{2c}, in.	5.9
A_{s1c}*	4#6
A_{s2c}*	2#6
L_b, in.	60.0
h_b, in.	17.3
b_b, in.	10.2
d_{1b}, in.	15.4
d_{2b}, in.	13.4
A_{s1b}*	3#7
A_{s2b}*	3#6
Hoops*	3
f'_c, psi	6470

Figure 5.32(a) : Beam-column 4B

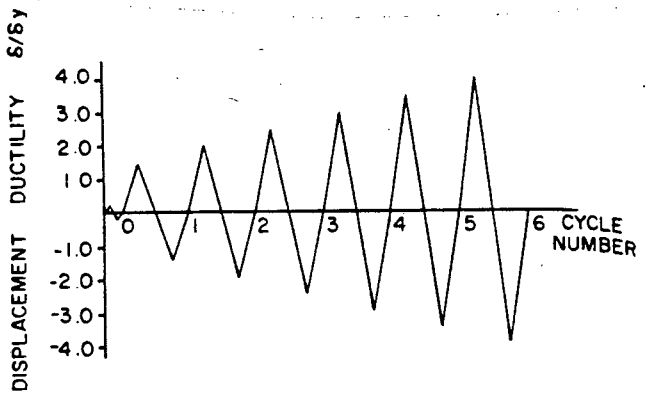

Figure 5.32(b) : Loading sequence

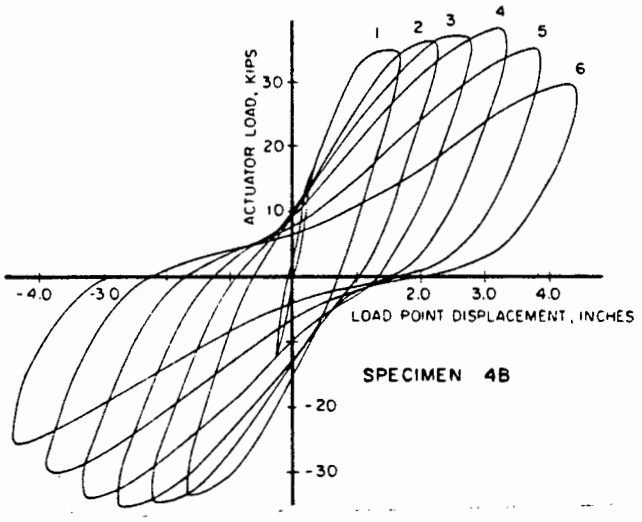

Figure 5.33 : Experimental results

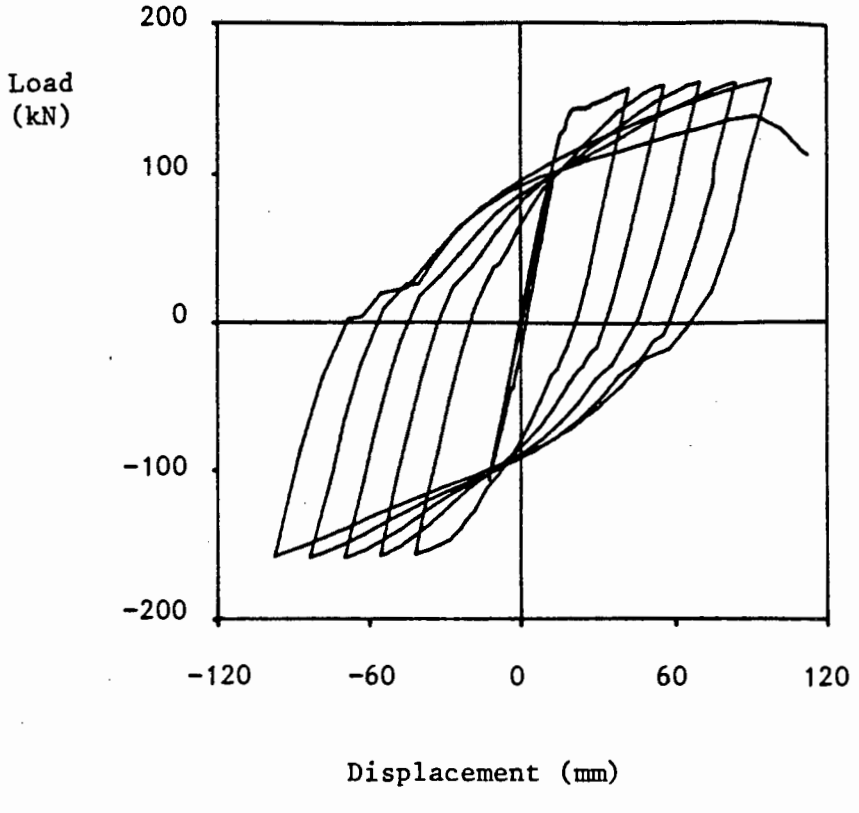

Figure 5.34(a) : Predicted response, sudden anchorage failure

layers, a top layer and a bottom layer. The analytical model predicted results which compared favourably with the experimental results up to the point when pullout started as shown in Figure 5.34(a). The experimental results showed some pinching due to shear and slippage of the column reinforcement. This was not reproduced by the analytical model. When pullout was predicted by the analytical model, it occurred suddenly and strength was lost quickly. In the experimental results the strength loss was more gradual. The reason for this difference is primarily the result of the assumption used for the bar-slippage model that the same bond stress-slip constitutive model applies at all integration points along the beam. By adjusting the rate at which damage occurred in the bond stress-slip relationship, pullout of the bars was not predicted during the response as illustrated in Figure 5.34(b).

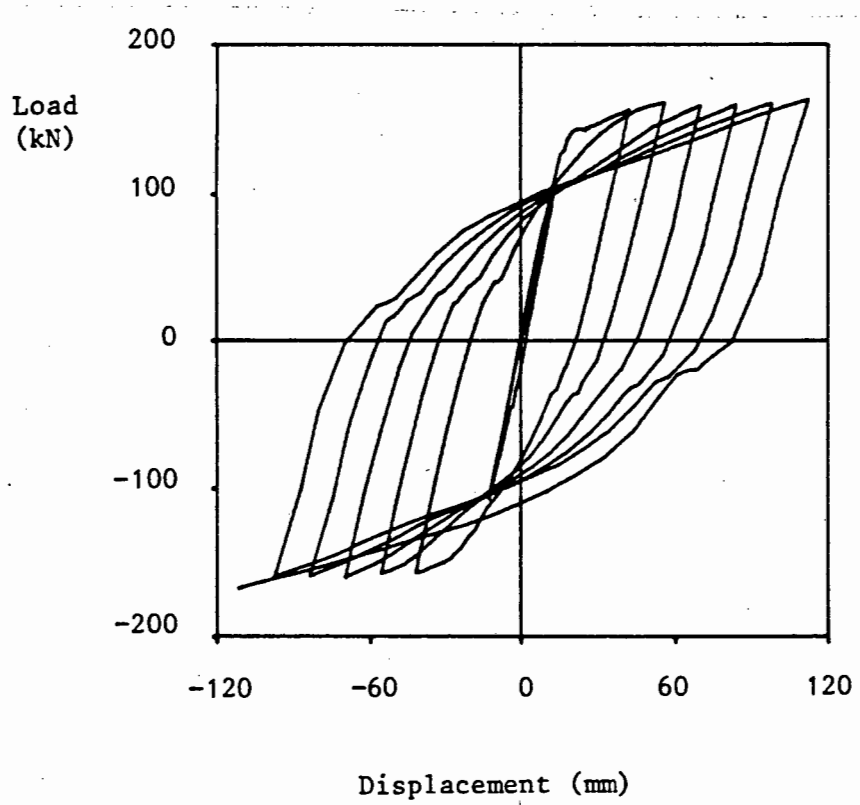

Figure 5.34(b) : Predicted response, no anchorage failure

Discussion of Results

The results obtained using the multi-layered beam model for flexurally dominated responses compare favourably with the experimental results. Differences were observed in two aspects of the load-displacement responses. The first concerns the higher loads achieved with downward loading for beams subjected to a number of cycles. This feature is not evident in beam R-4 and T-2 where only one large cycle of loading was considered. One likely explanation is that the concrete constitutive model does not consider any loss of strength or energy dissipation during unloading and reloading. The predicted model thus overestimates the strength of the concrete. The second aspect concerns the difference in the load-displacement response when the loading starts to be applied in the upward direction. This difference is significant at the larger cycles and results in the dissipated energy being underestimated. At first it was thought that the differences were the result of the unloading conditions in the concrete. However, a study showed little difference in the results that were obtained when the parameters of the concrete model were changed and when the crack closure criterion was varied.

A plausible argument for the differences concerns the mechanics of the crack closure. The experimental results indicate that the crack starts to close when the load is zero, whereas the analytical model predicts crack closure closer to the point of zero displacement. This would account for the diferences in the response between zero load and zero displacement, especially evident in beams R-4 and T-2. For loading in the opposite direction, the crack that is developed in the lower half of the beam is larger due to the differences in area of the top and bottom reinforcing steel. Consequently, crack closure occurs around the point of zero displacement. The differences in the predicted and experimental results are

not significant in this case, see the response of beam T-1 for example. Thus the mechanics concerning the crack closure are not modelled accurately enough in one loading direction. There are two possible reasons for this, either the crack closure criterion needs to be adjusted to account for the loading direction, or the bar-slippage characteristics are not modelled accurately enough. In respect of the dependence of crack closure on loading direction, a plausible explanation could be that for loading in the downward direction, small pieces of broken concrete would be trapped in the crack thereby resulting in early closure of the crack. When the loading is in the upward direction, broken concrete would tend to fall away from the crack. As far as the bar-slippage characteristics are concerned, a straightforward explanation is not forthcoming. In tension, the bar-slippage model underestimates the amount of slip due to the assumptions of a uniform bond stress slip relationship along the anchored bar. Numerical tests were conducted in which the amount of slippage in the top steel was artificially increased for beam T-2. The results obtained were somewhat closer to the experimental results. Further numerical studies are required using a more accurate bar-slippage model to ascertain the influence of this aspect on the response of the beam. It would therefore appear that the bar-slippage model requires variable bond stress-slip constitutive models in order to rectify the above problem and to predict pullout correctly in the response of the beam-column connection 4B.

Generally, the FDR and dissipated energy damage measures produced results similar to those given by Banon *et al* [7]. The MFDR damage measure tended to predict the onset of failure sooner than when it occurred in the experiments. The anchorage damage measure Δ_a was generally small for all the cantilever examples. However, it was shown to be capable of predicting

the onset of pullout in the beam-column connection example. It was noticed to be very sensitive to the rate of strength degradation allowed in the bond stress-bond slip constitutive model. The concrete damage measure Λ_c predicted the onset of strength degradation in all the experiments which failed with buckling of the bottom bars. Further experimental results are required to substantiate the critical strain value used in calculating Λ_c. The damage measure can be enhanced by including some dependence on the shear action at the beam-column interface. The analytical model would then be able to predict the failure of beams such as R-6.

CHAPTER 6

TWO-LAYER BEAM MODEL

A simplified analytical model in which the concrete is modelled using only two layers, is presented in this chapter. The multi-layered beam model described in Chapter 5 requires a large amount of data manipulation, storage and computational time when for example 50 layers are used to model the concrete. The purpose of the two-layer model is to provide a computationally efficient model for the cyclic response of reinforced concrete beams. By 'computationally efficient' it is implied that the model requires less storage, less computational time and retains a certain degree of accuracy. The important aspects that need to be addressed in developing such an approximation include the area and position of the concrete layers and the concrete stress-strain relation to be attributed to the two concrete layers. The moment-curvature relationship forms the basis of the procedure used to evaluate these quantities. This is discussed in section 6.1 followed by a comparison of the results obtained using the multi-layered approach in Chapter 5.

6.1 Moment-Curvature Relationship

The procedure to determine the position, area and constitutive relation of the two concrete layers, uses the monotonic moment-curvature relationship for a section in which the concrete is modelled with 50 layers. The first step is to determine this relationship over the expected range of curvatures. This relationship for beam R-1 in positive bending is shown in Figure 6.1. At a particular curvature ϕ , the distribution of stresses and

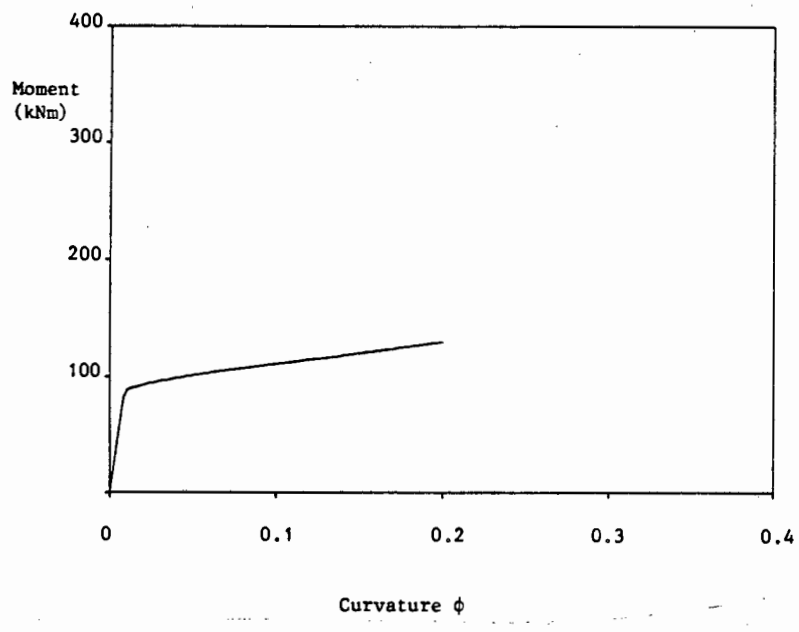

Figure 6.1 : Moment-curvature relationship (50 layers)

forces acting at the section is shown in Figure 6.2. The distributed compressive force in the concrete can be represented by an equivalent force F_c^{eq} which is equal to the total force in the concrete. The equivalent force F_c^{eq} acts at a position $\bar{y}$ above the bottom of the beam, such that the moment for the section remains the same. Assuming that the equivalent force F_c^{eq} is the force in a single layer of concrete with its height given by $\bar{y}$, then the stress in the concrete layer $\sigma_{\bar{y}}$ can be determined from the stress profile as shown in Figure 6.2. The area of the layer is then simply given as

$$A_{\bar{y}} = \frac{F_c^{eq}}{\sigma_{\bar{y}}} \quad . \qquad (6.1)$$

The equivalent force is calculated for other curvatures ϕ_j , in the range of interest. The subscript j is used to distinguish the results for one curvature from another. The equivalent forces are then $(F_c^{eq})_j$, the positions $(\bar{y})_j$ and the concrete areas $(A_{\bar{y}})_j$.

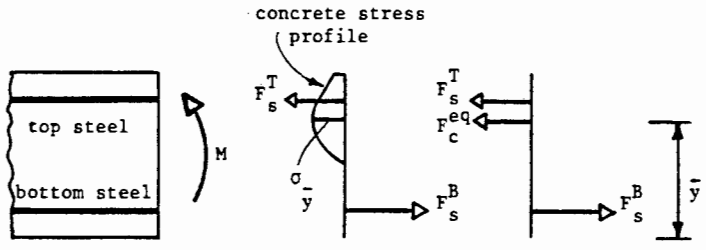

Figure 6.2 : Equivalent force at a section

Average values for the concrete areas and the positions are calculated and defined as

$$A_{avg} = \text{average} \left\{ (A_{\bar{y}})_j \right\} \tag{6.2}$$

$$\bar{y}_{avg} = \text{average} \left\{ (\bar{y})_j \right\} \quad . \tag{6.3}$$

These values now define the area and position of the top concrete layer. A similar procedure can be followed using the moment-curvature relationship for negative bending to determine the area and position for the bottom concrete layer.

The constitutive relation for the equivalent concrete layer can be determined by using the area and position of the concrete layer with the moment-curvature relationship for the multi-layered model at specified curvatures ϕ_j . The equivalent stress for ϕ_j can be obtained by dividing the equivalent force by the area of the equivalent concrete layer

$$(\sigma^{eq})_j = \frac{(F_c^{eq})_j}{A_{avg}} \quad . \tag{6.4}$$

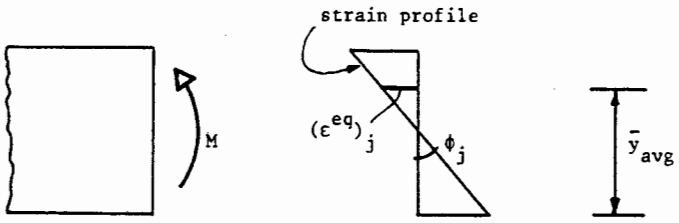

Figure 6.3 : Equivalent strain for concrete layer

Using the strain profile for ϕ_j and the position of the layer $\bar{y}_{avg}$, the equivalent strain for the concrete $(\epsilon^{eq})_j$ can be obtained as shown in Figure 6.3. The equivalent stress and equivalent strain values are obtained at all the specified curvatures ϕ_j . The resulting stress-strain relationship for the top concrete layer is depicted in Figure 6.4 where the circles indicate the results obtained for each prescribed curvature. The parameters defining

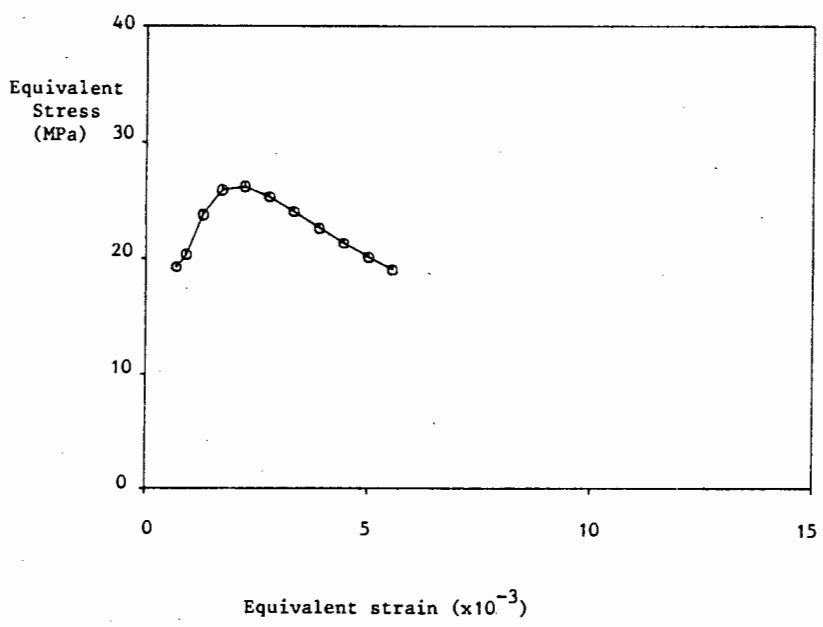

Figure 6.4 : Equivalent stress-strain relation for top concrete layer

the concrete damage constitutive relation are adjusted to obtain a stress-strain relation for monotonic loading which matches the equivalent stress-strain relationship as closely as possible over the expected strain range. These two relations are compared in Figure 6.5.

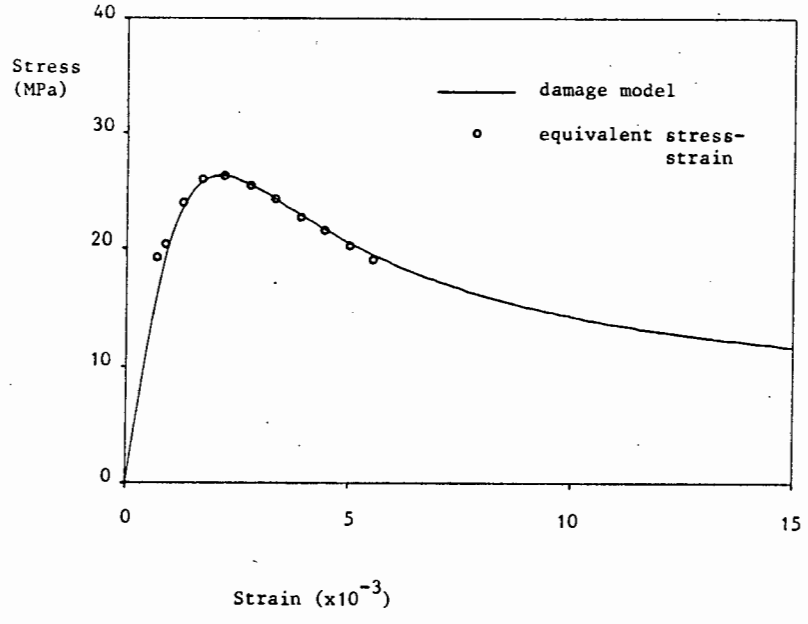

Figure 6.5 : Constitutive relation for top concrete layer

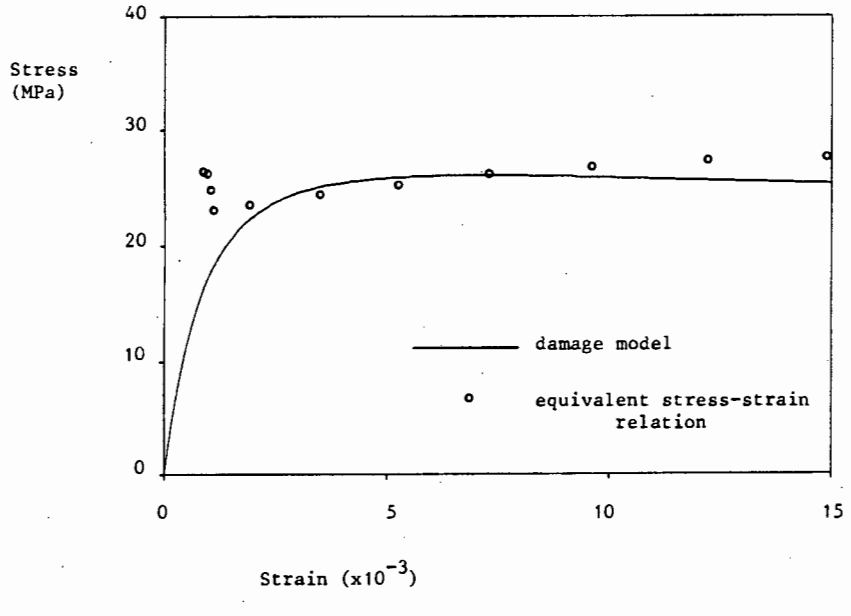

Figure 6.6 : Constitutive model for bottom concrete layer

The matching process is more difficult for the bottom concrete layer. It is not possible to obtain a damage constitutive relation to match the equivalent stress-strain relationship shown in Figure 6.6 at all strain measures. The equivalent stress-strain relation at the lower strains ($\sim 1 \times 10^{-3}$) occurs when the section starts to yield. Since the maximum expected strains are of the order 10×10^{-3} , the relationship is matched in the range of strains $5 - 10 \times 10^{-3}$. Consequently, poor correlation for the moment-curvature response is expected when yielding occurs.

The moment-curvature relationship for the two-layer approximation of the section is compared in Figure 6.7 with the moment-curvature relationship obtained using 50 concrete layers. Further insight into the behaviour can

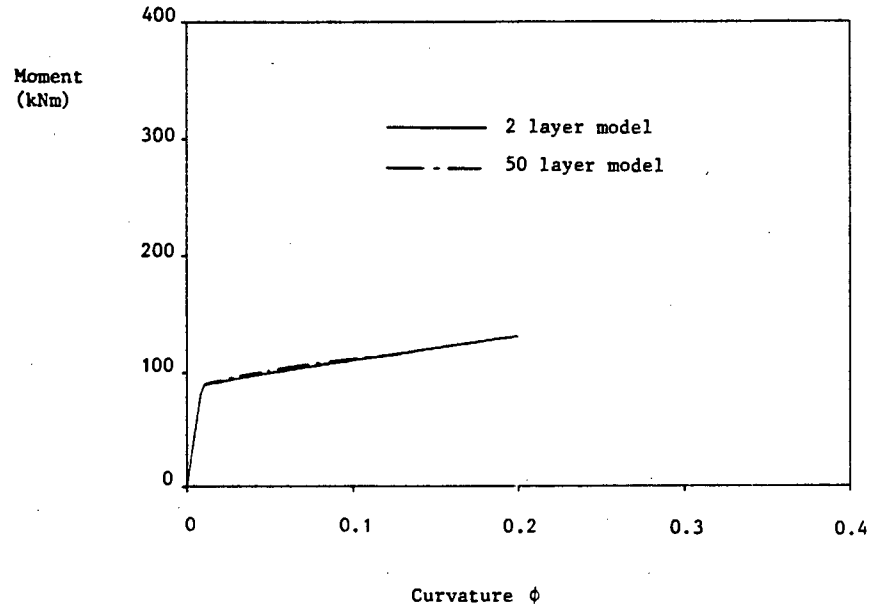

Figure 6.7 : Moment-curvature relationship for positive bending moment

be obtained by making a similar comparison for the total concrete force plotted against the strain in the top steel layer; this comparison is shown in Figure 6.8. The relationships show that the two-layer approximation

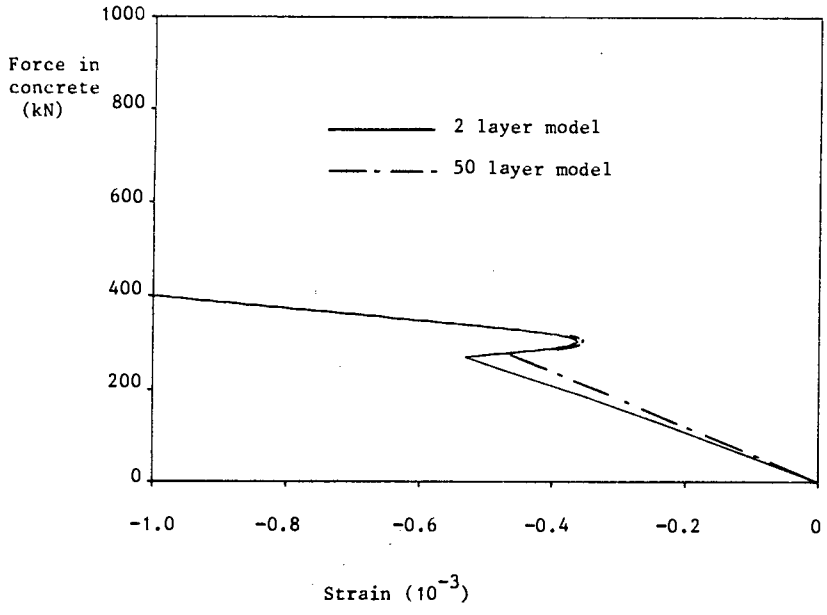

Figure 6.8 : Force-strain relationship for top concrete (positive bending moment)

produces good results for all strain measures. The results for negative bending are given in Figures 6.9 and 6.10. The results clearly show that around the yield point the correlation is poor but improves at larger strains.

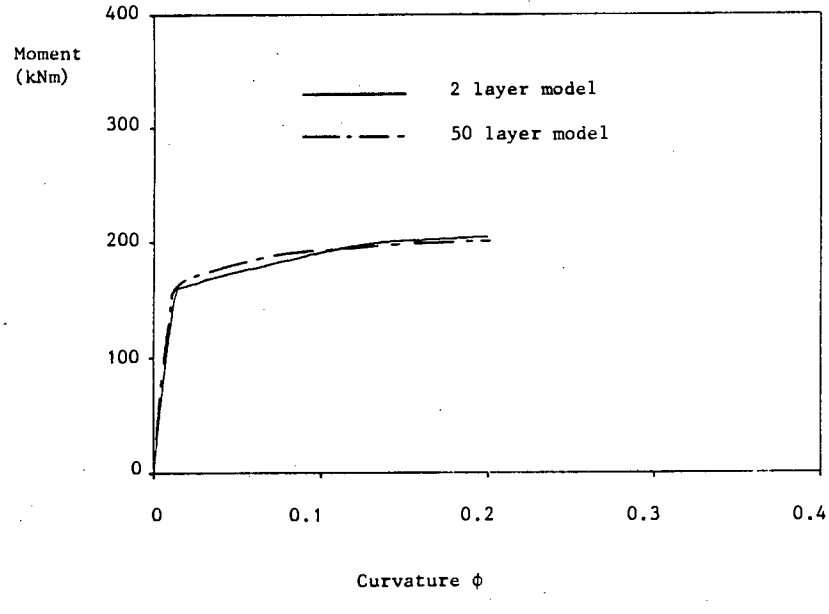

Figure 6.9 : Moment-curvature relationship for negative bending moment

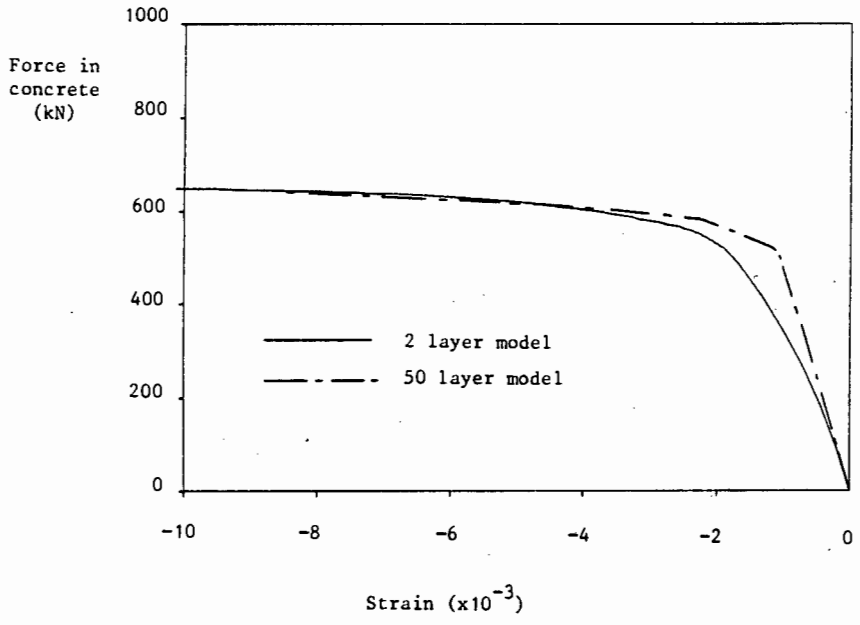

Figure 6.10 : Force-strain relationship for bottom concrete (negative bending moment)

If it was necessary to reproduce the response around the yield point only, then different parameters for the constitutive relation would have to be used. The section would then not be able to approximate the response for larger curvatures very well.

The cyclic response of the constitutive model for the equivalent concrete layers is assumed to be identical to the behaviour of a layer in a multi-layered model. Since the concrete damage model ideally unloads to the origin, such an assumption can be justified.

6.2 Results for Two-layer Beam Model

In this section, the results for the cyclic response of the cantilever beams using the two-layer beam model are compared with the results for the

multi-layered model presented in Chapter 5. The procedure outlined in section 6.1 was used to obtain the equivalent concrete layers and their constitutive relations for each of the cantilever beams. The critical damage variable used in the concrete damage measure Λ_c is obtained from the moment-curvature relationship for the two-layer model. It is defined as the damage variable for the equivalent concrete layer at the failure curvature. This failure curvature is the curvature at which the concrete damage measure Λ_c , in the multi-layered model reaches the value of one. The remaining damage measures have the same definitions as in the multi-layered model.

The results obtained for beam R-1 using 50 concrete layers and two concrete layers are given in Figures 6.11(a) and (b) respectively. A comparison of their load-displacement response envelopes is shown in Figure 6.11(c). The stress-strain responses for the top and bottom steel layers are given in Figures 6.11(d) - (g). The load-displacement responses for beams R-4, R-6, T-1 and T-2 using 50 layers and the two-layer model are presented in Figures 6.12 - 6.15 respectively. The damage measures for all the beams are given in Table 6.1.

Beam	% Bar slippage Experimental	Predicted	FDR	MFDR	Dissipated Energy kNm	E_n	Λ_f	Λ_a	Λ_c
R-1 (50 layers) LP50	30	23	5.3	2.3	29.1	88	0.81	0.12	1.03
R-1 (2 layers) LP50	30	20	5.5	1.9	30.0	91	0.82	0.13	1.02
R-4 (50 layers) LP13	25	23	6.3	2.9	9.2	35	0.84	0.14	1.01
R-4 (2 layers) LP13	25	17	6.5	2.3	10.0	38	0.85	0.12	1.01
R-6 (50 layers) LP66		19	5.6	0.97	100.1	247	0.82	0.14	0.66
R-6 (2 layers) LP66		16	6.0	0.85	101.5	250	0.83	0.14	0.62
T-1 (50 layers) LP50	42	25	5.6	2.9	39.7	123	0.82	0.19	1.01
T-1 (2 layers) LP50	42	24	5.5	2.7	40.0	124	0.82	0.17	1.01
T-2 (50 layers) LP 9	21	24	9.9	2.5	17.8	55	0.90	0.27	1.01
T-2 (2 layers) LP 9	21	20	11.2	2.3	18.8	58	0.91	0.20	1.01

Table 6.1 : Comparison of damage measures

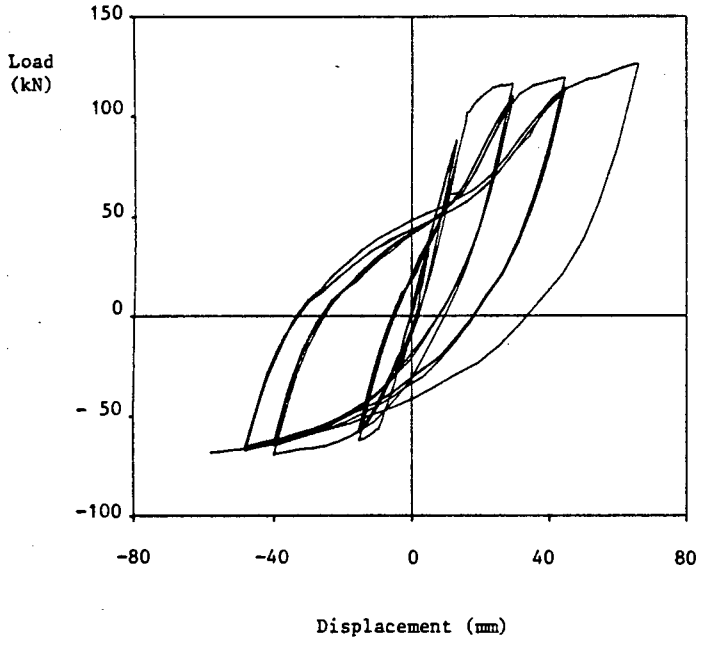

Figure 6.11(a) : Load-displacement response, Beam R-1, 50 layers

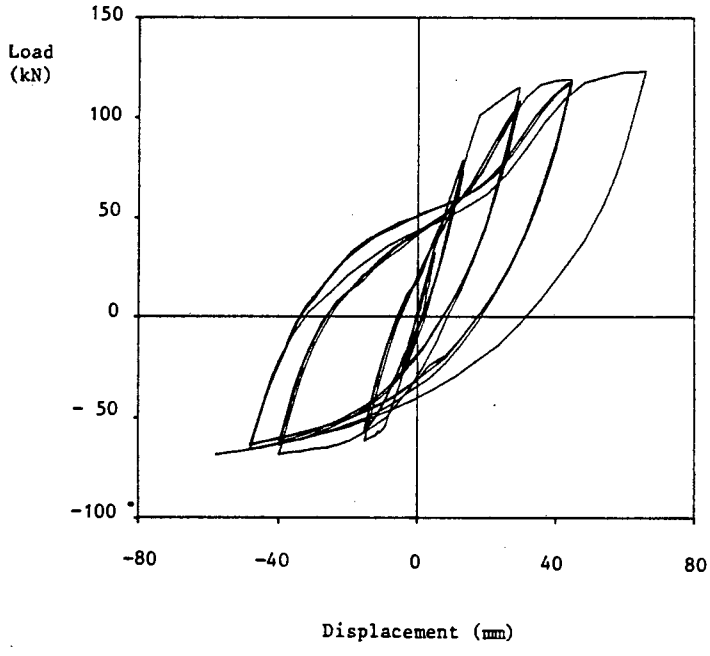

Figure 6.11(b) : Load-displacement response, Beam R-1, 2 layers

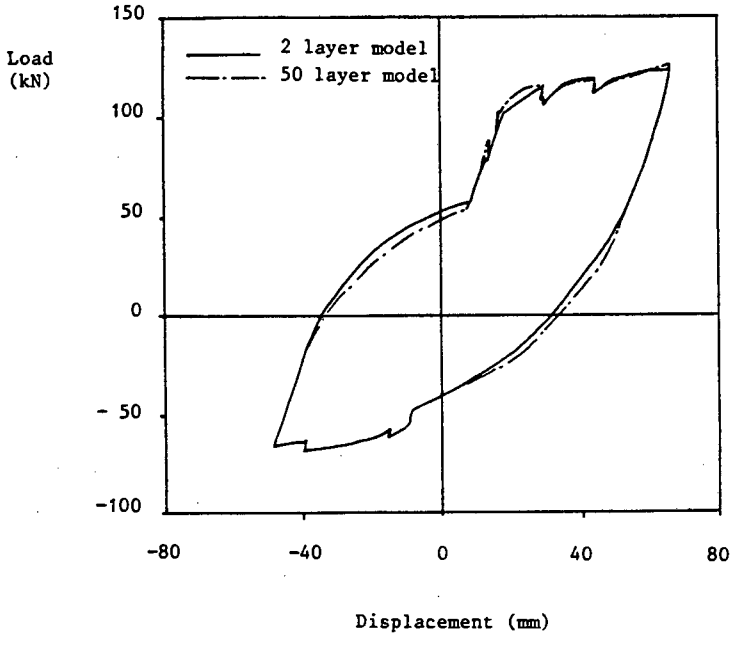

Figure 6.11(c) : Load-displacement envelopes, Beam R-1

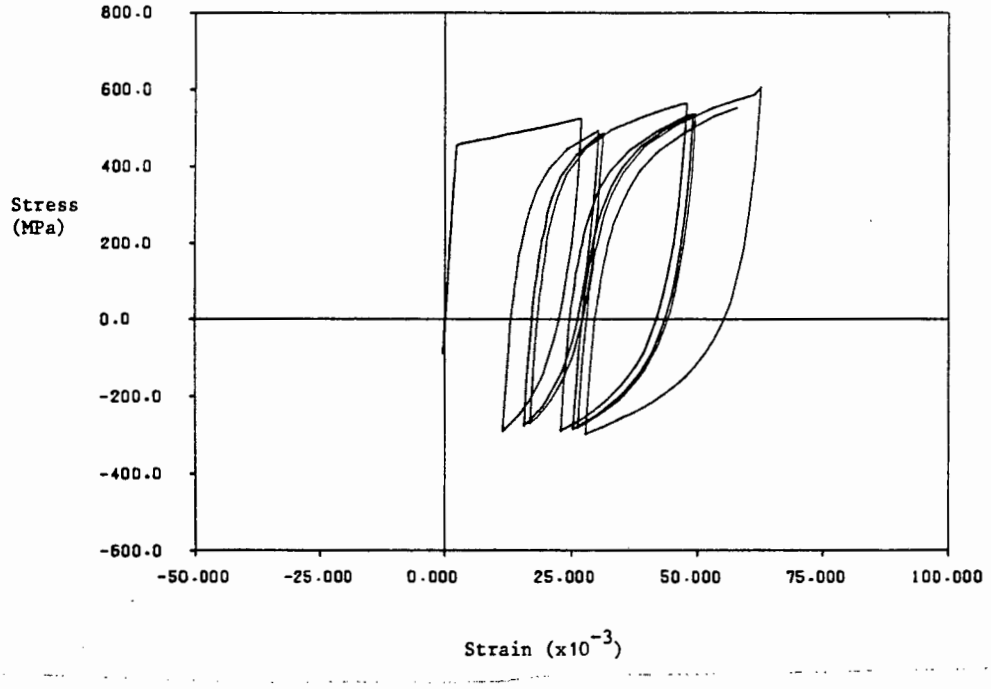

Figure 6.11(d) : Beam R-1, 50 layer model, top steel stress-strain response

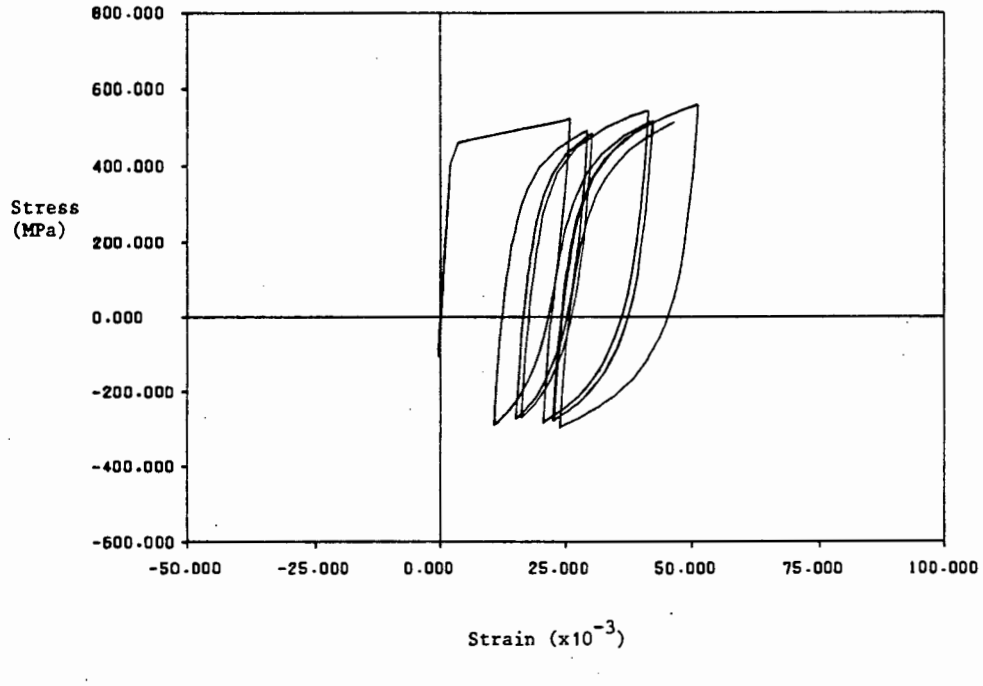

Figure 6.11(e) : Beam R-1, 2 layer model, top steel stress-strain response

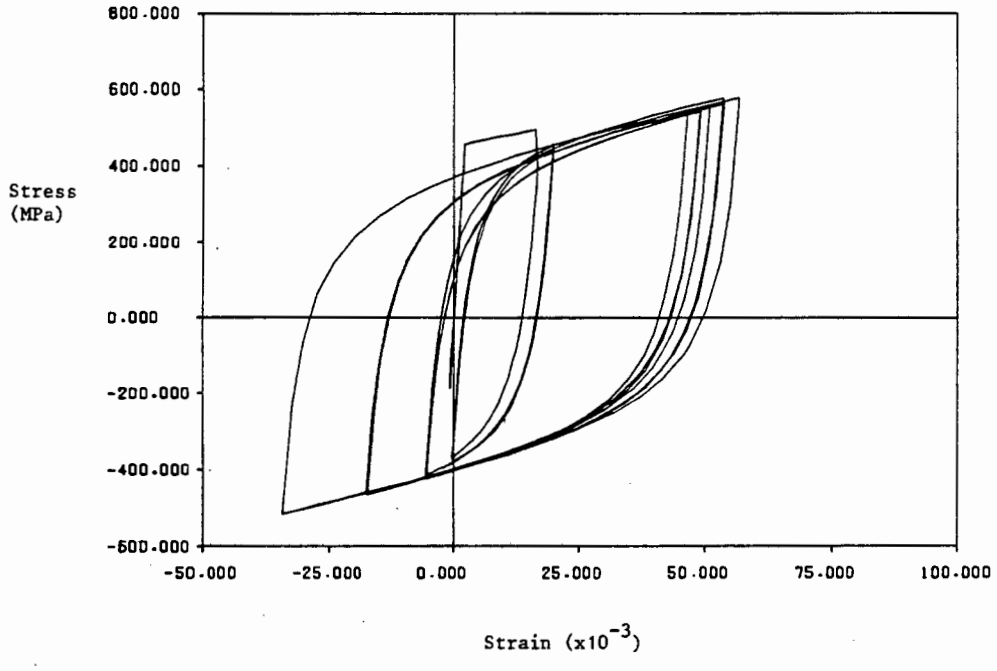

Figure 6.11(f) : Beam R-1, 50 layer model, bottom steel stress-strain response

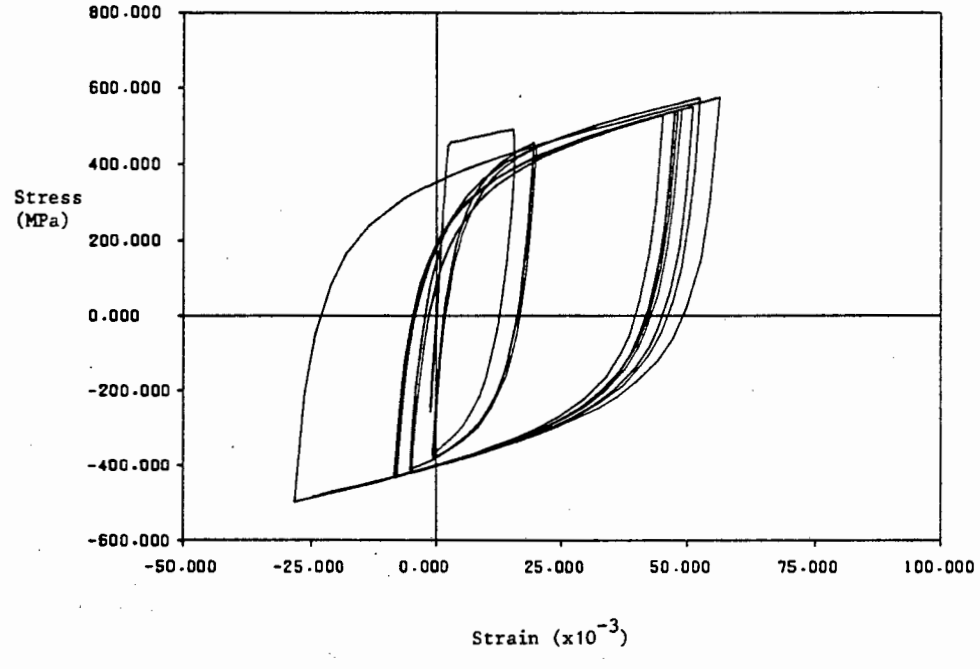

Figure 6.11(g) : Beam R-1, 2 layer model, bottom steel stress-strain response

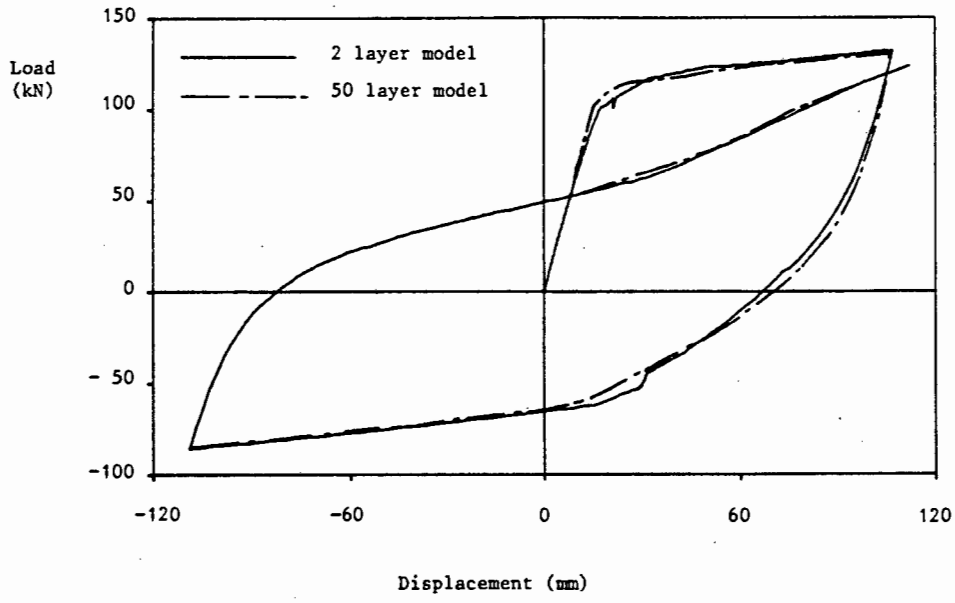

Figure 6.12 : Load-displacement responses, Beam R-4

The results do not correlate well around the point of yielding in some cases. However, at larger response levels there is generally good correlation. For all the beams, the damage measures obtained with the two-layer model show little difference when compared to those obtained using 50 concrete layers. There is also no difference in the predicted onset of failure for the beams in flexure. This underlines the need to obtain a good correlation in the moment-curvature relationship for the 50 layer and the two-layer models at the maximum expected curvature range. Matching the relationships at lower curvatures would result in a model that produces good results for low levels of cyclic loading, but would not predict the onset of failure very well.

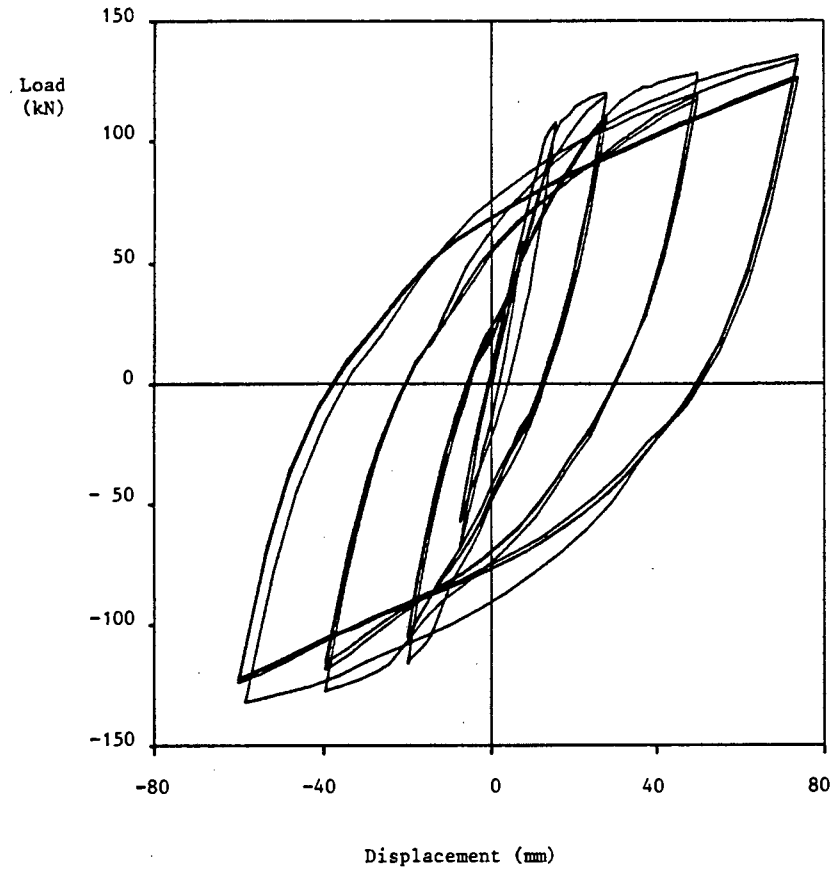

Figure 6.13(a) : Load-displacement response, Beam R-6, 50 layers

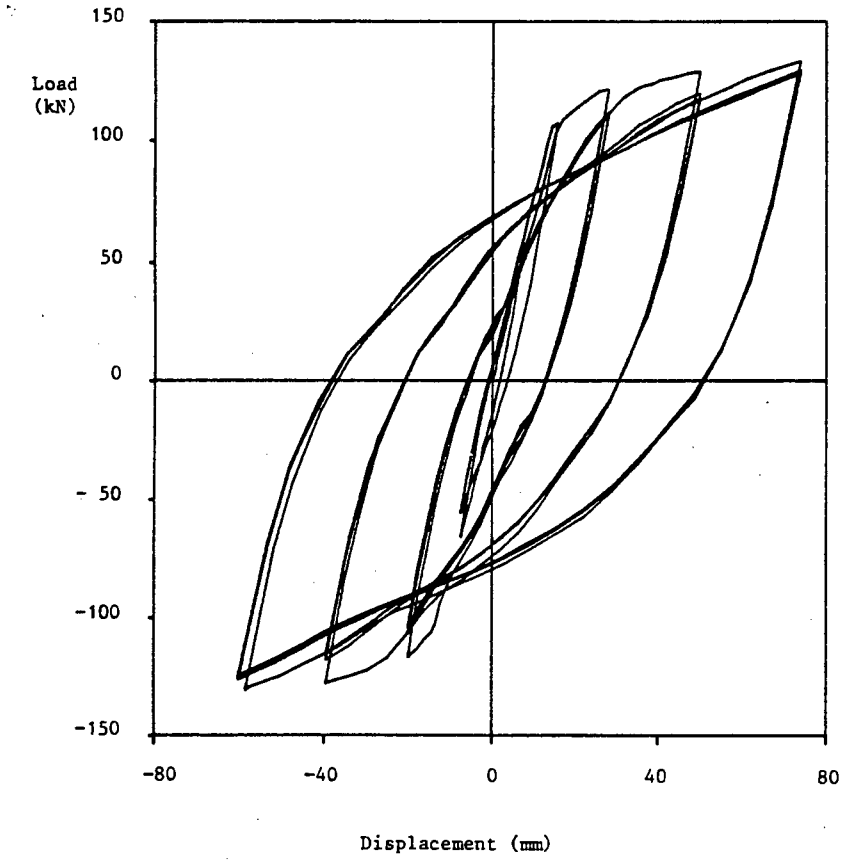

Figure 6.13(b) : Load-displacement responses, Beam R-6, 2 layers

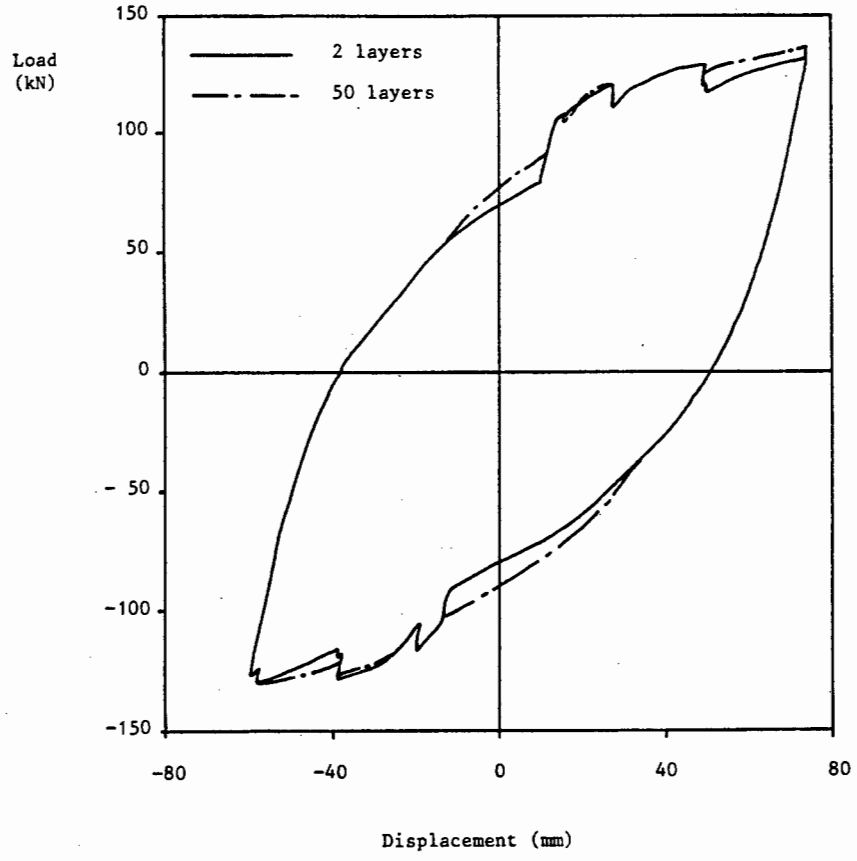

Figure 6.13(c) : Load-displacement envelopes, Beam R-6

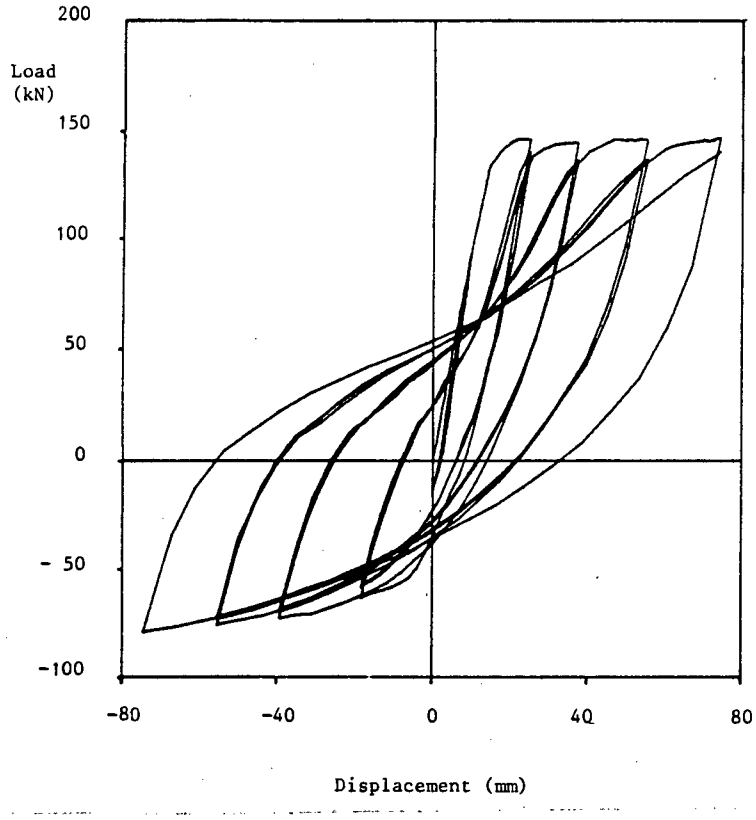

Figure 6.14(a) : Load-displacement response, Beam T-1, 50 layers

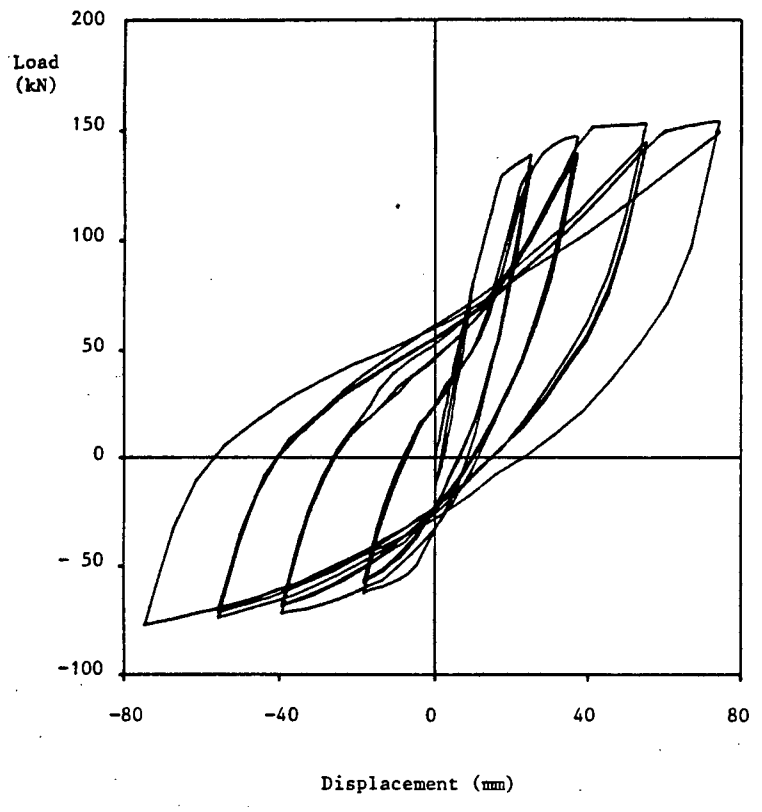

Figure 6.14(b) : Load-displacement response, Beam T-1, 2 layers

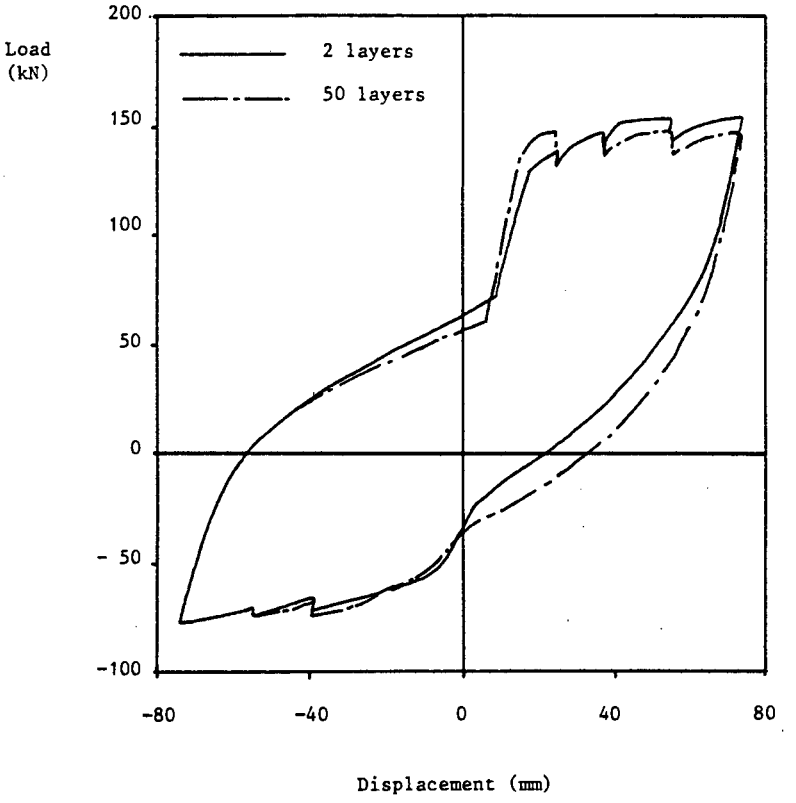

Figure 6.14(c) : Load-displacement envelopes, Beam T-1

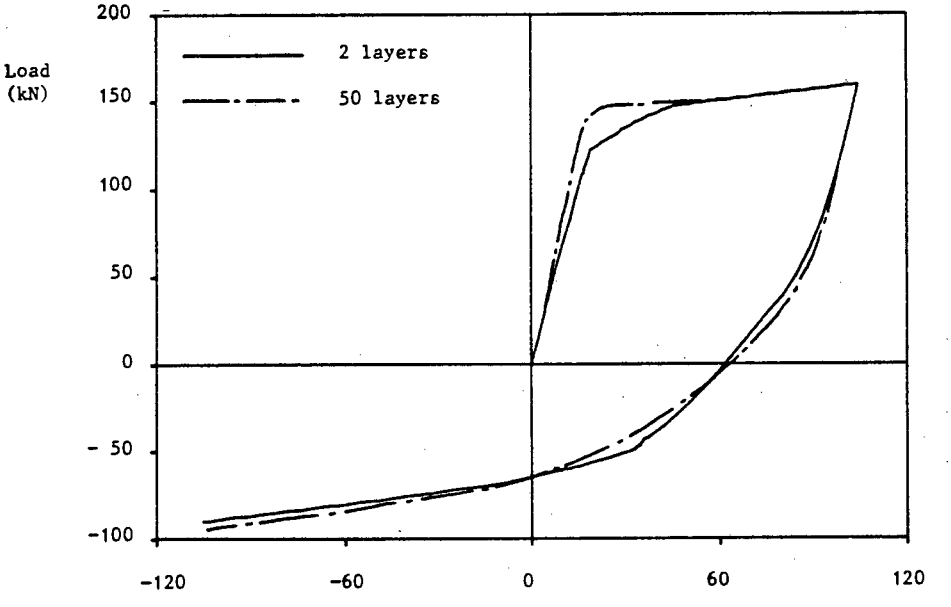

Figure 6.15 : Load-displacement responses, Beam T-2

CHAPTER 7

CONCLUSIONS AND RECOMMENDATIONS FOR FURTHER RESEARCH

In this thesis, a model for the cyclic response of reinforced concrete members has been described. One of the objectives was to explicitly include in the model the mechanics contributing to the cyclic behaviour of typical reinforced concrete members.

The important assumptions contained in the model are, firstly, that the member deforms with double curvature bending, and, secondly, that the deformations are primarily due to flexure and slippage of the reinforcement in the beam-column joint. For the analytical model, the cross-section is represented by a number of steel and concrete layers, while along the length of the beam inelastic zones are defined at the ends.

Attention was paid to the constitutive models used to describe the cyclic response of steel, concrete and the steel-concrete interaction, as well as the aspects concerning the implementation into a computer code.

From the results presented in this thesis, the following major conclusions were reached :

1. The proposed layered beam model successfully models the cyclic behaviour of reinforced concrete cantilevers. The model includes the essential mechanics which affect the cyclic behaviour. The study included members with loading histories consisting of either a single large amplitude cycle, or a number of cycles at a lower loading amplitude.

2. The concrete damage model is a simple yet effective constitutive model. It also provides a useful basis in a damage measure for predicting the onset of flexural failure in beams.

3. It is important to include the Bauschinger effect in the steel constitutive model.

4. The effect of bar-slippage in a beam-column joint needs to be included in the modelling process. With a finite element representation for the bar slippage model, it was shown that only a few higher order elements were required to produce satisfactory results for a straight bar. For a bar with a hooked end, the assumption of a uniform bond stress-slip relationship along the bar is not satisfactory.

5. The concept of strain increment compatibility at the cracked interface of a beam-column joint is effective in modelling the mechanics of crack closure.

6. The concrete damage measure successfully predicts the onset of flexural failure for the cantilever components studied. It is not clear how good the anchorage damage measure is.

7. A two-layered beam model produces results which correspond closely with the results for a beam modelled with 50 concrete layers. The improvement in computational time is significant. For the two-layer and the 50 layer models, an average of 28 and 15 increments per CPU second respectively were achieved for a typical cantilever problem.

8. The solution strategies adopted, as well as the numerical algorithms in which Newton methods are used to solve the nonlinear equations, provided a robust model with good convergence rates.

The work reported in this thesis is considered the first development stage of the proposed layered beam model. Various aspects have been identified for further development of the model; these are now discussed.

The bar-slippage model needs to include the variations in bond stress-slip relation along an anchored bar. Included in this development, would be the enhancements to the bond stress-slip constitutive relation to account for the variations in positive and negative slip in unconfined concrete. Another aspect to be considered is modelling of the cyclic behaviour at an interior beam-column connection.

The layered beam model can be improved by including shear deformation. The way in which this should be accomplished needs to be investigated. In addition the concrete damage measure would have to be enhanced to include some dependence on the shear deformation. Once a clearer understanding has been obtained for the cyclic response of beams in which shear deformation plays an important part, parametric studies are required with the objective of simplifying some of the modelling aspects.

Another aspect that needs to be addressed is the efficiency of the computations. It is important to reduce the computational time as much as possible, if such a model is to be of practical use to the engineer.

A significant amount of expertise is required by the engineer so that he can correctly specify the input needed for the nonlinear solution algorithms and

the modelling aspects. One way of assisting the engineer would be to disseminate heuristic knowledge of the modelling process. The acquisition of such knowledge requires the use of traditional and artificial intelligence techniques. Recent research by Hawla [77] addresses these issues.

Finally, further study into the concrete damage measure A_c is required in order to better calibrate the damage measure with experimental results. Recent work by Scribner [78] provides a valuable starting point.

REFERENCES

[1] A.S.C.E., 'State-of-the-Art Report on Finite Element Analysis of Reinforced Concrete', *ASCE*, 1982.

[2] Blume, J A, Newmark, N M and Corning, L H, 'Design of Multistorey Reinforced Concrete Buildings for Earthquake Motions', *Portland Cement Association*, Illinois, 1961.

[3] van Mier, J G M, 'Fracture of Concrete Under Cyclic Complex Stress', *Heron*, v.31, No. 3, 1986.

[4] Park, R and Paulay, T, '*Reinforced Concrete Structures*', John Wiley & Sons, 1975.

[5] Fintel, M and Ghosh, S K, 'Earthquake-resistant Structures', Chapter 15 in '*Handbook of Structural Concrete*' Ed. F K Kong; R H Evans; E Cohen and F Roll, Pitman Books, 1983.

[6] Biggs, J M, 'Some Comments on Aseismic Design', *Proceedings of the Symposium; Structural Engineering : Research, Education and Practice*, Ed. E Kausel, MIT, 1983.

[7] Banon, H; Biggs, J M and Irvine, H M, 'Prediction of Seismic Damage in Reinforced Concrete Frames', *Publication No. R80-16, Department of Civil Engineering*, Massachusetts Institute of Technology, Cambridge, Mass.

[8] Fajfar, P and Fischinger, M, 'Dynamic Analysis of RC Buildings - How much sophistication is justified', *Proceedings of the Conference. Computer Aided Analysis and Design of Concrete Structures.*

[9] Otani, S, 'Nonlinear dynamic analysis of reinforced concrete building structures', *Canadian Journal of Civil Engineering*, v.7, 1983, pp 333-344.

[10] Meyer, C, 'Dynamic Finite Element Analysis of Reinforced Concrete Structures', Advanced Mechanics of Reinforced Concrete: Introductory Report, *IABSE Colloquium*, Delft, 1981.

[11] Roesset, J M, 'Nonlinear Dynamic Analysis', *Proceedings of the Symposium; Structural Engineering : Research, Education and Practice*, Ed. E Kausel, MIT, 1983.

[12] Sozen, M A, 'Hysteresis in Structural Elements', *Applied Mechanics in Earthquake Engineering*, AMD-vol. 8, *ASME*, 1974.

[13] Bertero, V V; Bresler, B and Liao, H, 'Stiffness Degradations of Reinforced Concrete Members Subjected to Cyclic Flexural Moments', *Report No. EERC 69-12, Earthquake Engineering Research Center*, University of California, Berkeley, Dec. 1969.

[14] Bazant, Z P and Bhat, P D, 'Prediction of Hysteresis of Reinforced Concrete Members', *Journal of the Structural Division, ASCE*, v.103, Jan. 1977, pp 153-167.

[15] Keshavarzian, M and Schrobrich, W C, 'Analytical Models for the Nonlinear Analysis of R/C Structures', *Presented at the 1983 Annual Convention*, ACI, Los Angeles.

[16] Karsan, I K and Jirsa, J O, 'Behaviour of concrete under compressive loading', *Journal of the Structural Division, ASCE*, v.95, Dec. 1969, pp 2543-2563.

[17] Mercer, C D and Martin, J B, 'A Numerical Model for the Steel-Concrete Interaction in Cyclically Loaded Reinforced Concrete Structures', *Technical Report No. 90, UCT/CSIR Applied Mechanics Research Unit*, University of Cape Town, South Africa, March 1987.

[18] Filippou, F C; Popov, E P and Bertero, V V, 'Effects of Bond Deterioration on Hysteretic Behaviour of Reinforced Concrete Joints', *Report No. UCB/EERC-83/19, Earthquake Engineering Research Center*, University of California, Berkeley, August 1983.

[19] Kent, D C and Park, R, 'Flexural Members with Confined Concrete', ASCE, *Journal of the Structural Division*, v.97, No. ST7, July 1971.

[20] Bertero, V V and Popov, E P, 'Seismic Behaviour of Ductile Moment-Resisting Reinforced Concrete Frames', SP53-11 in Reinforced Concrete Structures in Seismic Zones, *ACI Special Publication SP-53*, 1977, ACI.

[21] Uzumeri, S M, 'Strength and Ductility of Cast-in-Place Beam-Column Joints', SP53-12 in Reinforced Concrete Structures in Seismic Zones, *ACI Special Publication SP-53*, 1977, ACI.

[22] Gulkan, P and Sozen, M A, 'Response and Energy-Dissipation of Reinforced Concrete Frames Subjected to Strong Base Motions', *Structural Research Series No. 377*, University of Illinois, May 1971.

[23] Popov, E P, 'Experiment as an Aid to Structural Seismic Design', *Experimental Mechanics*, June 1986, pp 194-208.

[24] Burns, N H and Siess, C P, 'Repeated and Reversed Loading in Reinforced Concrete', *Journal of the Structural Division, ASCE*, October 1966, pp 65-78.

[25] Brown, R H and Jirsa, J O, 'Reinforced Concrete Beams Under Load Reversals', *ACI Journal*, May 1971, pp 380-390.

[26] Gosain, N K; Brown, R H and Jirsa, J O, 'Shear Requirements for Load Reversals on RC Members', *Journal of the Structural Division, ASCE*, July 1977, pp 1461-1476.

[27] Lee, D L N; Wight, J K and Hanson, R D, 'RC Beam-Column Joints under Large Load Reversals', *Journal of the Structural Division, ASCE*, December 1977, pp 2337-2349.

[28] Scribner, C F and Wight, J K, 'Strength Decay in R/C Beams under Load Reversals', *Journal of the Structural Division, ASCE*, April 1980, pp 861-875.

[29] Durrani, A J and Wight, J K, 'Behaviour of Interior Beam to Column Connections under Earthquake Type Loading', *ACI Journal*, May-June 1985, pp 343-349.

[30] Hwang, T-H and Scribner, C F, 'RC Member Cyclic Response During Various Loadings', *Journal of the Structural Division, ASCE*, v.110, March 1984, pp 477-489.

[31] Ehsani, M R and Wight, J K, 'Exterior Reinforced Concrete Beam to Column Connections Subjected to Earthquake Type Loading', *ACI Journal*, July-August 1985, pp 492-499.

[32] Nmai, C K and Darwin, D, 'Lightly Reinforced Concrete Beams under Cyclic Loads', *ACI Journal*, Sept.-Oct. 1986, pp 777-783.

[33] Ma, S-Y M; Bertero, V V and Popov, E P, 'Experimental and Analytical Studies on the Hysteretic Behaviour of Reinforced Concrete Rectangular and T-Beams', *Report No. EERC 76-2, Earthquake Engineering Research Center*, University of California, Berkeley, May 1976.

[34] Clough, R W and Gidwani, J, 'Reinforced Concrete Frame 2 : Seismic Testing and Analytical Correlation', *Report No. EERC 76-15, Earthquake Engineering Research Center*, University of California, Berkeley, June 1976.

[35] Popov, E P, 'Bond and Anchorage of Reinforcing Bars Under Cyclic Loading', *ACI Journal*, July-August 1984, pp 340-349.

[36] Ciampi, V; Eligehausen, R; Bertero, V and Popov, E, 'Analytical Model for Deformed Bar Bond under Generalized Excitations', *Colloquium on Advanced Mechanics of Reinforced Concrete*, Final Report, IABSE, Delft, 1981.

[37] Goto, Y, 'Cracks Formed in Concrete Around Deformed Tension Bars', *ACI Journal*, April 1971, pp 244-251.

[38] Park, R; Gaerty, L and Stevenson, E C, 'Tests on an Interior Reinforced Concrete Beam-Column Joint', *Bulletin of the New Zealand National Society for Earthquake Engineering*, v.14, No. 2, June 1981.

[39] Stanton, J F and McNiven, H D, 'The Development of a Mathematical Model to Predict the Flexural Response of Reinforced Concrete Beams to Cyclic Loads using System Identification', *Report No. EERC 79-2, Earthquake Engineering Research Center*, University of California, Berkeley, Jan. 1982.

[40] Giuffre, A and Pinto, P E, 'Il Comportamento del Cemento Armato per Sollecitazioni Cicliche di Forte Intensita', *Giornole del Genio Civile*, Maggio, 1970.

[41] Menegotto, M and Pinto, P, 'Method of Analysis for Cyclically Loaded Reinforced Concrete Plane Frames Including Changes in Geometry and Nonelastic Behaviour of Elements under Constrained Normal Force and Bending', *Symposium on Resistance and Ultimate Deformability of Structures acted on by Well-Defined Repeated Loads*, Preliminary Report, IABSE, Lisbon, 1973.

[42] Stanton, J F and McNiven, H D, 'Towards an Optimum Model for the Response of Reinforced Concrete Beams to Cyclic Loads', *Earthquake Engineering and Structural Dynamics*, v.11, 1983, pp 299-312.

[43] Bazant, Z P, 'Mechanics of distributed cracking', *Applied Mechanics Reviews*, v.39, May 1986, pp 675-705.

[44] Kachanov, L M, 'On the Creep Rupture Time', *IZV. AN SSR, OTN*, No. 8, 1958, p 26.

[45] Krajcinovic, D and Selvaraj, S, 'Constitutive Equations for Concrete', in *Proceedings of the International Conference on Construction Laws for Engineering Materials*, Tucson, pp 399-406.

[46] Krajcinovic, D, 'Continuum Damage Mechanics', *Applied Mechanics Reviews*, v.37, Jan. 1984, pp 1-6.

[47] Lemaitre, J, 'How to Use Damage Mechanics', *Nuclear Engineering and Design*, v.80, 1984, pp 233-245.

[48] Lorrain, M and Loland, K E, 'Damage Theory Applied to Concrete', in *Fracture Mechanics of Concrete*, Ed. F H Wittmann, Elsevier, Amsterdam, 1983.

[49] Resende, L and Martin, J B, 'A progressive damage continuum model for granular materials', *Computer Methods in Applied Mechanics and Engineering*, v.42, 1984, pp 1-18.

[50] Mazars, J and Lemaitre, J, 'Application of Continuous Damage Mechanics to Strain and Fracture Behaviour of Concrete', in *Applications of Fracture Mechanics to Cementitious Composites*, NATO-ARW, Northwest University, Ed. S P Shah, Sept. 1984.

[51] Resende, L, 'Constitutive Modelling and Finite Element Analysis in Geomechanics', PhD Thesis, University of Cape Town, Cape Town, South Africa, 1984.

[52] William, K, 'Experimental and Computational Aspects of Concrete Fracture', in *Computer-Aided Analysis and Design of Concrete Structures*, Ed. F Damjanic, E Hinton, D R J Owen, N Bicanic and V Simovic, Pineridge, Swansea, 1984.

[53] Resende, L, 'A Damage Mechanics Constitutive Theory for the Inelastic Behaviour of Concrete', *Computer Methods in Applied Mechanics and Engineering*, v.60, 1987, pp 57-93.

[54] Morita, S and Kaku, T, 'Local Bond Stress-slip Relationship under Repeated Loading', Preliminary Publication, *Symposium on Structures Acted on by Repeated Loads*, IABSE, Lisbon, 1973.

[55] Mirza, M S and Houde, J, 'Study of Bond Stress-slip Relationship and Reinforced Concrete', *ACI Journal*, v.76, No. 19.

[56] Viawathanatepa, S, Popov, E P and Bertero, V V, 'Effects of Generalized Loadings on Bond of Reinforcing Bars Embedded in Confined Concrete Blocks', *Report No. UCB/EERC 79-22, Earthquake Engineering Center*, University of California, Berkeley, Aug. 1979.

[57] Bresler, B and Bertero, V V, 'Behaviour of Reinforced Concrete Under Repeated Load', *Journal of the Structural Division, ASCE*, v.24, June 1968.

[58] Eligehausen, R; Bertero, V V and Popov, E P, 'Hysteretic Behaviour of Reinforcing Deformed Hooked Bars in R/C Joints', *Proceedings, 7th European Conference on Earthquake Engineering*, v.4, Athens, Sept. 1982.

[59] ACI Committee 408, 'Bond Stress - The State of the Art', *ACI Journal*, v.63, No. 11, Nov. 1966.

[60] Rehm, G, 'The Basic Principles of the Bond Between Steel and Concrete', *C & CA Library Translation*, No. 134, Cement and Concrete Association, London, 1968.

[61] Cowell, A D; Popov, E P and Bertero, V V, 'Effects of Concrete Types and Loading Conditions on Local Bond-slip Relationships,' *Report No. UCB/EERC 82/17, Earthquake Engineering Research Center*, University of California, Berkeley, Sept. 1982.

[62] Clough, R W; Benuska, K L and Wilson, E L, 'Inelastic Response of Tall Buildings', *Proceedings, 3rd World Conference on Earthquake Engineering*, New Zealand, 1965, v.II, pp 68-89.

[63] Giberson, M F, 'Two Nonlinear Beams with Definitions of Ductility', *Journal of the Structural Division, ASCE*, Feb. 1969, pp 137-155.

[64] Clough, R W, 'Effects of stiffness degradation on earthquake ductility requirements', *Structural and Materials Research, Structural Engineering Laboratory*, University of California, Berkeley, Report No. 66-16.

[65] Takeda, T; Sozen, M A and Nielsen, N N, 'Reinforced Concrete Response to Simulated Earthquakes', *Journal of the Structural Division, ASCE*, Dec. 1970, pp 2557-2573.

[66] Takayanagi, T and Schnobrich, W C, 'Computed behaviour of reinforced concrete coupled shear walls', University of Illinois, Urbana, *Structural Research Series No. 434*.

[67] Hsu, L W, 'Behaviour of Multistorey R/C Walls during Earthquakes', PhD Dissertation, University of Illinois, Urbana, 1974.

[68] Soleimani, D, 'Reinforced Concrete Frames under Earthquake Loadings with Stiffness Degradation', PhD Dissertation, University of California, Berkeley, Dec. 1978.

[69] Meyer, C; Roufaiel, M S and Arzoumanidis, S G, 'Analysis of Damaged Concrete Frames for Cyclic Loads', *Earthquake Engineering and Structural Dynamics*, v.11, 1983, pp 207-228.

[70] Schnobrich, W C, 'Behaviour of R/C Structures Predicted by the Finite Element Method', *Int. Journal of Computers and Structures*, v.7, No. 3, June 1977, pp 365-376.

[71] Bohong, Z; Mingshun, W and Kunlian, Z, 'A Study of Hysteretic Curve of Reinforced Concrete Members under Cyclic Loading', *Seventh World Conference on Earthquake Engineering*, v.6, Istanbul, 1981.

[72] Park, R; Kent, D C and Sampson, R A, 'Reinforced Concrete Members with Cyclic Loading', *Journal of the Structural Division, ASCE*, v.98, July 1972, pp 1341-1359.

[73] Vos, J, 'A Data Handling and Sequential Work Files Package; Programmer's Manual', *Technical Report No. 95, UCT/CSIR Applied Mechanics Research Unit*, University of Cape Town, South Africa, August 1987.

[74] Roufaiel, M S L and Meyer, C, 'Analytical Modelling of Hysteretic Behaviour of R/C Frames', *Journal of the Structural Division, ASCE*, v.113, March 1987, pp 429-444.

[75] Eligehausen, R; Bertero, V V and Popov, E P, 'Local Bond Stress-Bond Slip Relationship of Deformed Bars under General Excitations', *UCB/EERC - 83/23, Earthquake Engineering Research Center*, University of California, Berkely, October 1983.

[76] Crisfield, M A, 'A Fast Incremental/Iterative Solution Procedure That Handles "Snap Through"', *Computers and Structures*, v.13, 1981, pp 55-62.

[77] Hawla, D L, 'Knowledge Acquisition for Effective use of Engineering Software', PhD Thesis, University of Cape Town, South Africa, 1987.

[78] Scribner, C F, 'Reinforcement Buckling in Reinforced Concrete Flexural Members', *ACI Journal*, Nov-Dec. 1986, pp 966-973.

APPENDIX A

NUMERICAL INTEGRATION CONSTANTS FOR INELASTIC ZONES

The following integrals are calculatged using Simpson's Rule. The nomenclature is defined in Figures 3.14(a) and 3.14(b).

$$\text{(i)} \quad \int_A^a \phi \, dx = \frac{x_a}{3n} \{\phi_A + \phi_a\}$$

$$+ \frac{x_a}{3n} \{4 \phi_i\} \qquad : i \text{ odd}, \ 1 \leq i \leq n-1$$

$$+ \frac{x_a}{3n} \{2 \phi_i\} \qquad : i \text{ even}, \ 2 \leq i \leq n-2$$

(A.1)

$$\text{(ii)} \quad \int_A^a \theta \, dx = \frac{x_a}{3n} \left\{3n \, \theta_A^f + \frac{(3n+1)}{3n} x_a \phi_A + \frac{x_a}{3n} \phi_a\right\}$$

$$+ \frac{x_a}{3n} \left\{\frac{10 \, x_a}{3n}\right\} \phi_i \qquad : i \text{ odd}, \ 1 \leq i \leq n-1$$

$$+ \frac{x_a}{3n} \left\{\frac{4 \, x_a}{n} (n-1-i)\right\} \phi_i \qquad : i \text{ odd}, \ 1 \leq i \leq n-3$$

$$+ \frac{x_a}{3n} \left\{\frac{14 \, x_a}{3n}\right\} \phi_i \qquad : i \text{ even}, \ 2 \leq i \leq n-2$$

$$+ \frac{x_a}{3n} \left\{\frac{2 \, x_a}{n} (n-2-i)\right\} \phi_i \qquad : i \text{ even}, \ 2 \leq i \leq n-4$$

(A.2)

$$\text{(iii)} \quad \int_b^B \phi \, dx = \frac{x_b}{3m} \{\phi_B + \phi_b\}$$

$$+ \frac{x_b}{3m} \{4 \phi_j\} \qquad : j \text{ odd}, \ 1 \leq j \leq m-1$$

$$+ \frac{x_b}{3m} \{2 \phi_j\} \qquad : j \text{ even}, \ 2 \leq j \leq m-2$$

(A.3)

$$\text{(iv)} \quad \int_b^B \theta \, dx = \frac{x_b}{3m} \left\{3m \, \theta_B^f - \frac{(3m+1)}{3m} x_b \, \phi_B - \frac{x_b}{3m} \phi_b\right\}$$

$$- \frac{x_b}{3m} \left\{\frac{10 \, x_b}{3m}\right\} \phi_j \qquad : j \text{ odd}, \ 1 \leq i \leq m-1$$

$$- \frac{x_b}{3m} \left\{\frac{4 \, x_b}{m} (m-1-i)\right\} \phi_j \qquad : j \text{ odd}, \ 1 \leq i \leq m-3$$

$$- \frac{x_b}{3m} \left\{\frac{14 \, x_b}{3m}\right\} \phi_j \qquad : j \text{ even}, \ 1 \leq j \leq m-2$$

$$- \frac{x_b}{3m} \left\{\frac{2 \, x_b}{m} (m-2-i)\right\} \phi_j \qquad : j \text{ even}, \ 1 \leq i \leq m-4$$

(A.4)

The function $\Omega(\phi_i, \phi_j)$ in equation (3.30) is given as

$$\Omega(\phi_i, \phi_j) = \left\{ - \left[\frac{x_a^2(3n+1)}{\ell_e (3n)^2} + \frac{x_a}{3n}\right] \phi_A - \left[\frac{x_a^2}{\ell_e (3n)^2} + \frac{x_a}{3n}\right] \phi_a \right\}$$

$$- \left\{\frac{10}{\ell_e} \left[\frac{x_a}{3n}\right]^2 + \frac{4 \, x_a}{3n}\right\} \phi_i \qquad : i \text{ odd}, \ 1 \leq i \leq n-1$$

$$- \left\{ \frac{4\, x_a^2}{\ell_e (3n)^2} (n-1-i) \right\} \phi_i \qquad : i \text{ odd}, \ 1 \le i \le n-3$$

$$- \left\{ \frac{14}{\ell_e} \left[\frac{x_a}{3n} \right]^2 + \frac{2\, x_a}{3n} \right\} \phi_i \qquad : i \text{ even}, \ 2 \le i \le n-2$$

$$- \left\{ \frac{2\, x_a^2}{\ell_e (3n)^2} (n-2-i) \right\} \phi_i \qquad : i \text{ even}, \ 2 \le i \le n-4$$

$$+ \left\{ \frac{10}{\ell_e} \left[\frac{x_b}{3m} \right]^2 \right\} \phi_j \qquad : j \text{ odd}, \ 1 \le j \le m-1$$

$$+ \left\{ \frac{12}{\ell_e} \left[\frac{x_b^2}{3m^2} \right] (m-1-j) \right\} \phi_j \qquad : j \text{ odd}, \ 1 \le j \le m-3$$

$$+ \left\{ \frac{14}{\ell_e} \left[\frac{x_b}{3m} \right]^2 \right\} \phi_j \qquad : j \text{ even}, \ 2 \le j \le m-2$$

$$+ \left\{ \frac{2\, x_b^2}{\ell_e 3m^2} (m-2-j) \right\} \phi_j \qquad : j \text{ even}, \ 2 \le j \le m-4$$

$$+ \frac{1}{\ell_e} \left[\frac{x_b}{3m} \right]^2 (3m+1)\, \phi_B + \frac{1}{\ell_e} \left[\frac{x_b}{3m} \right]^2 \phi_b \quad .$$

(A.5)

The function $\Omega(\phi_i, \phi_j)$ in equation (3.31) is given as

$$\Omega(\phi_i, \phi_j) = \left\{ - \left[\frac{3n+1}{\ell_e}\left[\frac{x_a}{3n}\right]^2\right]\phi_A - \left[\frac{1}{\ell_e}\left[\frac{x_a}{3n}\right]^2\right]\phi_a \right\}$$

$$- \left\{\frac{10}{\ell_e}\left[\frac{x_a}{3n}\right]^2\right\}\phi_i \qquad : i \text{ odd}, \ 1 \le i \le n-1$$

$$- \left\{\frac{12}{\ell_e}\left[\frac{x_a}{3n}\right]^2 (n-1-i)\right\}\phi_i \qquad : i \text{ odd}, \ 1 \le i \le n-3$$

$$- \left\{\frac{14}{\ell_e}\left[\frac{x_a}{3n}\right]^2\right\}\phi_i \qquad : i \text{ even}, \ 2 \le i \le n-2$$

$$- \left\{\frac{6}{\ell_e}\left[\frac{x_a}{3n}\right]^2 (n-2-i)\right\}\phi_i \qquad : i \text{ even}, \ 2 \le i \le n-4$$

$$+ \left\{\frac{10}{\ell_e}\left[\frac{x_b}{3m}\right]^2 + \frac{4\,x_b}{3m}\right\}\phi_j \qquad : j \text{ odd}, \ 1 \le j \le m-1$$

$$+ \left\{\frac{12}{\ell_e}\left[\frac{x_b}{3m}\right]^2 (m-1-j)\right\}\phi_j \qquad : j \text{ odd}, \ 1 \le j \le m-3$$

$$+ \left\{\frac{14}{\ell_e}\left[\frac{x_b}{3m}\right]^2 + \frac{2\,x_b}{3m}\right\}\phi_j \qquad : j \text{ even}, \ 2 \le j \le m-2$$

$$+ \left\{\frac{6}{\ell_e}\left[\frac{x_b}{3m}\right]^2 (m-2-j)\right\}\phi_j \qquad : j \text{ even}, \ 2 \le j \le m-4$$

$$+ \left\{\frac{1}{\ell_e}\left[\frac{x_b}{3m}\right]^2 (3m+1) + \frac{x_b}{3m}\right\}\phi_B$$

$$+ \left\{\frac{1}{\ell_e}\left[\frac{x_b}{3m}\right]^2 + \frac{x_b}{3m}\right\}\phi_b \quad . \qquad \text{(A.6)}$$

APPENDIX B

SOLUTION ALGORITHM USING ARC-LENGTH METHOD

The arc-length method as suggested by Crisfield [76], is used as the basis for a solution algorithm to solve the set of nonlinear equations given in equation (3.40).

Writing equation (3.40) in terms of a loading parameter λ we have

$$\underset{\sim}{F}^{int} = \underset{\sim}{F}^{*} = \lambda \underset{\sim}{P} + \underset{\sim}{A} \tag{B.1}$$

where $\underset{\sim}{A} = \begin{Bmatrix} F^{*} \\ 0 \end{Bmatrix}$

and $\underset{\sim}{P} = \begin{Bmatrix} 0 \\ 1 \end{Bmatrix}$.

The residual form of equation (B.1) is written as

$$\underset{\sim}{\psi} = (\lambda \underset{\sim}{P} + \underset{\sim}{A}) - \underset{\sim}{F}^{int} \quad . \tag{B.2}$$

This equation is expressed in the form, where we require that

$$\underset{\sim}{\psi}(\lambda + \delta \lambda) = \underset{\sim}{0} \quad . \tag{B.3}$$

Expanding equation (B.3) we have

$$\underset{\sim}{\mathcal{P}}(\lambda + \delta\lambda) = \underset{\sim}{\mathcal{P}}(\lambda) + \delta\lambda \frac{\partial \underset{\sim}{\mathcal{P}}}{\partial \lambda}$$

$$= \underset{\sim}{\mathcal{P}}(\lambda) + \delta\lambda \underset{\sim}{P} \quad . \tag{B.4}$$

Casting equation (B.2) in an iterative form, we have for iteration i

$$[J]\, \Delta\underset{\sim}{\epsilon}_o = - \underset{\sim}{\mathcal{P}}(\lambda^i + \delta\lambda^i) \quad . \tag{B.5}$$

Substituting from equation (B.4), equation (B.5) reduces to

$$\Delta\underset{\sim}{\epsilon}_o = - [J]^{-1} \underset{\sim}{\mathcal{P}}(\lambda^i) - [J]^{-1} \delta\lambda^i \underset{\sim}{P} \tag{B.6}$$

or

$$\Delta\underset{\sim}{\epsilon}_o = \Delta\bar{\underset{\sim}{\epsilon}}_o + \delta\lambda^i \Delta\underset{\sim}{\epsilon}^* \quad . \tag{B.7}$$

The total incremental displacement is defined as

$$\Delta\underset{\sim}{\epsilon}^{i+1} = \Delta\underset{\sim}{\epsilon}^i + \Delta\underset{\sim}{\epsilon}_o \quad . \tag{B.8}$$

If a modified Newton-Raphson method is used, the vector $\Delta\underset{\sim}{\epsilon}^*$ need only be calculated when the stiffness matrix is reformed.

A constraint equation is used to fix the 'incremental length' during an increment. Crisfield [76] suggests an equation of the form

$$(\Delta\underset{\sim}{\epsilon}^{i+1})^T (\Delta\underset{\sim}{\epsilon}^{i+1}) = \Delta\ell^2 \tag{B.9}$$

where $\Delta\ell$ is scalar quantity determined at the start of an increment, and superscript T denotes the transpose of the vector.

Given $\underset{\sim}{F}_t^{int}$, λ_t , $\underset{\sim}{\epsilon}_t$, $\Delta\ell$

1. Determine [J]

2. Calculate $\Delta\lambda^o$: Solve [J] $\Delta\underset{\sim}{\epsilon}^* = -\underset{\sim}{P}$

$$\Delta\ell^* = (\Delta\underset{\sim}{\epsilon}^*)^T(\Delta\underset{\sim}{\epsilon})$$

$$\Delta\lambda^o = \Delta\lambda^* \frac{\Delta\ell}{\Delta\ell^*}$$

$$\Delta\underset{\sim}{\epsilon}^o = (\Delta\underset{\sim}{\epsilon}^*)\Delta\lambda^o$$

3. Set counter i = 0

$$\Delta\underset{\sim}{\epsilon}^1_{t+\Delta t} = \Delta\underset{\sim}{\epsilon}^o$$

$$\underset{\sim}{\epsilon}^1_{t+\Delta t} = \underset{\sim}{\epsilon}_t + \Delta\underset{\sim}{\epsilon}^1_{t+\Delta t}$$
$$\lambda^1_{t+\Delta t} = \lambda_t + \Delta\lambda^o$$

4. Calculate $(\underset{\sim}{F}^{int})^1_{t+\Delta t}$

5. Calculate $\underset{\sim}{r}^1 = (\lambda^1_{t+\Delta t}\,\underset{\sim}{P} + \underset{\sim}{A}) - \underset{\sim}{F}_t^{int}$

6. Start iteration loop , i=i+1

7. Solve [J] $\Delta\bar{\underset{\sim}{\epsilon}} = -\underset{\sim}{r}^i$

8. Solve for roots ($\delta\lambda_1$, $\delta\lambda_2$) of $a_1\delta\lambda^2 + a_2\,\delta\lambda + a_3 = 0$

9. Choose correct root $\delta\lambda^i$

10. Update $\lambda^{i+1}_{t+\Delta t} = \lambda^i_{t+\Delta t} + \delta\lambda^i$

$$\Delta\underset{\sim}{\epsilon}^{i+1}_{t+\Delta t} = \Delta\underset{\sim}{\epsilon}^i_{t+\Delta t} + \Delta\bar{\underset{\sim}{\epsilon}} + \delta\lambda^i\,\Delta\underset{\sim}{\epsilon}^*$$

$$\underset{\sim}{\epsilon}^{i+1}_{t+\Delta t} = \underset{\sim}{\epsilon}_t + \Delta\underset{\sim}{\epsilon}^{i+1}_{t+\Delta t}$$

11. Calculate $(\underset{\sim}{F}^{int})^{i+1}_{t+\Delta t}$

12. Calculate $\underset{\sim}{r}^{i+1} = (\lambda^i_{t+\Delta t}\,\underset{\sim}{P} + \underset{\sim}{A}) - (\underset{\sim}{F}^{int})^{i+1}_{t+\Delta t}$

13. Check convergence, go to step 6 if solution has not converged

Table B.1 : Solution algorithm employing arc-length method

Substituting equations (B.7) and (B.8) into (B.9), the following quadratic equation is obtained ;

$$a_1 (\delta \lambda^i)^2 + a_2 \delta \lambda^i + a_3 = 0 \qquad \text{(B.10)}$$

where $a_1 = (\Delta\underset{\sim}{\epsilon}^*)^T(\Delta\underset{\sim}{\epsilon}^*)$,

$a_2 = 2(\Delta\underset{\sim}{\epsilon}^i + \Delta\underset{\sim}{\bar{\epsilon}})^T(\Delta\underset{\sim}{\epsilon}^*)$,

$a_3 = (\Delta\underset{\sim}{\epsilon}^i + \Delta\underset{\sim}{\bar{\epsilon}})^T(\Delta\underset{\sim}{\epsilon}^i + \Delta\underset{\sim}{\bar{\epsilon}}) - \Delta\ell^2$.

Further details on choosing the correct root for equation (B.10) and the procedure for obtaining the 'length' $\Delta\ell$ are given in [76].

A solution scheme which is based on the arc-length method described above, is given in Table B.1. It is assumed that the result of equation (B.1) is known at time t . The solution scheme is used to obtain the result of equation (B.1) at time t+Δt (for each increment Δt is calculated once convergence has been obtained). Note that in equation (B.2) , F^* always remains constant.